UNIVERSITY OF OKLAHOMA

GRADUATE COLLEGE

USE OF SMALL UNOCCUPIED AERIAL SYSTEM MULTISPECTRAL IMAGERY TO ADDRESS OPTICAL AND NON-OPTICAL WATER QUALITY PARAMETERS IN WATERSHED RESTORATION

A DISSERTATION

SUBMITTED TO THE GRADUATE FACULTY

in partial fulfillment of the requirements for the

Degree of

DOCTOR OF PHILOSOPHY

By

JUAN G. ARANGO CALDERON
Norman, Oklahoma
2020

USE OF SMALL UNOCCUPIED AERIAL SYSTEM MULTISPECTRAL IMAGERY TO ADDRESS OPTICAL AND NON-OPTICAL WATER QUALITY PARAMETERS IN WATERSHED RESTORATION

A DISSERTATION APPROVED FOR THE
SCHOOL OF CIVIL ENGINEERING AND ENVIRONMENTAL SCIENCE

BY THE COMMITTEE CONSISTING OF

Dr. Robert W. Nairn, Chair

Dr. Karl D. Hambright

Dr. Randall Kolar

Dr. Yang Hong

Dr. Darrell Townsend

Del príncipe para su abuela. Cuanta falta me hace escuchar tu voz.

ACKNOWLEDGMENTS

I want to thank my professor, friend, and advisor Dr. Robert W. Nairn, for believing that I could complete this work. When I hesitated, you never doubted, and it is because of your guidance, dedication, and patience that today I am not only a better professional; but also, a better human being.

With profound gratitude and respect, I would like to thank all the people who were directly engaged with this research. Especially to the Grand River Dam Authority (GRDA), for funding this project and to all my committee members (past and present): Dr. Karl D. Hambright, Dr. Randall Kolar, Dr. Yang Hong, Dr. Darrell Townsend, Dr. Robert Knox, and Dr. Kirsten de Beurs. Special thanks are provided to Grant Victor and his family for providing land access.

My most sincere gratitude also extends to all past and current members of the Center for Restoration of Ecosystems and Watersheds (CREW) research team, especially to Brandon Holzbauer-Schweitzer for all his help, time, and sincere advice. As you often mentioned, “we are in this together” and honestly, I believe that none of the work presented in this dissertation could have been produced without you.

I would now like to take the opportunity to thank my girlfriend, my friend, my lover, my confidant, and my life partner, Jana Sanchez. I cannot but thank her for letting me fall in love with her every day more and more; for assuring me in weak moments that everything was going to be fine, and most importantly, for teaching me that no matter what we encounter the next day, the most important thing is that we are together.

Finally, I want to thank my parents Elsa and Gonzalo, for all the unconditional inspiration, support, and care they have offered me.

Table of Contents

List of Tables

List of Figures

ABSTRACT

Remote sensing is defined as the art, science, and technology of obtaining reliable information about physical objects and the environment through the process of recording, measuring, and interpreting imagery and digital representations of energy patterns derived from non-contact sensor systems. Currently, one of the many applications for this technology is to monitor and predict water quality. In recent decades, the use of remote sensing tools for estimation of Secchi disk depth (SDD), total suspended solids (TSS), chlorophyll-a (Chl-a), and colored dissolved organic matter (CDOM) in inland and near-coastal bodies of waters has proven not only to be accurate and reliable, but also has given the possibility to expand the discrete sampling point coverage associated with traditional in-situ sampling. In recent years, the emergence of compact multispectral sensors and small Unoccupied Aerial Systems (sUAS) has opened possibilities of collecting higher resolution multispectral imagery with study specific revisiting periods and minimal impact from atmospheric effects (e.g., cloud cover) at substantially lower costs.

The main purpose of this dissertation was to use multispectral imagery captured with the help of an sUAS to create/develop finer and more accurate models to predict both optical and non-optical water quality parameters capable not only to monitor small bodies of water, but also sizeable lakes with multiple beneficial uses and diverse land use and land cover within their watersheds. For that purpose, four studies were designed that not only evaluate the capabilities of sUAS in monitoring and predicting water quality in small and sizable water bodies, but also to incorporate this technology into a holistic long-term project that focuses on improving water quality at the watershed scale.

Results indicate that: (1) with the use of imagery captured by an sUAS, and a thorough understanding of the existing relationships between water quality components in the systems involved, optical and non-optical water quality parameters can be reliably estimated, (2) when using a multiple linear regression approach, models capable of predicting optical and non-optical models (with strong prediction capability $R^2 \geq 0.80$) can be created, (3) multiple variable linear regression models in the visible portion of the electromagnetic spectrum best describe the relationship between TSS ($R^2 = 0.99$, *p*-value ≤ 0.01, n=15), SDD ($R^2 = 0.88$, *p*-value ≤ 0.01, n=15), Chl-a ($R^2 = 0.85$, *p*-value ≤ 0.01, n=15), Total Phosphorous ($R^2 = 0.98$, *p*-value ≤ 0.01, n=15) and Total Nitrogen ($R^2 = 0.98$, *p*-value ≤ 0.01, n=15), (4) although sUAS imagery increased the regression coefficients for the different evaluated models for this study compared to traditional remote sensing tools (e.g., Landsat 8 and Sentinel-2), the major limitations experienced when operating an sUAS are caused by flight restrictions, safety (improper piloting/ high wind speeds/ unclear airspace designations), battery life (≈20 minutes, which in turn decreases the size of the scene), and on-board sensor accuracy (large bandwidths and limited GPS precision), (5) 100% cloud free imagery can be collected with the use of sUAS, (6) the use of sUAS for water quality monitoring allows the user more flexibility in terms of temporal and spatial resolution, (7) current sUAS pre-processing tools are not capable of properly stitching images captured over large bodies of water, (8) generation of complete geolocated and radiometrically corrected true reflectance surfaces for large bodies of waters, allows for the estimation of optical water quality parameters using linear approaches, and (9) the use of sUAS in watershed monitoring programs has the potential to collect and provide information that can be used to enhance decision making and data collection.

CHAPTER 1 – Introduction

Remote sensing is defined "as the art, science, and technology of obtaining reliable information about physical objects and the environment, through the process of recording, measuring and interpreting imagery and digital representations of energy patterns derived from non-contact sensor systems" (Jensen, 2014). This process involves sending a natural (passive remote sensing) or artificial (active remote sensing) energy source to an object in order to register the amount of energy reflected by it and then processing and interpreting those data into useful information (Figure 1) (Khan et al., 2012). The most important characteristics of remote sensing in terms of resolution are: (1) Temporal (revisiting time of the sensor or mission collecting the data), (2) Radiometric (how much information is contained in each pixel), (3) Spatial (the physical dimensions of each pixel), and (4) Spectral (number of bands collected by the sensor). Due to this last characteristic, remote sensing tools are divided into three main categories: (1) Multispectral remote sensing (records information in multiple bands), (2) Hyperspectral remote sensing (records information in hundreds of bands) and (3) Ultraspectral remote sensing (records information in thousands of bands) (Jensen, 2007).

The history of remote sensing science dates to at least 1839 when photography was used to obtain information of the Earth's surface by taking pictures from balloons. By 1909, due to advances in transportation technology, photographs were taken from airplanes. In 1972, the first satellite designed to study and monitor the Earth's surface was launched (Landsat 1), enabling photography from space (Campbell, 1996). Since then, other Earth observing satellites such as: Terra (1999), Ikonos (1999), Landsat-7 (1999), Earth Observing-1 (2000), Meteosat-8 (2002), NOAA-17

(2002), Aqua (2002), SPOT-5 (2002), Envisat-1 (2002) and Landsat-8 (2013) have been launched (Kerle et al., 2004).

Currently, one of the many applications for this technology is the monitoring and prediction of water quality. In recent decades, the use of remote sensing tools for estimation of Secchi disk depth (SDD), total suspended solids (TSS), chlorophyll-a (Chl-a), and colored dissolved organic matter (CDOM) in inland and near-coastal bodies of waters has proven not only to be accurate and reliable, but also has given the possibility to expand beyond the discrete sampling point coverage associated with traditional in-situ sampling. However, there are major drawbacks using this technology, related to data loss due to cloud cover, limited temporal resolution, coarse spatial resolution, and the ability to monitor and predict only optical water quality parameters (e.g., TSS, SDD, Chl-a and CDOM).

In recent years, the emergence of compact multispectral sensors and small Unoccupied Aerial Systems (sUAS) has opened possibilities of collecting higher resolution multispectral imagery with study-specific revisiting periods and minimal impact from atmospheric effects (e.g., cloud cover) at substantially lower costs. With this in mind, the overall working hypothesis of this dissertation is that with the use of multispectral imagery captured with the help of an sUAS, finer and more accurate models to predict both optical and non-optical water quality parameters can be generated not only to monitor small bodies of water, but also sizeable lakes with multiple beneficial uses and diverse land use and land cover within their watersheds.

To accept or reject this overall hypothesis, the following chapters of this dissertation present four studies that not only evaluated the capabilities of sUAS in monitoring and predicting water quality in small and sizable water bodies (at different ends of the productivity spectrum), but also

incorporated this technology into a holistic long-term project that focuses on improving water quality at the watershed scale.

Chapters two and three describe the results of developing predictive algorithms using sUAS and then comparing them against algorithms developed from traditional satellite-based remote sensing tools for waters in different trophic states (e.g., low and high nutrient). Chapter two, "Prediction of Optical and Non-Optical Water Quality Parameters in Low and High Nutrient Aquatic Systems Using a Small Unoccupied Aerial System" (chapter accepted and published in *Drones* in 2020), focuses on developing different statistically reliable predictive algorithms for optical (TSS, SDD, Chl-a) and non-optical (total phosphorus (TP) and total nitrogen (TN)) water quality variables or indicators in an low nutrient system (Grand River Dam Authority (GRDA) Duck Creek Nursery Ponds) and a high nutrient system (City of Commerce, Oklahoma, Wastewater Lagoons) using remote sensing images from a sUAS equipped with a multispectral imaging sensor. Chapter three, "Is Bigger Always Better? Analysis of Models Developed from Small Unoccupied Aerial System Imagery Compared to Satellite Remote Sensing of Optical and Non-optical Water Quality Parameters" used the model from chapter two and compared them against two satellite-based remote sensing tools (Landsat 8 and Sentinel-2). Results indicate that: (1) with the use of imagery captured by an sUAS, and a thorough understanding of the existing relationships between water quality components in the systems involved, optical and non-optical water quality parameters can be reliably estimated and (2) although sUAS imagery increased the regression coefficients for the different evaluated models for this study compared to traditional remote sensing tools (e.g., Landsat 8 and Sentinel-2), the major limitations experienced when operating an sUAS are caused by flight restrictions, battery life and on-board sensor.

Once the capabilities of sUAS were tested in relatively small bodies of water, the focus of this dissertation was to implement the use of this model in larger bodies of water. However, current limitations in imagery pre-processing technology prevented full assessment of this idea. Due to that, Chapter 4, "Generation of Geolocated and Radiometrically Corrected True Reflectance Surfaces in the Visible Portion of the Electromagnetic Spectrum Over Large Bodies of Water using Images from an sUAS" (chapter accepted and published in the *Journal of Unmanned Vehicle Systems* in 2020) focuses on presenting a methodology to develop true reflectance surfaces in the visible portion of the electromagnetic spectrum from sUAS images obtained over large bodies of water when no ground control points were available. As a result of this work, generation of complete geolocated and radiometrically corrected true reflectance surfaces for large bodies of waters was accomplished.

Finally, chapter five, "Land Use/Land Cover Impacts on Water Quality Inside the Upper Horse Creek watershed – Understanding the Past in Order to Act in the Future", focused not only on the implementation of sUAS technology as part of a monitoring tool to improve water quality in a watershed scale, but also served as the first step to understand the dynamics that have driven water quality degradation in this watershed and to develop management options. From this work, results indicate that the use of sUAS in watershed monitoring programs has the potential to collect and provide information that can be used to enhance decision making and data collection.

CHAPTER 2 – Prediction of Optical and Non-Optical Water Quality Parameters in Low and High Nutrient Aquatic Systems Using a Small Unmanned Aerial System

Work presented in this chapter has been accepted and published in *Drones* 2020, 4(1), 1-21.

Abstract: The purpose of this study was to create different statistically reliable predictive algorithms for trophic state or water quality for optical (total suspended solids (TSS), Secchi disk depth (SDD), and chlorophyll-a (Chl-a)) and non-optical (total phosphorus (TP) and total nitrogen (TN)) water quality variables or indicators in an a low nutrient system (Grand River Dam Authority (GRDA) Duck Creek Nursery Ponds) and a high nutrient system (City of Commerce, Oklahoma, Wastewater Lagoons) using remote sensing images from a small Unoccupied aerial system (sUAS) equipped with a multispectral imaging sensor. To develop these algorithms, two sets of data were acquired: (1) In-situ water quality measurements and (2) the spectral reflectance values from sUAS imagery. Reflectance values for each band were extracted under three scenarios: (1) Value to point extraction, (2) average value extraction around the stations, and (3) point extraction using kriged surfaces. Results indicate that multiple variable linear regression models in the visible portion of the electromagnetic spectrum best describe the relationship between TSS ($R^2 = 0.99$, *p*-value = ≤ 0.01), SDD ($R^2 = 0.88$, *p*-value = ≤ 0.01), Chl-a ($R^2 = 0.85$, *p*-value = ≤ 0.01), TP ($R^2 = 0.98$, *p*-value = ≤ 0.01) and TN ($R^2 = 0.98$, *p*-value = ≤ 0.01). In addition, this study concluded that ordinary Kriging does not improve the fit between the different water quality parameters and reflectance values.

Keywords: remote sensing; small Unoccupied aerial system; water quality; optical and non-optical water quality parameters

2.1. Introduction

The United States Geological Survey (USGS), in their National Water Quality Assessment Program (NAWQA), defines water quality monitoring as a continuous period of data collection (in lakes, streams, rivers, reservoirs, wetlands, or oceans), in order to evaluate the chemical, physical, and biological characteristics of the body of water with respect to its ecological conditions and designated water uses (USG, 2019). Monitoring water quality typically involves a series of in-situ observations, measurements, and water sample collections that are analyzed for various parameters depending on the individual project goals, such as temperature, phosphorus (P), nitrogen (N), total solids, pH, fecal bacteria, conductivity, dissolved oxygen (DO), biochemical oxygen demand (BOD), hardness, alkalinity, suspended sediments, other nutrients, trace metals, and water clarity. Traditionally, water quality indicators are determined by the collection, field examination, and laboratory analyses of water samples, following consistent protocols and guidelines (Wilde, 2019).

Although properly collected and analyzed in-situ measurements are highly accurate, these measurements can be time-consuming, susceptible to errors (especially visual subjectivity), and can only be related to a specific point in time and space (Kloiber et al., 2002; Zhao et al., 2011). Due to these potential limitations, water quality monitoring programs that rely solely on these types of measurements may fail to provide accurate spatial or temporal views of water quality.

Considering the above constraints, the use of remote sensing and satellite imagery in water quality monitoring and management has been widely implemented to estimate different water quality parameters (Ritchie et al., 2003; Olmanson et al., 2008; Brezonik et al., 2008). Images from different Earth observing satellites (e.g., Landsat 5, Landsat 7, Landsat 8, Terra, Aqua, SPOT, among others) with the capability of obtaining information in the visible (0.4–0.8 μm), near infrared (0.8–1 μm) (NIR), and thermal (10–12 μm) portions of the electromagnetic (EM) spectrum, have been used to estimate different water quality parameters, such as total suspended solids (TSS), chlorophyll-a (Chl-a), pH, colored dissolved organic matter (CDOM), and Secchi disk depth (SDD). In case 1 waters (i.e., oceans), determination of optical properties is affected by phytoplankton. In case 2 waters (i.e., inland waters), determination of optical properties is more complex, due to the of presence of dissolved mineral sediments and organic matter (Kirk, 1998; Forget et al., 1999; Ritchie et al., 2003; Mobley et al., 2004; Morel et al., 2006; Baban, 2007; Olmanson et al., 2008; IOCCG, 2008; Dominguez et al. 2009, Duan et al., 2012, Matthews et al., 2012; Ma et al., 2015; Lee et al., 2016).

Satellite technology has proven not only to be able to obtain unbiased information on specific characteristics of lakes, but to also serve as a cost-effective complement to in-situ monitoring programs (Kloiber et al., 2002). The implementation of remote sensing and satellite imagery addresses two of the most important limiting factors when obtaining in-situ measurements: (1) The subjective error susceptibility associated with these types of measurements and (2) the limited, discrete sampling point coverage limitation (Ma et al., 2015).

Despite the benefits of using this technology, a major challenge when using optical imagery in observing and determining water quality parameters is its excessive susceptibility to data

limitations due to cloud cover (Lillesand et al., 1983; Giardino et al., 2001; Olmanson et al., 2008; Asner, 2010; Wilde, 2019). At the same time, most applications have focused on detection, determination, and prediction of optical water quality parameters like Chl-a, SDD, and CDOM (Giardino et al., 2001; Nelson et al., 2003; Torbick et al., 2008; Guan et al., 2011; Bonansea et al., 2015).

However, in recent years, the collection of high-resolution images using small Unoccupied aerial systems (sUAS) has become more prevalent (Colomina and Molina, 2014; Rusnak et al., 2018; Louhaichi et al., 2018; Doughty et al., 2019; Melville et al., 2019). Pairing sUAS with multispectral sensors may provide cloud free images with higher revisiting time (temporal resolution) and higher spatial resolutions at relatively low costs (Berni et al., 2009; Nebiker et al., 2016). Particularly, for water quality monitoring and modeling, different authors have developed site specific models using multispectral images collected with sUAS (Su and Chou, 2015; Kageyama et al., 2016). Su and Chou (2015) used a multispectral sensor onboard an sUAS in order to map the trophic state of Tain-Pu reservoir in Kinmen, Taiwan. As part of their findings, they determined that the ratio between multispectral bands has the ability to predict Chl-a, total phosphorous (TP), and SDD. At the same time, they corroborated that with the flexibility that sUAS offers not only in terms of temporal resolution; but also, with respect to higher spatial resolution, stronger regression models can be obtained. Kageyama et al. (2016) used an sUAS in order to perform water quality analysis in the Miharu reservoir in Japan. Their findings indicate that the ratios between multispectral bands are helpful to determine chemical oxygen demand (COD), TSS and Chl-a concentrations.

The main purpose of this study was to develop algorithms capable of estimating optical (TSS, Chl-a, SDD) and non-optical (TP and total nitrogen (TN)) water quality parameters in a low nutrient system and a high nutrient system using images collected with a multispectral sensor attached to an sUAS. Given the global economic and water security challenges posed by increasing nutrient over enrichment and resulting water quality degradation (Anderson et al., 2019; Schmale et al., 2019; Carlson, 2019), systems representing end members of the biological productivity spectrum were selected to generate robust and widely applicable models. Additionally, this study evaluates whether using a well-accepted statistical interpolation method improves the algorithms between the different water quality parameters and the reflectance values.

2.2. Materials and Methods

2.2.1. Study Areas

The area of research for this project involved two human-made pond systems, located on two opposite ends of the biological productivity spectrum. One is a low nutrient system, while the other one is a high nutrient system (Figure 2.1).

The low nutrient system (the Duck Creek Nursery ponds) was developed as an aquatic plant nursery and receive runoff from surrounding grasslands. The site is located in northeast Oklahoma (36.5691° N, −94.9676° W) (Figure 2.1a). The nursery ponds (NP) are a series of small ponds, ranging in surface area, located at the upstream part of the Duck Creek arm of Grand Lake O' the Cherokees (Grand Lake). Situated in a watershed of pasture/hay land use, yearly temperatures in the region range from −4 °C (in winter) to 33 °C (in summer) and yearly precipitation ranges from 4.78 cm (in winter) to 13.77 cm (in fall) (Mesonet, 2019). The land is owned and managed by the

Grand River Dam Authority (GRDA). These ponds are not hydrologically connected to Grand Lake, and are mainly recharged by surface run-off; however, when the water is excessively high in the reservoir (Grand Lake) these ponds serve a flood control function. Two adjacent ponds were included in this study.

The high nutrient system (the City of Commerce Wastewater Lagoons) is located in Commerce, Oklahoma (36.9334° N and −94.8730° W) (Figure 2.1b). The wastewater lagoons (CL) were reconstructed by the city of Commerce in 2014 and their purpose is to provide primary treatment for the city's municipal wastewater. The primary input of untreated wastewater to these lagoons has excess nitrogen (N), phosphorous (P), and carbon. Domestic wastewater from Commerce enters the system via a clarifier. After a hydraulic retention time (HRT) of 24 h, the clarifier effluent splits into two flow paths. One half of the wastewater goes to the north wastewater lagoon, while the other half goes to the south wastewater lagoon. At each lagoon, wastewater is exposed to sunlight for a period of 3–4 days. The exposure to sunlight contributes to the growth of algae, and the algae builds biomass in order to promote bacteria growth. These bacteria break down the waste present in the water (ODEQ, 2019). After adequate HRT, both lagoons discharge their effluent into a third wastewater lagoon that serves as an environmental buffer before discharging the treated effluent to the nearest tributary located at the north-east part of the parcel, in the Grand Lake watershed. Due to its proximity to the Nursery Ponds (which are approximately 40 km south southwest), yearly temperatures and precipitation are similar. The north lagoon was included in this study.

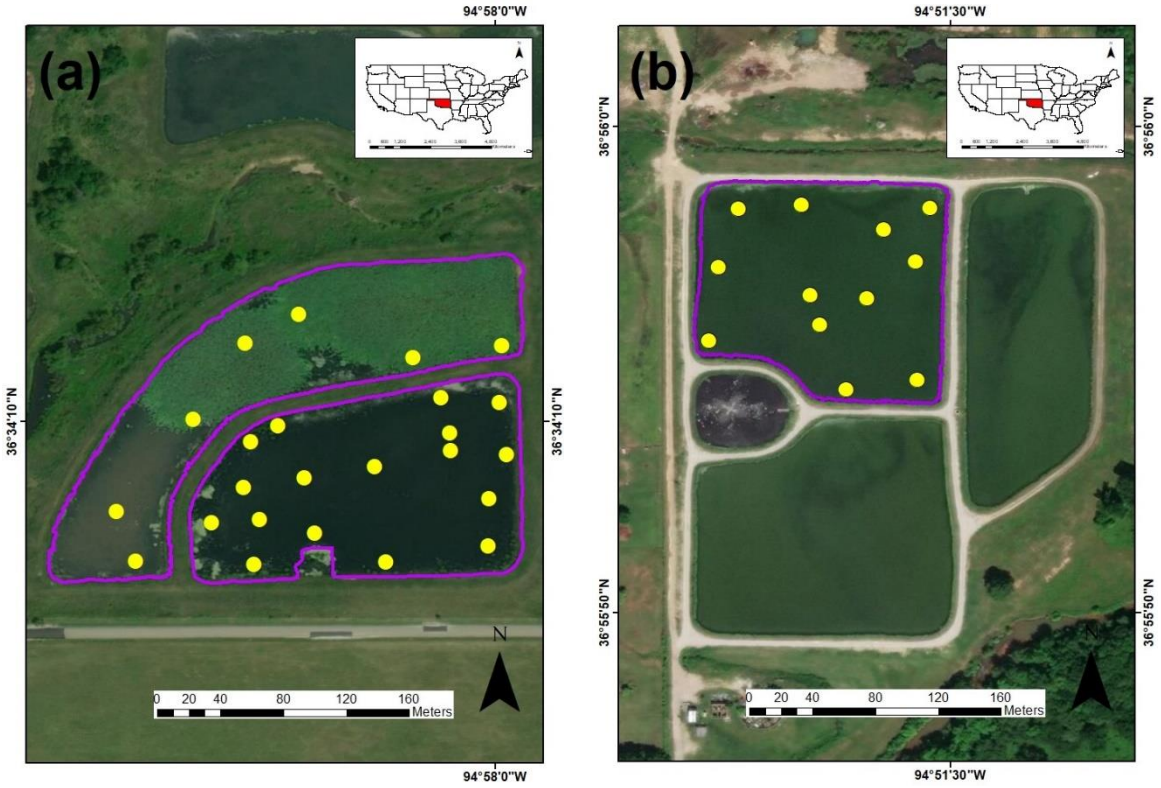

Figure 2.1. Location of the low and high nutrient systems and sampling stations at each system (yellow dots). (a) Nursery pond, Ottawa County, Oklahoma. (b) Wastewater Lagoons, City of Commerce, Ottawa County, Oklahoma.

2.2.2. Water Quality and Multispectral Imagery Data Collection

In total, 36 water samples were collected (24 at the Nursery Ponds and 12 at the Wastewater Lagoons) (Figure 2.1). At each sampling location, a Secchi Disk Depth (SDD) reading was taken using a 30-cm Secchi Disk attached to a measuring tape. Once completed, one water sample was collected using a 4.2-L PVC depth-discrete horizontal water sampler submerged 0.5 m from the water's surface. Before sample collection, the sampler was rinsed three times with sample water. Once collected, water was divided into four portions. A first portion was transferred to a 250-mL high-density polyethylene (HDPE) bottle for field analyses (turbidity). A second portion was transferred to another 250-mL HDPE bottle to be analyzed for total nitrogen (TN) and total

phosphorus (TP). A third portion was transferred to a 1-L dark bottle to be analyzed for chlorophyll-a (Chl-a). Finally, the remaining portion of the sample was transferred to a 1-L bottle to be analyzed for total suspended solids (TSS). Once samples were generated, they were placed into a cooler with ice at 4 °C for later analysis. A calibrated YSI 600 multiparameter data sonde (YSI, 2019) was then deployed to obtain dissolved oxygen (DO), temperature, specific conductance, salinity, and pH data. Calibration checks were performed using pH 7 buffer, 1000 μS/cm conductivity solution, and water saturated air (for DO) during and after sample collection. All samples were collected and preserved according to procedures from the U.S. Environmental Protection Agency (EPA, Washington, DC, USA) (USEPA, 2002).

Multispectral imagery was collected using an ATI AgBot sUAS (Aerial Technology International, Oregon City, Oregon, USA) (Figure 2.2a) equipped with a MicaSense RedEdge multispectral sensor (MicaSense Inc., Seattle, Washington, USA) (Figure 2.2b), capable of obtaining information in the blue (0.475 μm), green (0.560 μm), red (0.668 μm), red edge (0.717 μm), and NIR (0.840 μm) portions of the spectrum. The ATI AgBot is a vertical takeoff and landing (VTOL) carbon fiber frame four-rotor quadcopter (Tri-prop and 4012 400 Kv motors). Onboard, the ATI AgBot carries two dual 6S 6500 mAh lithium polymer (LiPo) battery packs (Pulse Battery, Middletown, Indiana, USA) (that allow for 26+ minutes of flight time), UBlox GPS, compass module and a MicaSense RedEdge multispectral sensor. The MicaSense RedEdge multispectral sensor is a digital frame camera that has a ground sample distance of 8 cm per pixel (per band) at 120 m above ground level (AGL), a capture rate of 1 capture per second (in all bands), a 16-bit radiometric resolution, and a 47.2° horizontal field of view (HFOV). The sUAS lacks a sun irradiance sensor, so this information was supplemented with pre- and post-photographs (taken with the MicaSense sensor) of MicaSense's calibration reflectance panels in order to improve

reflectance in situations where light conditions change during the flight. Including the sensor and batteries, the entire setup weighs 4.7 kg. (ATI, 2019).

(a) **(b)**

Figure 2.2. Small unnamed aerial system used to collect multispectral data (a) and MicaSense RedEdge multispectral sensor (b).

To georeference the multispectral images taken with the RedEdge sensor, information from the GPS was transferred to the images via the UBX binary protocol using the NAV and RXM data classes (Mesonet 2019b). Differential GPS (DGPS) was obtained using Mission Planner 1.3.68 (Mission Planner, 2019). No ground control points (GCPs) were defined before the mission (because the mission was flown over water); however, the inertial navigation system (INS) onboard the sUAS provided continuous position, orientation, and velocity of the aircraft. All of this information was transmitted to a ground control station using Mission Planner 1.3.68. Two multiple-waypoint missions were designed in Mission Planner 1.3.68. All missions were flown at an altitude of 100 m with a flying speed of 5 m/s, and estimated flight time of 10 min. For the Nursery Ponds, a total of 164 images with a ground resolution of 6.20 cm were obtained. For the Wastewater Lagoons, a total of 46 images with a ground resolution of 6.20 cm were obtained. Figure 2.3 presents the flight paths for imagery collection at the Nursery Ponds (2.3a) and

Wastewater Lagoons (2.3b), respectively. Multispectral imagery was acquired the same day as the in-situ water samples.

(a) **(b)**

Figure 2.3. Small Unoccupied aerial system (sUAS) flight path (yellow arrow) and imagery footprint (with number of overlapping pictures) at the Nursery Ponds (a) and Wastewater Lagoon (b).

2.2.3. Methodology

The workflow for this study was divided in four phases: (1) Data collection, (2) data processing, (3) model development, and (4) validation (Figure 2.4).

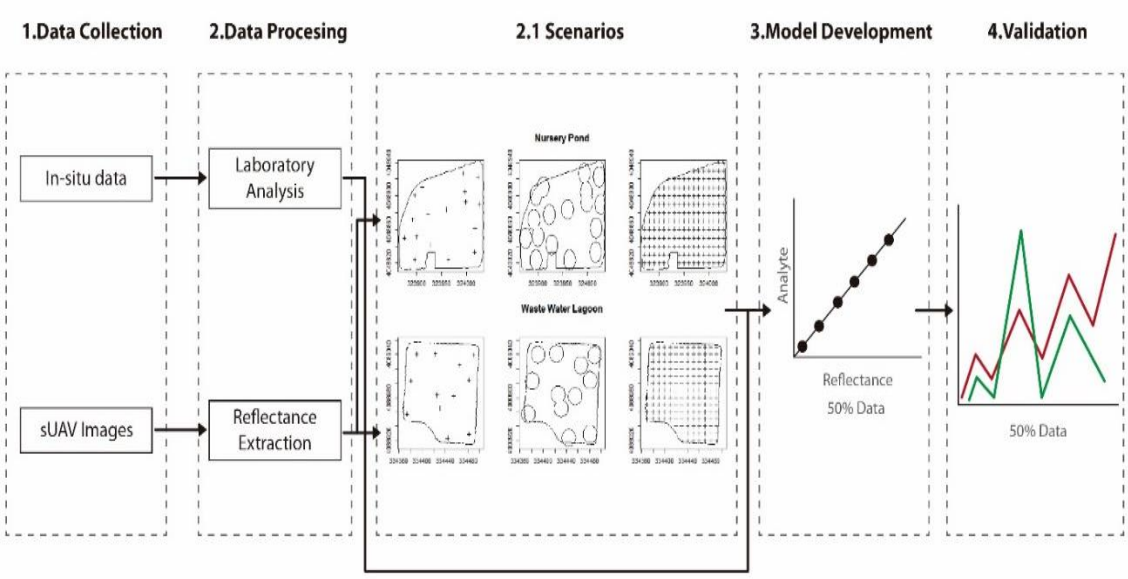

Figure 2.4. Overview of created methodology for the development to statistical water quality models for optical and non-optical water quality parameters.

2.2.3.1. Data Collection

For the Nursery Ponds, in-situ water quality and multispectral imagery collection took place on 12 July 2017, beginning at 11:00 A.M. CST. For the Wastewater Lagoons, in-situ water quality and multispectral imagery collection took place on 8 September 2017, beginning at 2:00 P.M. CST. Multispectral imagery was acquired the same day as the in-situ water samples. Table 2.1 presents the time window between multispectral data collection and water sample acquisition, using the ending time of the sUAS missions as the reference point.

Table 2.1. Time window between multispectral imagery collection and water samples acquisition for the low and high nutrient systems. NP refers to Nursery Pond and CL refers to Wastewater Lagoons.

Nursery Ponds				Wastewater Lagoons	
Site ID	**Window (minutes)**	**Site ID**	**Window (minutes)**	**Site ID**	**Window (minutes)**
NP-1	+17	NP-13	+151	CL-1	+22
NP-3	+33	NP-14	+154	CL-2	+38
NP-4	+46	NP-15	+161	CL-3	+47
NP-5	+58	NP-16	+198	CL-4	+57
NP-6	+67	NP-17	+210	CL-5	+68
NP-7	+78	NP-18	+216	CL-6	+79
NP-2	+86	NP-19	+226	CL-7	+86
NP-8	+101	NP-20	+347	CL-8	+97
NP-9	+111	NP-21	+360	CL-9	+108
NP-10	+121	NP-22	+370	CL-10	+114
NP-11	+131	NP-23	+379	CL-11	+125
NP-12	+144	NP-24	+389	CL-12	+130

2.2.3.2. Data Processing

Laboratory Analysis

After collection, all water samples were analyzed for TSS, Chl-a, TP, and TN following the methods presented in Table 2.2. Chl-a samples were filtered through individual glass fiber filters in order to perform pigmentation extraction using 90% acetone, then Chl-a concentrations were measured using a Trilogy laboratory fluorometer at 460 nm. TP samples were individually mixed with a solution of 5N sulfuric acid (H_2SO_4), antimony potassium tartrate ($C_8H_{10}K_2O_{15}Sb_2$), ammonium molybdate ($(NH_4)_2MoO_4$), and 0.1M ascorbic acid ($C_6H_8O_6$), and TP concentrations

were measured using a Cole Parmer 2800 UV VIS spectrophotometer at 650 nm. TN samples were individually mixed with a solution of 3N sodium hydroxide (NaOH), potassium persulfate ($K_2S_2O_8$), nicotinic acid p-toluenesulfonate ($C_{13}H_{13}NO_5S$), and adenosine triphosphate ($C_{10}H_{16}N_5O_{13}P_3$), and TN concentrations were measured with a Lachat Quikchem 8500 series 2 flow injection analysis system. Finally, TSS samples were filtered through individual glass fiber filters (Gelman type A/E), then dried at 105 °C for at least one hour. TSS concentrations were determined by mass difference for the volume of filtered sample.

Table 2.2. Water quality analytes and methods.

Analyte	Method
Chlorophyll α	EPA 445.0
Total Phosphorus	APHA 4500-P J
Total Nitrogen	APHA 4500-P J
Total Suspended Solids	EPA 160.2

Reflectance Extraction

In order to perform the extraction of the reflectance values from the multispectral imagery, three scenarios were conducted (Figure 2.5): (1) Value to point extraction (Figure 2.5a), where the georeferenced position of each sampling station was used in order to extract the reflectance; (2) average buffer value extraction (Figure 2.5b), where a buffer zone of 3 m was created around the georeferenced position of each sampling station in order to extract the average reflectance (the distance of this buffer zone was defined based on the offset distance of the GPS units); and (3) Kriging extraction (Figure 2.5c), where kriged surfaces (using ordinary Kriging) were developed for each of the analytes in order to extract the reflectance values of 319 points (low nutrient system) and 162 points (high nutrient system) inside each created surface. This last scenario was created

in order to simulate a hypothetical situation where water samples could be collected from the entire surface of the systems and to determine if the "collection" of more samples (represented by the centroids of each pixel inside the systems) could improve the predictive capability of the models. Ordinary Kriging was selected as the interpolation statistical method because concentration estimations (for the different water quality parameters) were to be determined at unsampled locations with minimal error. All imagery stitching and preprocessing were performed in PiX4Dmapper 4.4.9 (PiX4Dmapper, 2011), while the reflectance extractions were performed using ArcMap 10.6 (ArcMap, 2012).

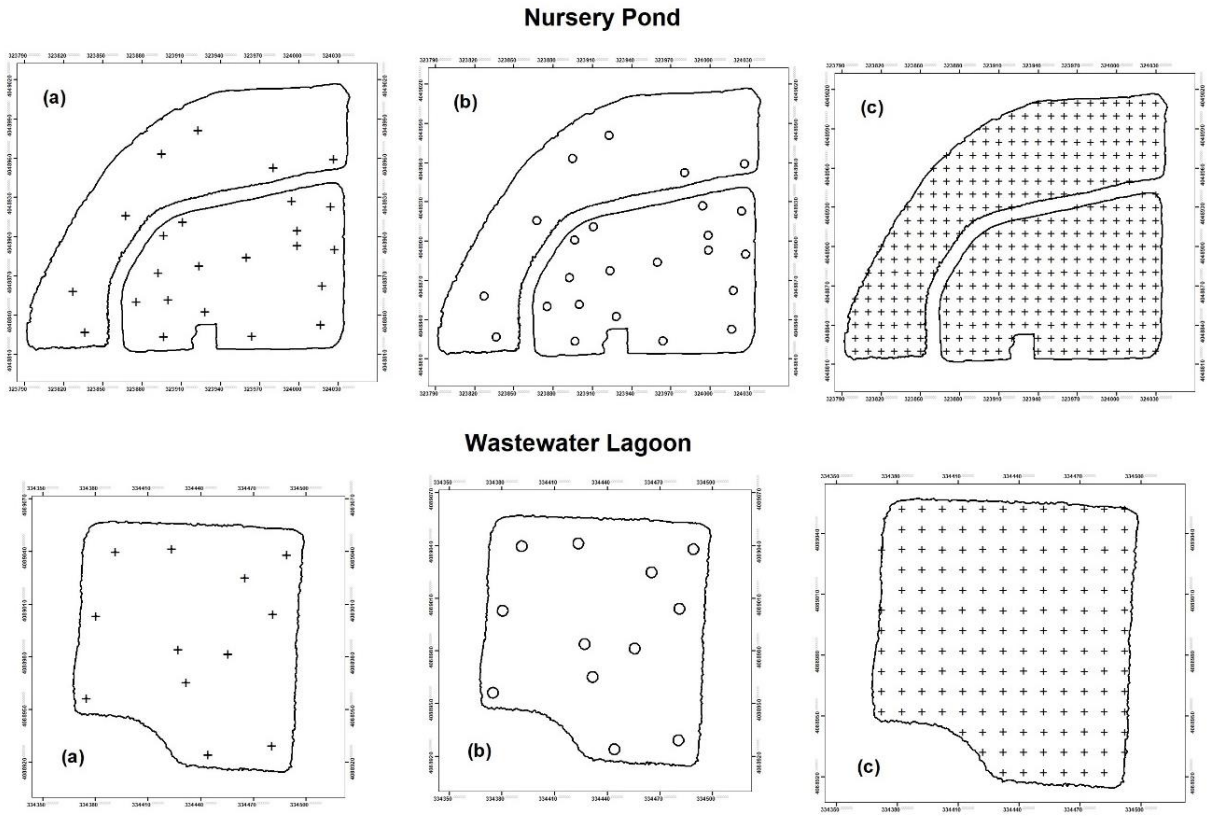

Figure 2.5. Evaluated reflectance extraction scenarios: Point extraction (a), buffer extraction (b), and Kriging extraction (c).

2.2.3.3. Model Development and Validation

To ensure equal spatial distribution between both systems, the overall data generated in each system were randomly divided into two subsets. Each subset was then merged with its counterpart. As a result, 50% of the data were used for model development, while the other half was used for model validation.

The models were developed using single variable and multiple variable linear model regression approaches. The untransformed data from in-situ TSS, Chl-a, SDD, TP, and TN values were used as the dependent variables, while the untransformed reflectance of each band, and different ratios between them, were used as the independent variables. The best fit was determined using the coefficient of determination (R^2) and the small sample corrected Akaike information criterion (AICc) (Akaike, 1971; Burnharm et al, 2002). Once the best fit for each analyte was determined, the remaining 50% of the data were used for validation. Statistical difference was determined using a paired sample *t*-test (*p*-value ≥ 0.05) given the normal distribution of the entire dataset (Shapiro–Wilk test (Shapiro and Wilk, 1965) *p*-value ≥ 0.05). All statistical analyses were conducted in R 3.5.1 (R Core Team, 2017).

2.3. Results

2.3.1. Water Quality

Two systems located at the opposite sides of the biological productivity spectrum were selected for this study. Figures 2.6 and 2.7 present the water quality results for the low and high nutrient systems, respectively.

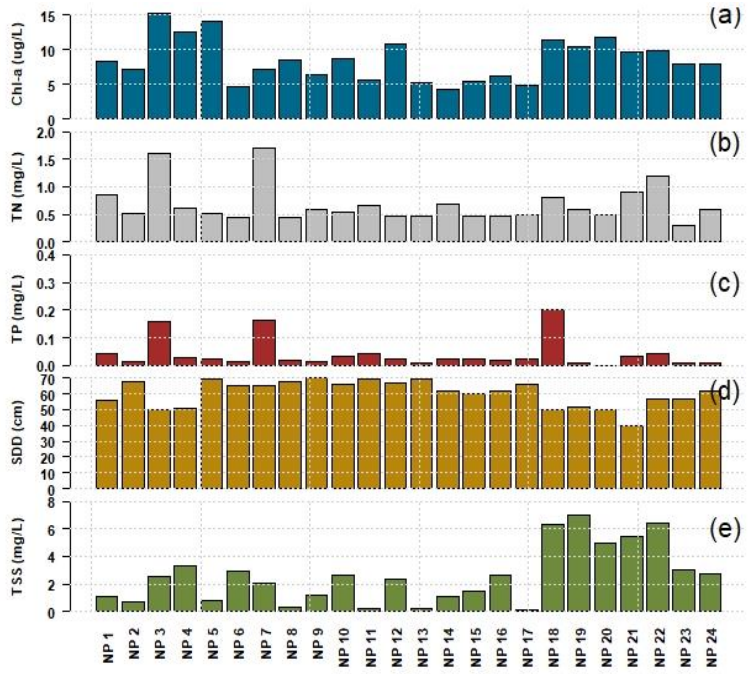

Figure 2.6. Water quality results for the Nursery Ponds (NP) (low nutrient system). (a) Chlorophyll-a, (b) total nitrogen, (c) total phosphorous, (d) Secchi disk depth, and (e) total suspended solids.

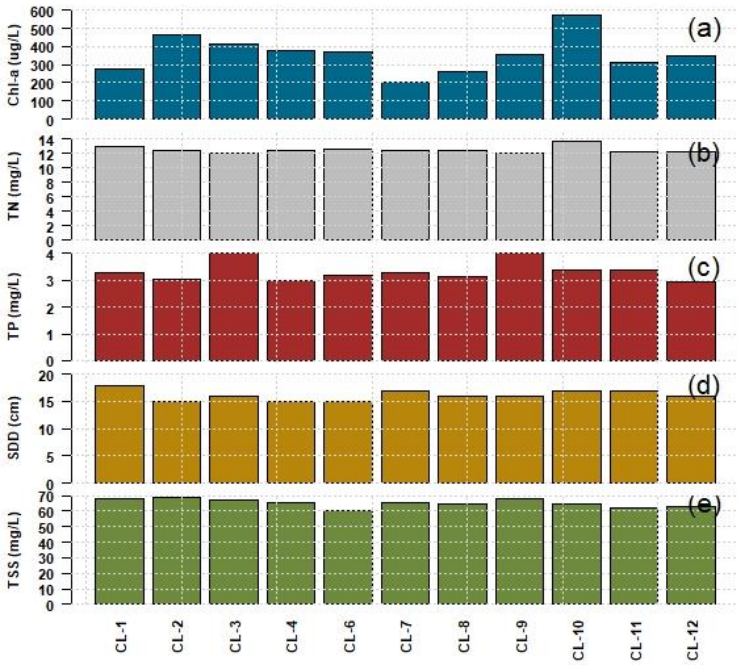

Figure 2.7. Water quality results for the Wastewater Lagoons (CL) (high nutrient system). (a) Chlorophyll-a, (b) total nitrogen, (c) total phosphorous, (d) Secchi disk depth, and (e) total suspended solids.

For the analyzed water quality parameters, substantial differences can be observed between the two systems. Table 2.3 shows the statistical summary (and comparisons) between the water quality parameters measured at the low and high nutrient systems.

Table 2.3. Descriptive statistics and comparison between water quality parameters at the low and high nutrient systems. SD refers to standard deviation. Units are μg/L for Chl-a, mg/L for TN, TP and TSS, and cm for SDD.

	Low Nutrient System					**High Nutrient System**				
	Mean	**Median**	**SD**	**Min**	**Max**	**Mean**	**Median**	**SD**	**Min**	**Max**
Chl-a	8.52	8.10	3.08	4.26	15.37	358.3	352.60	103.36	200.40	575.80
TN	0.68	0.56	0.35	0.30	1.71	12.47	12.40	0.47	12.00	13.60
TP	0.04	0.02	0.05	0.01	0.20	3.33	3.27	0.37	2.94	4.02
SDD	60.4	62.00	8.18	40.00	70.00	16.18	16.00	0.98	15.00	18.00
TSS	2.44	2.57	2.09	0.11	7.00	65.33	65.20	2.7	60.20	68.83

2.3.2. Reflectance Extraction

Three scenarios were evaluated under the reflectance extraction procedures: (1) Point extraction, (2) buffer extraction, and (3) Kriging extraction. Figures 2.8 and 2.9 present the reflectance values of the low and high nutrient systems as a function of the individual stations evaluated in each scenario.

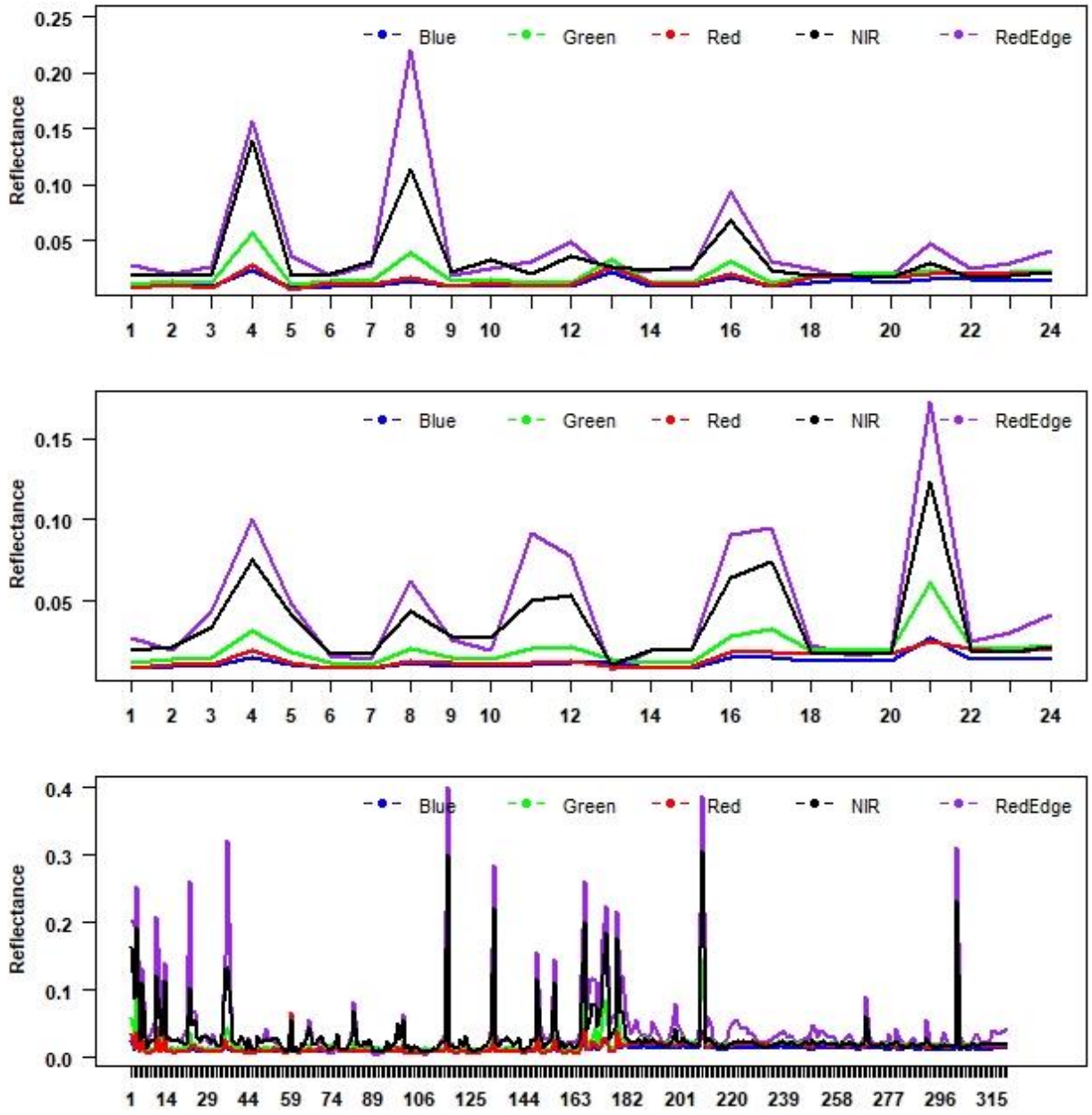

Figure 2.8. Reflectance values (y-axis) as a function of the number of stations (x-axis) evaluated in the reflectance extraction scenarios. (a) Point extraction, (b) buffer extraction, and (c) Kriging extraction for the low nutrient system.

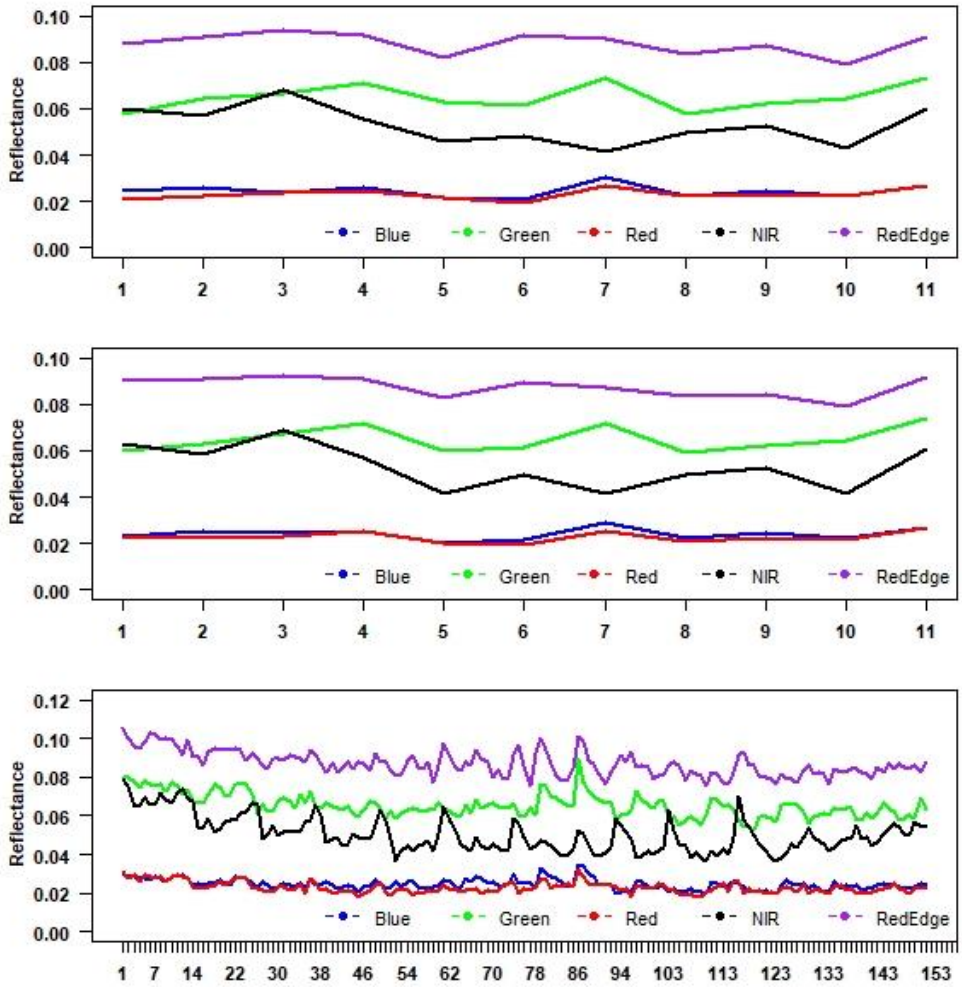

Figure 2.9. Reflectance values (y-axis) as a function of the number of stations (x-axis) evaluated in the reflectance extraction scenarios. (a) Point extraction, (b) buffer extraction, and (c) Kriging extraction for the high nutrient system.

From the reflectance values as a function of sampling stations, it can be observed that each system provides different relationships, indicating distinct compositions and characteristics. In the low nutrient system, light reflects more than in the high nutrient system indicating clearer waters.

2.3.3. Models Development and Extraction Scenarios Evaluation

Using a single variable linear model regression approach, a total of 315 models (single bands and band ratios) were developed under the three extraction scenarios (105 models per extraction

scenario). For this purpose, the independent variable was defined as the reflectance values from the different bands available from the multispectral sensor and the dependent variable was the in-situ measurements for the different water quality parameters. Considering the predictive capabilities of each model (under each evaluated scenario), it was determined that the point extraction scenario had stronger predictive capabilities (maximum R^2 and minimum AICc values) for all the analyzed parameters (Figure 2.10).

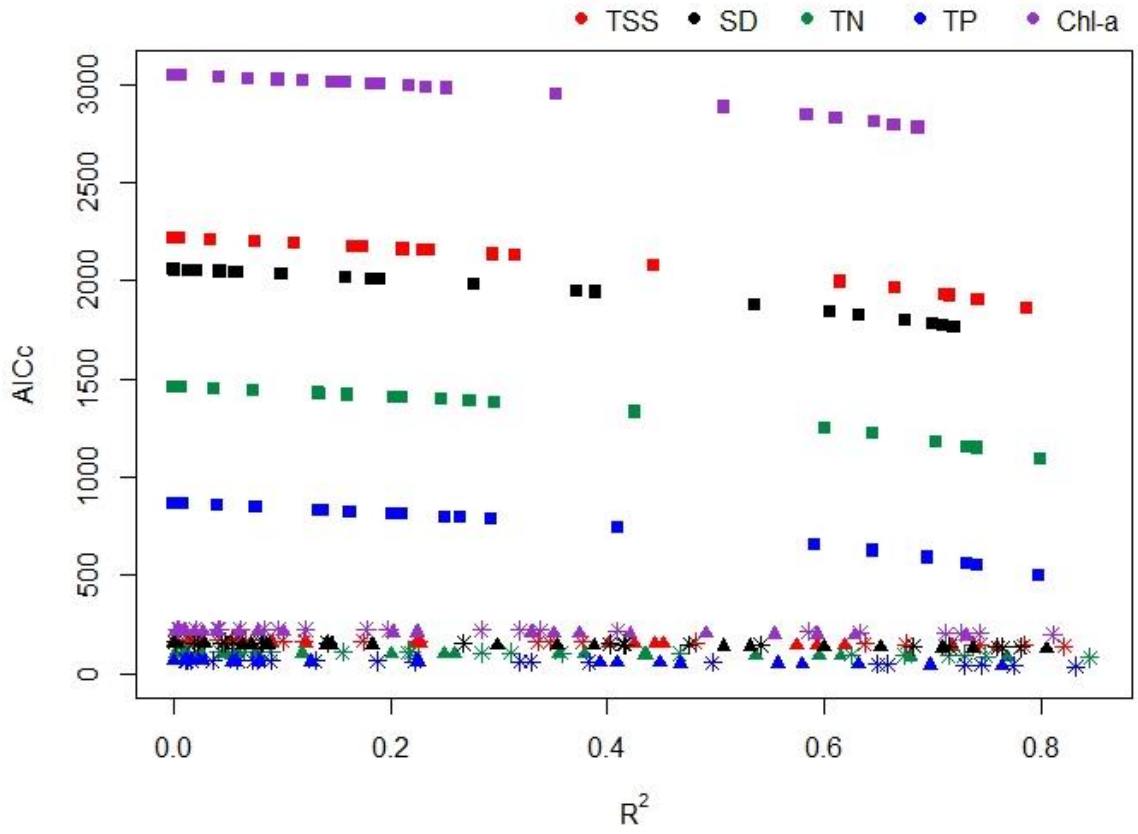

Figure 2.10. Prediction capabilities of all developed models under three extraction scenarios: (1) Point extraction (asterisks), (2) buffer extraction (triangles), and (3) Kriging extraction (squares), using a single variable regression approach.

In order to improve the predictive capabilities of each model developed under the point extraction scenario, a multiple variable linear regression approach was used. Table 2.4 presents the best performing (highest R^2) models for all evaluated water quality parameters, using single and

multiple variable linear approaches. From this table, it can be observed that for all water quality parameters, a multiple variable model yielded a higher R^2. Table 2.5 presents the estimated statistical coefficients for the multiple linear regression analysis.

Table 2.4. Best predictive water quality models using single and multiple variable linear approaches. WQP refers to the specific water quality parameter, while m and b are estimated coefficients fitting the regression analysis.

WQP	Single Variable Model	R^2	Multiple Variable Model	R^2
SDD	=m*(Green) + b	0.781	=m*(Blue/Red) − m*(Green/Red) + m*(Green/Blue) − b	0.888
TSS	=m*(Green/Red) − b	0.821	=m*(Blue/Red) − m*(Green/Red) + m*(Green/Blue) + b	0.987
TN	=m*(Green/Red) − b	0.845	=m*(Blue/Red) − m*(Green/Red) − m*(Green/Blue) + b	0.979
TP	=m*(Green/Red) − b	0.832	=m*(Blue/Red) − m*(Green/Red) + m*(Green/Blue) + b	0.984
Chl-a	=m*(Green/Red) − b	0.810	=m*(Green) – m*(Red) + b	0.846

Table 2.5. Estimated coefficients from multiple regression analysis.

WQP	Slope (m)					y-Intercept (b)
	$\frac{Blue}{Red}$	$\frac{Green}{Red}$	$\frac{Green}{Blue}$	Green	Red	
SDD	164.32	108.33	78.67	--	--	61.91
TSS	264.5	148.2	185.2	--	--	215.3
TN	45.43	26.16	32.94	--	--	36.92
TP	12.441	6.993	8.810	--	--	9.953
Chl-a	--	--	--	9158.79	13,359	27.99

2.3.4. Validation and Spatial Distribution Maps

The developed models and their respective equations were validated using the remaining 50% of the data. Using this validation dataset as input for the models (Table 2.4), calculated water quality values were generated and compared against the actual in-situ measurements. Given that the R^2 values calculated for each selected model were so close to unity, bias and scatter—both of which evaluate the difference between the predicted values of the model and the real value to be predicted—were very small.

Figure 2.11 presents a comparison between the actual and predicted optical and non-optical water quality parameters. Further evaluation of the calculated water quality data indicates that the distribution of created data followed a normal distribution (Shapiro-Wilk test *p*-value ≥ 0.05 for all parameters) and that statistically there was no difference between the calculated values and the collected in-situ values (*t*-test *p*-value ≥ 0.05 for all parameters).

Once it was determined that there was no statistical difference between the calculated values and the collected in-situ values, band arithmetic function (following the models' equations) was applied to the collected multispectral images in order to establish spatial distribution maps for all of the water quality parameters in the low (Figure 2.12) and high (Figure 2.13) nutrient systems.

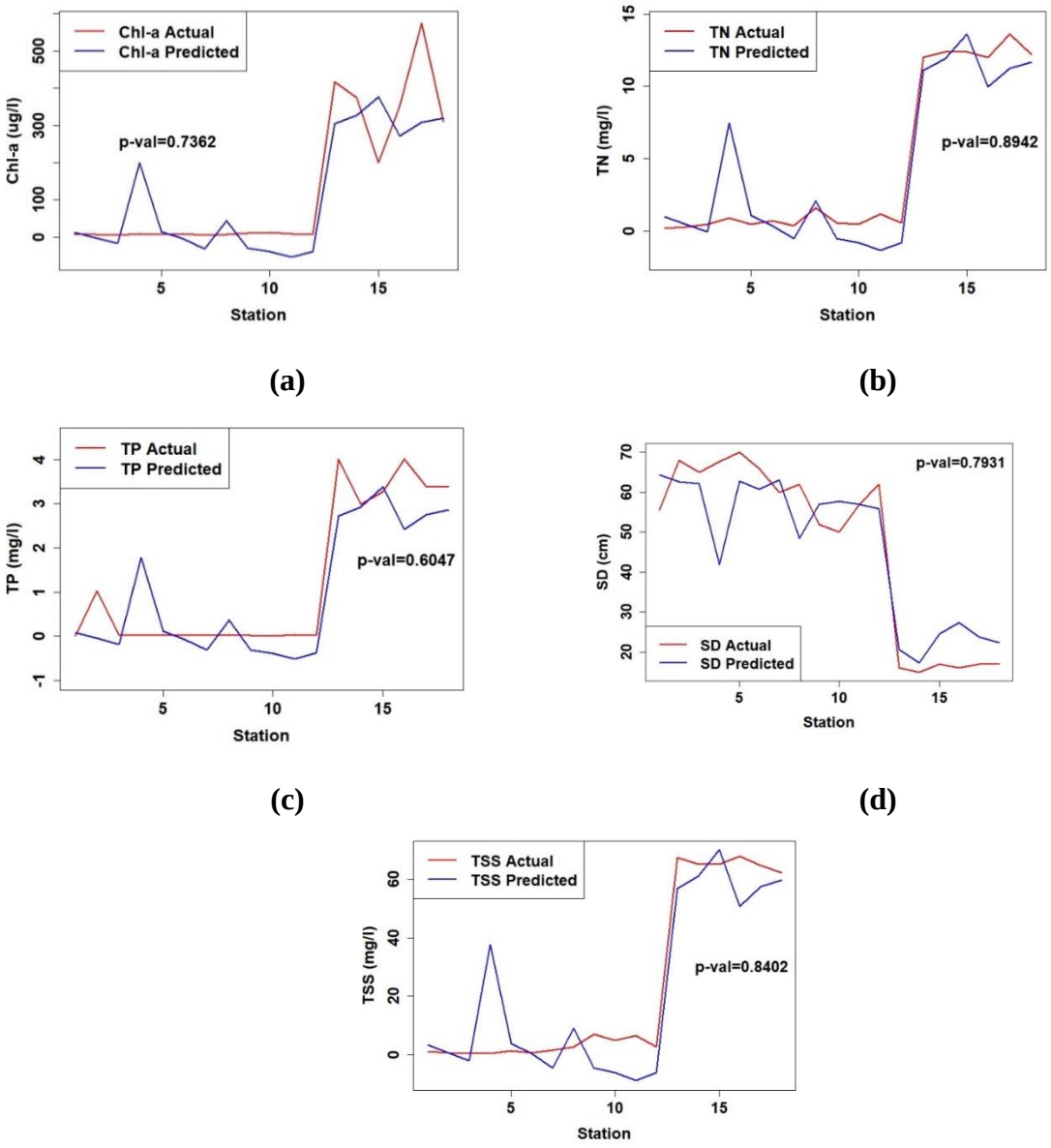

Figure 2.11. Multiple variable models' comparisons of the actual and predicted optical and non-optical water quality parameters. (a) Chlorophyll-a, (b) total nitrogen, (c) total phosphorous, (d) Secchi disk depth, and (e) total suspended solids.

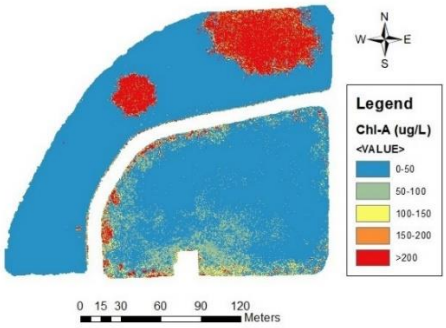

(a)

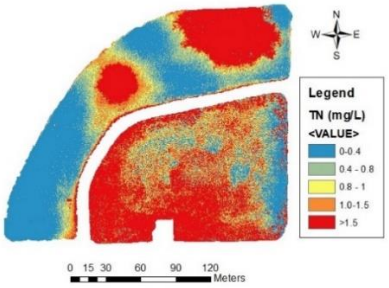

(b)

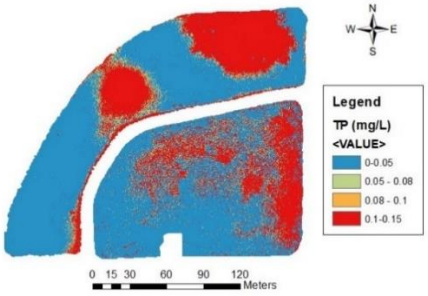

(c)

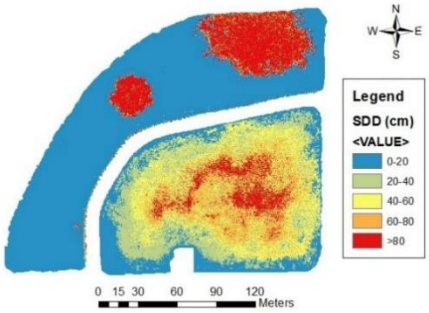

(d)

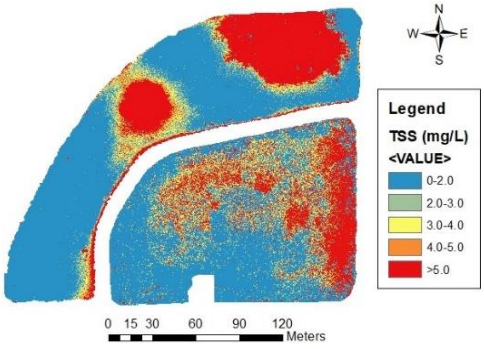

(e)

Figure 2.12. Spatial distribution maps for the estimated water quality parameters in the low nutrient system. (a) Chlorophyll-a, (b) total nitrogen, (c) total phosphorous, (d) Secchi disk depth, and (e) total suspended solids.

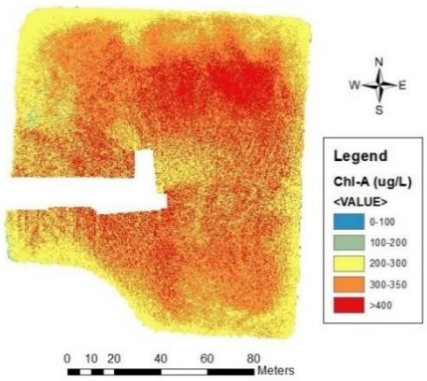

(a)

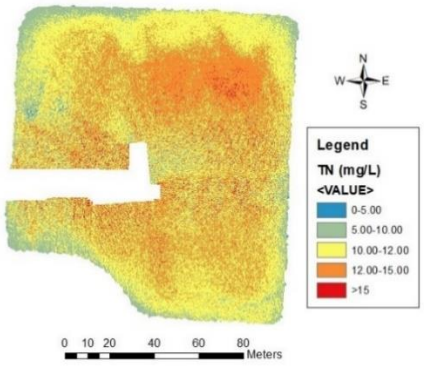

(b)

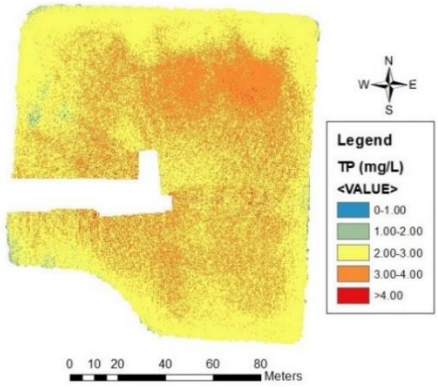

(c)

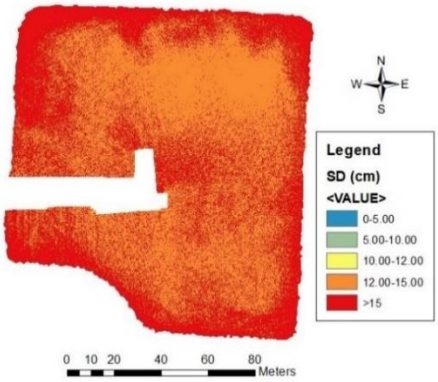

(d)

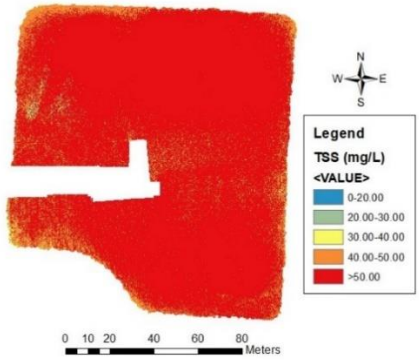

(e)

Figure 2.13. Spatial distribution maps for the estimated water quality parameters in the high nutrient system. (a) Chlorophyll-a, (b) total nitrogen, (c) total phosphorous, (d) Secchi disk depth, and (e) total suspended solids. Whited-out sections are due to the inability of the pre-processing software to properly stich images at those locations.

From the generated spatial distribution maps, it can be observed that both systems (low and high nutrient) present fully mixed waters (which correlates to the water quality analyses presented in Section 2.3.1). Also, it is important to note from the distribution maps for the oligotrophic system, that aquatic features present during the image capturing process (aquatic vegetation, located at north and northeast portion of pond) can be clearly identified from the different optical water quality measurements. At the same time, from Figure 2.13, it can be observed that that in all distribution maps, there are whited-out sections. These sections are due to the inability of the pre-processing software to properly stich images at those locations.

2.4. Discussion

The main purpose of this study was to develop models capable of reliably estimating optical (TSS, Chl-a, and SDD) and non-optical (TP and TN) water quality parameters in two extremes of the aquatic biological productivity spectrum (low and high nutrient systems), using in situ data and images collected with a multispectral sensor attached to an sUAS. In order to develop these algorithms, linear approaches using single and multiple variables were used. As a result, it was determined that linear models using multiple variables had stronger predictive capabilities for all water quality parameters. These algorithms have the capability of generating data that are not statistically different from the collected in-situ data for optical and non-optical water quality parameters.

In the paper “Comprehensive Review on Water Quality Parameters Estimation Using Remote Sensing Techniques”, Gholizabeh et al. (2016) references that different authors determined that the use of visible and near infrared bands of the EM spectrum from multispectral sensors can be used to obtain strong correlations between reflectance and optical water quality parameters.

However, when exploring correlations for non-optical parameters, direct inference of these measurements had low predictive capabilities. Lim and Choi (2015) used Landsat 8 in order to correlate spectral bands with in-situ water quality measurements, in order to establish water quality models capable of estimating optical (TSS and Chl-a) and non-optical (TN and TP) parameters in the Nakdong River in Korea. As a result, they obtained algorithms that strongly estimated TSS and Chl-a (R^2 = 0.74 and 0.71, respectively), but were not as strong when estimating TP and TN (R^2 = 0.50 and 0.48, respectively). Due to this limitation, an indirect estimation approach has been taken by some authors in order to develop strong correlations that relate TP and TN to Chl-a concentrations and SDD (Wu et al., 2010; Sharaf and Shang, 2017).

When examining the multiple variable models determined by this study (Table 2.4), it can be observed that the combination between the ratios Blue/Red, Green/Red, and Green/Blue provide the strongest correlation between reflectance and most of the optical and non-optical water quality parameters (except for Chl-a, for which the highest correlation was obtained with the Green and Red bands). These findings are in accordance with Gholizabeh et al. (2016); however, it was determined by this study that these ratios not only have the capability of estimating optical parameters, but also non-optical values. Lui et al. (2017) determined that with the use of high-resolution imagery, linear (multiple linear regression) and non-linear (artificial neural network) models with strong predictive capabilities could be developed for TN and TP. The basis of these relationships is explained by the high spectral correlation that TN and TP have with SDD, TSS, and Chl-a (Song et al., 2012).

It is imperative to begin this discussion with this information because the study presented herein deviates from the traditional approach of using multispectral sensors attached to satellite platforms.

Instead, this study uses a more compact multispectral sensor, attached to an sUAS. By doing this, not only can direct methods of estimating non-optical water quality parameters be derived, but the use of this tool enhances spatial and temporal resolutions while eliminating the cloud coverage issues.

Earth observation satellites are the most common platforms to monitor and collect information about the Earth (Liu et al., 2013). Table 2.6 presents some of the most common remote sensing satellites used for estimating water quality parameters, along with their respective spatial and temporal resolutions. From this table, it can be determined that the spatial resolution obtained by any of these platforms is much coarser when compared to the spatial resolution (6–8 cm) obtained with the sensor used in this study. To illustrate this concept, Figure 2.14 presents a visual comparison between images taken from two commonly used remote sensing satellites (Landsat 8 and Sentinel-2A) versus the images captured by the sUAS in the high nutrient system used in this study. By looking at these aerial images, the pixel resolution significantly increases in the picture taken with the sUAS.

The use of satellite remote sensing tools helps to expand the limited discrete sampling point coverage of traditional monitoring plans (Kloiber et al., 2002; Olmanson et al., 2008; Bonansea et al., 2015; Allan et al., 2011; Mushtaq and Nee Lala, 2017). However, in addition to spatial resolution, two major drawbacks when using these tools are: (1) The longer revisiting time (temporal resolution) of these platforms and (2) cloud coverage limitations. Zhang and Kovacs (2012) point out that the longer temporal resolutions of some of these platforms presents a major difficulty when trying to monitor systems that are in a constant state of change. At the same time, other authors mention that the number of images that they are unable to be used due to cloud

coverage accounts in some cases for up to 97% of the available captured imagery for a particular region in a 25-year period (Kloiber et al., 2002). With the use of sUASs, these issues are no longer a concern. First, with an sUAS, the operator has the flexibility of deciding how often they want to capture multispectral imagery. Secondly, because sUAS fly below the clouds, all the imagery is 100% cloud coverage free.

Table 2.6. Spatial and temporal resolutions of some of the most commonly used remote sensing satellites for water quality estimation, compared to the sUAS used in this study.

Satellite	Spatial Resolution	Temporal Resolution (Day)
Landsat–5	30 m	16
Landsat–7	30 m	16
Landsat–8	30 m	16
QuickBird–2	15 m	1–3
Orb View–3	4 m	3
Gaofen–1	8 m	4
Sentinel–2	10 m	5
sUAS	0.06–0.08 m	Flight-specific

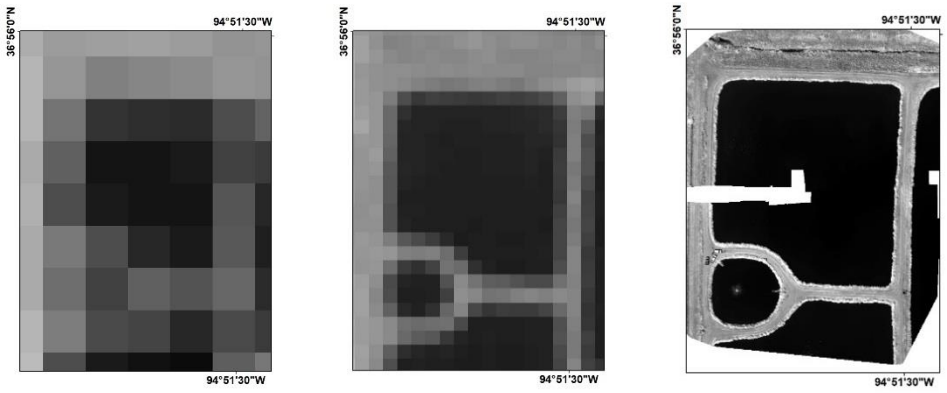

(a) **(b)** **(c)**

Figure 2.14. Remote sensing imagery collected at the high nutrient system by Landsat–8 (a), Sentinel–2A (b), and sUAS (c).

In order to determine optical and non-optical water quality measurements from multispectral sensors, in-situ measurements are needed to develop and calibrate the different models (Bonansea et al., 2015). However, due to the above limitations for use of satellite imagery, selecting images for these types of correlations can become a non-trivial task. Hicks et al. (2013) suggest that ideal imagery for these types of studies should not be more than one day apart from the in-situ data collection. However, in most cases, this is not possible due to the temporal resolution of the platform or cloud coverage present in the imagery (Kloiber et al., 2002; Olmanson et al., 2008; Zhang et al., 2012; Bonansea et al., 2015; Mushtaq and Nee Lala, 2017). Furthermore, Barrett and Frazier (2016) mention that water quality parameters can be directly influenced by rapidly changing environmental conditions in the study site, and as a result, the utility of predictive models developed from imagery that is generated days or weeks from the day of the in-situ sampling can be detrimentally impacted. As shown in Table 2.1, with the use of an sUAS, the time window between water sample acquisition and multispectral imagery collection can be reduced to minutes to hours. In theory, and due to the flexibility that these portable platforms provide, decreasing the time window between water sample acquisition and multispectral imagery collection translates to stronger and more reliable water quality models.

A secondary objective of this study was to evaluate if using a statistical interpolation method improved the algorithms between the different optical and non-optical water quality parameters and the reflectance values. In order to do that, three scenarios were evaluated under the reflectance extraction procedures: (1) Point extraction, (2) buffer extraction, and (3) Kriging extraction. Results indicated that models created from the first scenario (point extraction) presented stronger predictive capabilities. Mu et al. (2015) references that in spatial sampling, collected samples are not independent from each other and for that reason the number of samples that need to be taken

in order to develop or validate remote sensing products can be decreased in order to improve accuracy. Considering the water quality results and the spatial distribution maps generated in this study, it makes sense that for fully mixed systems (such as the ponds used in this study), fewer sample stations led to more accurate models.

For all the points discussed, one can determine that the use of sUAS offers additional benefits than the traditional satellite remote sensing approach. However, it is important to point out that sUAS, just like any other remote sensing tool, have their limitations. The first and perhaps the most important limiting factor when using this technology is the weather. When planning missions with sUAS, the operator must be aware that these platforms are unable to fly under wet conditions (rain) and elevated wind speeds (higher than 5 m/s or as stipulated by the platform manufacturer). For the study presented above, these issues were not a concern. However, it is necessary to point this out, because even though sUAS offer more advantages when it comes to obtaining imagery capable of estimating optical and non-optical water quality parameters, there is a tradeoff that needs to be considered and evaluated by the user.

2.5. Conclusions

This study aimed to create different statistical water quality models for optical (TSS, SDD, and Chl-a) and non-optical (TP and TN) water quality parameters in low and high nutrient systems using remote sensing images from an sUAS equipped with a multispectral sensor. From the results of this study, it can be concluded that: (1) When using a multiple linear regression approach, models capable of predicting optical and non-optical models (with strong prediction capability $R^2 \geq 0.80$) can be created, (2) multiple variable linear regressions in the visible portion of the electromagnetic spectrum (blue, green, and red) best described the relationship between TSS (R^2

= 0.99, *p*-value = ≤ 0.01, n=15), Chl-a (R^2 = 0.85, *p*-value = ≤ 0.01, n=15), TP (R^2 = 0.98, *p*-value = ≤ 0.01, n=15), TN (R^2 = 0.98, *p*-value = ≤ 0.01, n=15), and SDD (R^2 = 0.88, *p*-value = ≤ 0.01, n=15), (3) the use of statistical interpolation (ordinary Kriging) resulted in poor AICc values between the different water quality parameters and the reflectance values, (4) 100% cloud free imagery can be collected with the use of sUAS, (5) the use of sUAS for water quality monitoring allows the user more flexibility in terms of temporal and spatial resolution, and (6) future research should evaluate if the use of this technology improves the predictive capabilities of water quality models that rely on satellite imagery and if the models developed in this study have the capacity of determining water quality in reservoirs that fall in other portions of the biological productivity spectrum.

References

Aerial Technology International. ATI AgBOT Data Sheet. Available online: http://store.aerialtechnology.com/product/agbot-2/ (accessed on 7 December 2019).

Akaike, H. Information Theory and an Extension of the Maximum Likelihood Principle. In Proceedings of the 2nd International Symposium on Information Theory: Tsahkadsor, Armenia, 2–8 September 1971; Akadémiai Kiadó: Budapest, Hungary, 1973; pp. 267–281.

Allan, M.G.; Hamilton, D.P.; Hicks, B.J.; Brabyn, L. Landsat remote sensing of chlorophyll-a concentrations in central north island lakes of New Zealand. Int. J. Remote Sens. 2011, 32, 2037–2055.

Anderson, C.R.; Berdalet, E.; Kudela, R.M.; Cusack, C.K.; Silke, J.; O'Rourke, E.; Dugan, D.; McCammon, M.; Newton, J.A.; Moore, S.K.; et al. Scaling up from regional case studies to a global harmful algal bloom observing system. Front. Mar. Sci. 2019, 6.

ArcMap; Computer Software; Environmental Systems Research Institute (ESRI): Redlands, CA, USA, 2012.

Asner, G.P. Cloud cover in Landsat observations of the Brazilian Amazon. Int. J. Remote Sens. 2010, 22, 3855–3862.

Baban, S.J. Detecting water quality parameters in the Norfolk Broads, U.K., using Landsat imagery. Int. J. Remote Sens. 2007, 14, 1247–1267, doi:10.1080/01431169308953955.

Barrett, D.C.; Frazier, A.E. Automated method for monitoring water quality using Landsat imagery. Water 2016, 8, 257–271.

Berni, J.A.; Zarco-Tejada, P.J.; Suarez, L.; Fereres, E. Thermal and narrowband multispectral remote sensing for vegetation monitoring from an unmanned aerial vehicle. IEEE Trans. Geosci. Remote Sens. 2009, 47, 722–738.

Bonansea, M.; Rodriguez, M.C.; Pinotti, L.; Ferrero, S. Using multi-temporal Landsat imagery and linear mixed models for assessing water quality parameters in Río Tercero Reservoir (Argentina). Remote Sens. Environ. 2015, 158, 28–41.

Brezonik, P.L.; Olmanson, L.G.; Finlay, J.C.; Bauer, M.E. Factors affecting the measurement of CDOM by remote sensing of optically complex inland waters. Remote Sens. Environ. 2015, 157, 199–215.

Burnham, K.P.; Anderson, D.A. Model Selection and Multimodel Inference, 2nd ed.; Springer: New York, NY, USA, 2002; pp. 1–488.

Carlson, R.E. A trophic state index for lakes. Limnol. Oceanogr. 1977, 22, 361–369.

Colomina, I.; Molina, P. Unmanned aerial systems for photogrammetry and remote sensing: A review. ISPRS J. Photogramm. Remote Sens. 2014, 92, 79–97.

Davis, T.W.; Stumpf, R.; Bullerjahn, G.S.; McKay, R.M.; Chaffin, J.D.; Bridgeman, T.B.; Winslow, C. Science meets policy: A framework for determining impairment designation criteria for large waterbodies affected by cyanobacterial harmful algal blooms. Harmful Algae 2019, 81, 59–64.

Dominguez, J.A.; Chuvieco, E.; Sastre-Merlin, A. Monitoring transparency in inland water bodies using multispectral images. Int. J. Remote Sens. 2009, 30, 1567–1586.

Doughty, C.; Cavanaugh, K. Mapping coastal wetlands biomass from high resolution unmanned aerial vehicle (UAV) imagery. Remote Sens. 2019, 11, 540.

Duan, H.; Ma, R.; Hu, C. Evaluation of remote sensing algorithms for cyanobacterial pigment retrievals during spring bloom formation in several lakes of east China. Remote Sens. Environ. 2012, 126, 126–135.

Forget, P.; Ouillon, S.; Lahet, F.; Broche, P. Inversion of reflectance spectra of nonchlorophyllous turbid coastal waters. Remote Sens. Environ. 1999, 68, 264–272.

Gholizadeh, M.H.; Melesse, A.M.; Reddi, L. A comprehensive review on water quality parameters estimation using remote sensing techniques. Sensors 2016, 16, 1298–1320.

Giardino, C.; Pepe, M.; Brivio, P.A.; Ghezzi, P.; Zilioli, E. Detecting chlorophyll, Secchi disk depth and surface temperature in a sub-alpine lake using Landsat imagery. Sci. Total. Environ. 2001, 268, 19–29.

Guan, X.; Li, J.; Booty, W.G. Monitoring Lake Simcoe water clarity using Landsat-5 TM images. Water Resour. Manag. 2011, 25, 2015–2033.

Hicks, B.J.; Stichbury, G.A.; Brabyn, L.K.; Allan, M.G.; Ashraf, S. Hindcasting water clarity from Landsat satellite images of unmonitored shallow lakes in the Waikato Region, New Zealand. Environ. Monit. Assess. 2013, 185, 7245–7261.

International Ocean-Colour Coordinating Group (Ioccg). Earth Observations in Support of Global Water Quality Monitoring; International Ocean Colour Coordinating Group (IOCCG): Dartmouth, NS, Canada, 2018; p. 132.

International Ocean-Colour Coordinating Group (IOCCG). Why the Ocean Color? The Societal Benefits of Ocean-Colour Technology; International Ocean Colour Coordinating Group (IOCCG): Dartmouth, NS, Canada, 2008; p. 141.

Kageyama, Y.; Takahashi, J.; Nishida, M.; Kobori, B.; Nagamoto, D. Analysis of water quality in Miharu dam reservoir, Japan, using UAV data. IEEJ Trans. Electr. Electron. Eng. Jpn. 2016, 11, 183–185.

Kirk, J.T.O. Optical water quality—What does it mean and how should we measure it? J. Water Pollut. Control Fed. 1988, 60, 194–197.

Kloiber, S.M.; Brezonik, P.L.; Olmanson, L.G.; Bauer, M.V. A procedure for regional lake water clarity assessment using Landsat multispectral data. Remote Sens. Environ. 2002, 82, 38–47.

Lee, Z.; Hu, C. Global distribution of Case-1 waters: An analysis from Seawifs measurements. Remote Sens. Environ. 2006, 101, 270–276.

Lillesand, T.M.; Johnson, W.L.; Deuell, R.L.; Lindstrom, O.M.; Meisner, D.E. Use of Landsat data to predict the trophic state of Minnesota lakes. Photogramm. Eng. Remote Sens. 1983, 49, 219–229.

Lim, J.; Choi, M. Assessment of water quality based on Landsat 8 operational land imager associated with human activities in Korea. Environ. Monit. Assess. 2015, 187, 384–401.

Liu, J.; Zhang, Y.; Yuan, D.; Song, X. Empirical estimation of total nitrogen and total phosphorus concentration of urban water bodies in China using high resolution IKONOS multispectral imagery. Water 2015, 7, 6551–6573.

Liu, X.; Chen, Y.; Chen, Y.; He, R. Optimization of earth observation satellite system based on parallel systems and computational experiments. J. Control Theory Appl. 2013, 11, 200–206.

Louhaichi, M.; Petersen, S.; Gomez, T.; Jensen, R.R.; Morgan, G.R.; Butterfield, C. Remote spectral imaging using a low cost sUAV system for monitoring rangelands. Adv. Remote Sens. Geo Inform. Appl. 2018, 1, 143–145.

Ma, J.; Qin, B.; Wu, P.; Zhou, J.; Niu, C.; Deng, J.; Niu, H. Controlling cyanobacteria blooms by managing nutrient ratio and limitation in large hyper-eutrophic lake: Lake Taihu, China. J. Environ. Sci. 2015, 27, 80–86.

Matthews, M.W.; Bernard, S.; Robertson, L. An algorithm for detecting trophic status (chlorophyll-a), cyanobacterial-dominance, surface scums and floating vegetation in inland and coastal waters. Remote Sens. Environ. 2012, 124, 637–652.

Melville, B.; Fisher, A.; Lucieer, A. Ultra-high spatial resolution fractional vegetation cover from unmanned aerial multispectral imagery. Int. J. Appl. Earth Obs. Geoinf. 2019, 78, 14–24.

Mesonet. Local Conditions. Available online: https://www.mesonet.org/index.php/weather/local (accessed on 10 December 2019).

Mission Planner; Computer Software; ArduPilot Development Team. Retrieved from https://ardupilot.org/planner/ (accessed on 23 December 2019).

Mobley, C.; Stramski, D.; Bissett, W.; Boss, E. Optical modeling of ocean waters: Is the Case 1–Case 2 classification still useful? Oceanography 2004, 17, 60–67.

Morel, A.; Belanger, S. Improved detection of turbid waters from ocean color sensors information. Remote Sens. Environ. 2006, 102, 237–249.

Mu, X.; Hu, M.; Song, W.; Ruan, G.; Ge, Y.; Wang, J.; Huang, S.; Yan, G. Evaluation of sampling methods for validation of remotely sensed fractional vegetation cover. Remote Sens. 2015, 7, 16164–16182.

Mushtaq, F.; Nee Lala, M.G. Remote estimation of water quality parameters of Himalayan lake (Kashmir) using Landsat 8 OLI imagery. Geocarto Int. 2017, 32, 274–285.

Nebiker, S.; Lack, N.; Abacherli, M. Light-weight multispectral UAV sensors and their capabilities for predicting grain yield and detecting plant diseases. Int. Arch. Photogramm. Remote Sens. Spat. Inf. Sci. 2016, XLI-B1, 963–970.

Nelson, S.; Soranno, P.A.; Spence Cheruvelil, K.; Batzli, S.; Skole, D.L. Regional assessment of lake water clarity using satellite remote sensing. Educ. J. Limnol. 2003, 32, 27–32.

Oklahoma Department of Environmental Quality. Lagoon Sewage Treatment Systems. Available online: https://www.deq.ok.gov/wp-content/uploads/environmental-complaints/Lagoon-.pdf (accessed on 10 December 2019).

Olmanson, L.G.; Bauer, M.E.; Brezonik, P.L. A 20-year Landsat water clarity census of Minnesota's 10,000 lakes. Remote Sens. Environ. 2008, 112, 4086–4097.

Pix4Dmapper; Computer Software; Pix4D SA: Prilly, Switzerland, 2011.

R Core Team. R; Computer Software; R Core Team: Vienna, Austria, 2017.

Ritchie, J.C.; Zimba, P.V.; Everitt, J.H. Remote sensing techniques to assess water quality. Am. Soc. Photogramm. Remote Sens. 2003, 6, 695–704.

Rusnak, M.; Sladek, J.; Kidova, A.; Lehotsky, M. Template for high-resolution river landscape mapping using UAV technology. Measurement 2018, 115, 139–151.

Schmale, D.G.; Ault, A.P.; Saad, W.; Scott, D.T.; Westrick, J.A. Perspectives on harmful algal blooms (HABs) and the cyberbiosecurity of freshwater systems. Front. Bioeng. Biotechnol. 2019, 7.

Shapiro, S.S.; Wilk, M.B. An analysis of variance test for normality (complete samples). Biometrika 1965, 52, 591–611.

Sharaf El Din, E.; Zhang, Y. Estimation of both optical and non-optical surface water quality parameters using Landsat 8 OLI imagery and statistical techniques. J. Appl. Remote Sens. 2017, 11, 046008.

Song, K.; Li, L.; Li, S.; Tedesco, L.; Hall, B.; Li, L. Hyperspectral remote sensing of total phosphorus (TP) in three central Indiana water supply reservoirs. Water Air Soil Pollut. 2012, 223, 1481–1502.

Su, T.; Chou, H. Application of multispectral sensors carried on unmanned aerial vehicle (UAV) to trophic state mapping of small reservoirs: A case study of Tain-Pu Reservoir in Kinmen, Taiwan. Remote Sens. 2015, 7.

Torbick, N.; Hu, F.; Zhang, J.; Qi, J.; Zhang, H.; Becker, B. Mapping chlorophyll-a concentrations in west lake, China using Landsat 7 ETM+. J. Great Lakes Res. 2008, 34, 559–565.

United States Environmental Protection Agency. Methods for Chemical Analysis of Waters and Waste Waters; EPA/600/4-79/020 (NTIS PB84128677); U.S. Environmental Protection Agency: Washington, DC, USA, 2002,

United States Geological Survey. Measuring and Monitoring Water. Available online: https://www.usgs.gov/mission-areas/water-resources/science/measuring-and-monitoring-water (accessed on 10 December 2019).

Wilde, F.D. Field Measurements: U.S. Geological Survey Techniques of Water-Resources Investigations. Available online: http://pubs.water.usgs.gov/twri9A6/ (accessed on 10 December 2019).

Wu, C.; Wu, J.; Qi, J.; Zhang, L.; Huang, H.; Lou, L.; Chen, Y. Empirical estimation of total phosphorus concentration in the mainstream of the Qiantang River in China using Landsat TM data. Int. J. Remote Sens. 2010, 31, 2309–2324.YSI Incorporated. 6-Serie Multiparameter Water Quality Sondes User Manual. Available online: https://www.ysi.com/File%20Library/Documents/Manuals/069300-YSI-6-Series-Manual-RevJ.pdf (accessed December 7 on 2019).

Zhang, C.; Kovacs, J.M. The application of small unmanned aerial systems for precision agriculture: A review. Precis. Agric. 2012, 12, 693–712.

Zhao, D.; Cai, Y.; Jiang, H.; Xu, D.; Zhang, W.; An, S. Estimation of water clarity in Taihu lake and surrounding rivers using Landsat imagery. Adv. Water Resour. 2011, 34, 165–173.

CHAPTER 3 – Is Bigger Always Better? Analysis of Models Developed from Small Unoccupied Aerial System Imagery Compared to Satellite Remote Sensing of Optical and Non-optical Water Quality Parameters

This chapter is formatted for submission to *Drones*.

Abstract: Continuous global expansion of agricultural, industrial, and commercial practices has resulted in ubiquitous discharges of elevated concentrations of phosphorous and nitrogen into surface waters. Due to nutrient over-enrichment and resulting water quality degradation, effective monitoring of water bodies has become a necessity yet a major challenge. Modern remote sensing tools (multispectral sensors onboard satellites) can accurately and reliably estimate water quality information and expand the discrete sampling point coverage associated with traditional labor-intensive in-situ sampling but are subject to certain environmental limitations. However, the recent emergence of compact multispectral sensors and small Unoccupied Aerial Systems (sUAS) has opened the possibility of collecting high-resolution multispectral imagery without some of the constraints of satellite data collection. The purpose of this study was to compare multispectral imagery from two satellite-based remote sensing tools (Landsat 8 and Sentinel-2) and a sUAS. Optical and non-optical water quality parameters were able to be predicted in both low nutrient and high nutrient bodies of water by multiple linear regression. Algorithms for optical water quality parameters were developed with imagery collected with all platforms. However, for the non-optical data, reliable models were obtained only from the imagery collected with the sUAS.

Keywords: Remote Sensing, Small Unoccupied Aerial System, Landsat 8, Sentinel-2, Water Quality

3.1. Introduction

Global agricultural, industrial, and commercial practices are constantly changing to adjust to continuously growing demand triggered by different socioeconomic, political, and environmental factors (e.g., increases in population, rapid urbanization, water availability and supply, and climate variation) (Reilly et al., 1994; Burns, 2000; Hails, 2002; Barnwal and Kotani, 2013; Hertel and Lobell, 2014). As a direct result of some of these global changes, elevated concentrations of phosphorous (P) and nitrogen (N) are discharged into surface waters (rivers, lakes, and streams) via point and non-point sources (Han et al., 2012; LaBeau et al., 2013; Bosh et al., 2014; Bosch et al., 2015; Culbertson et al., 2016). This nutrient over-enrichment has proven to not only degrade water quality (Leon et al., 2001; Howarth et al., 2002; Keiser and Shapiro, 2019) but also to negatively impact ecosystem integrity and human health (Zhao et al., 2015; Liyanage et al., 2017; Zhao et al., 2017; Rui et al., 2018). For that reason, effective monitoring of these bodies of water is a necessity and a major challenge.

Conventionally, the collection and analysis of in-situ water samples have been the most common practices implemented for monitoring chemical, physical and biological constituents in lakes, rivers, streams, and oceans (Scott and Frost, 2017; Schraga and Cloern, 2017). However, due to discrete temporal and spatial coverage, susceptibility to errors, and labor-intensive protocols (e.g., sample collection and analyses), monitoring programs that rely only on these types of measurements may fail to identify existing or emerging water quality issues (Kloiber et al., 2002; Arabi et al., 2017; Strokal et al., 2019).

In recent decades, the use of remote sensing tools for estimation of Secchi disk depth (SDD) (Matthews, 2011; Butt and Nazeer, 2011; McCullough et al., 2013; Doña et al., 2015), total

suspended solids (TSS) (Matthews, 2011; Chen et al., 2015; Wang et al., 2018), chlorophyll-a (Chl-a) (Cannizzaro and Carder, 2006; Matthews, 2011; Hu et al., 2012; Doña et al., 2015; Laili et al., 2015; Regina et al., 2017), and colored dissolved organic matter (CDOM) (Kutser et al., 2005; Mannino et al., 2008; Matthews, 2011; Brezonik et al., 2015) in inland and near-coastal bodies of waters has proven not only to be accurate and reliable, but also has given the possibility to expand the discrete sampling point coverage associated with in-situ sampling (Gould et al., 1999; ; Kloiber et al., 2002; ; Darecki et al., 2003; Park et al., 2005; Kutser et al., 2005; Mannino et al., 2008; Matthews, 2011; Butt and Nazeer, 2011; Hu et al., 2012; Matsushita et al., 2012; McCullough et al., 2013; Brezonik et al., 2015; Doña et al., 2015; Chen et al., 2015; Laili et al., 2015; Regina et al., 2017; Cannizzaro and Carder et al., 2017; Wang et al., 2018). For most applications, the remote sensing tools are satellite platforms that carry different on-board sensors capable of measuring the reflected radiation from the Earth's surface in different portions of the electromagnetic spectrum (Kloiber et al., 2002; Matsushita et al., 2012). These measurements are then used to develop algorithms capable of determining (directly or indirectly) water quality parameters. The vast majority of these relationships have been found between the visible (red, blue, green (RGB)) and near-infrared (NIR) portions of the spectrum (Kloiber et al., 2002; Chen et al., 2015; Strokal et al., 2019). Table 3.1 presents some of the most used operational satellite missions for water quality monitoring and prediction.

Different authors have demonstrated the potential of remote sensing when it comes to monitoring and predicting water quality in both inland and oceanic waters around the world (Gholizadeh et al., 2016). Boland (1976) identified the potential of the first Earth Observation (EO) mission (Landsat 1) to estimate SDD and Chl-a in large reservoirs across the United States. As part of these findings, Boland (1976) pointed out that to estimate SDD and Chl-a, regression models needed to

incorporate specific bands or ratios of the measurements captured by the multispectral scanner (MSS) onboard Landsat. Years later, Lathrop et al. (1990) used Landsat 1 and SPOT-1 to investigate the fate and transport of a sediment plume in Lake Michigan. Lathrop et al. (1990) pointed out that, with the smaller spatial resolution of SPOT-1, certain interactions in the water are more clearly derived. Since then, and as stated by Gholizabeh et al. (2016), remote sensing techniques have allowed several researchers to monitor, predict and develop spatial and temporal views of water quality in different water bodies, due to the reliable correlations that have been found among portions of the spectrum (visible and NIR) and varied biological, chemical, and physical components in surface waters.

Table 3.1. Regularly used satellite-based remote sensing tools for water quality monitoring. Spectral resolution refers to the number of bands of the spectrum.

Mission	**Landsat-7**	**Landsat-8**	**Sentinel-2A**	**MODIS**
Spatial Resolution	15 m (band 8) 30 m (bands 1-5, 7) 60 m (band 6)	15 m (band 8) 30 m (bands 1-7,9) 100 m (bans 10-11)	10 m (bands 2-4, 8) 20 m (bands 5-7, 11,12) 60 m (bands 1,9,10)	250 m (bands 1-2) 500 m (bands 3-7) 1000 m (bands 8 – 36)
Temporal Resolution	16 days	16 days	10 days*	1-2 days
Spectral Resolution	8	11	12	36
Radiometric Resolution	12-bit	12-bit	11-bit	12-bit

*5 days with two satellites

The use of satellite-based sensors has provided effective monitoring of water quality in water bodies of various sizes, trophic states, and locations around the world, but a major drawback when using this technology is data loss due to cloud coverage (Berbar and Gaber, 2004; Sano et al., 2007; Avitabile et al., 2012; Asner et al., 2012; Strokal et al., 2019; Becker et al., 2019). Clouds

obstruct visible and near-infrared (VNIR) and thermal infrared (TIR) wavelengths, so information directly underneath clouds cannot be retrieved, resulting in alterations of surface reflectivity (Berbar et al., 2004; Becker et al., 2019). In several cases (especially when performing time-series analyses), data loss due to cloud coverage has inhibited the effective use of up to 70% of the collected data (Olmanson 2008; Asner et al., 2010; Peng et al., 2015; Xiao et al., 2018).

In recent years, the emergence of compact multispectral sensors and small Unoccupied Aerial Systems (sUAS) has opened possibilities of collecting higher resolution multispectral imagery with study specific revisiting periods and minimal impact from atmospheric effects (e.g., cloud cover) at substantially lower costs (Tang and Shao, 2015; Zeng et al., 2017; Agudo et al., 2018; Thorp et al., 2018; de Oca et al., 2018; Gomes et al., 2018; Mogili and Deepak, 2018; Stavrakoudis et al., 2019). Notably, the use of these new technologies in water quality monitoring has proven useful to predict and monitor optical water quality parameters (e.g., Chl-a, SDD, TSS, and turbidity); but also, non-optical water quality parameters (e.g., total nitrogen (TN) and total phosphorus (TP)) (Arango and Nairn, 2020), due to the higher spatial resolution of the captured data.

The use of sUAS is becoming an attractive tool to monitor and predict water quality (Arango and Nairn, 2020). For that reason, the purpose of this study was to compare multispectral imagery from two satellite-based remote sensing tools (Landsat 8 and Sentinel-2) and that from an sUAS to determine if traditional remote sensing technologies present advantages over the novel use of compact multispectral sensors on-board sUAS when developing monitoring algorithms for water quality.

3.2. Materials and Methods

3.2.1. Study Area

Two small human-made aquatic ecosystems were selected for this study, each serving as end members of the range of aquatic biological productivity. Both systems are located in the northeast portion of the state of Oklahoma (Figure 3.1). The high nutrient system (Figure 3.1a) is a series of human-made lagoons located in the City of Commerce, Oklahoma (36.5691° N, −94.9676° W). This system is composed of four hydrologically connected process units (one clarifier, two treatment units, and one final polishing unit, ranging in surface area from 0.2 to 2.2 ha) that serve as primary treatment for the city's domestic wastewater before it is discharged. Due to the nature of domestic wastewaters, this high nutrient system contains elevated concentrations of phosphorus (P), nitrogen (N) and carbon (C) (EPA, 2012).

The low nutrient system (Figure 3.1b) consists of a series of human-made ponds located on the upstream part of the Duck Creek arm of Grand Lake O' the Cherokees (Grand Lake) (36.5691° N, −94.9676° W). This system is composed of seven ponds (ranging in surface area from 0.5 to 2.5 ha) that collectively served as an aquatic plant nursery, managed by the Grand River Dam Authority (GRDA). Despite their proximity to Grand Lake, these ponds are not hydrologically connected to the larger reservoir, and their primary hydrologic input is surface runoff. However, when water levels in Grand Lake are elevated, these ponds serve as flood control units. Table 3.2 presents the coordinates of each sampling station in both systems.

Due to the relative proximity of these two systems (< 40 km from each other), weather patterns and land use conditions are not dissimilar. In terms of weather, the annual mean temperatures in the area

is 15°C for Ottawa County, where the high nutrient system is located, and 15.5°C for Delaware County, where the low nutrient system is located. Annual mean precipitation for Ottawa County is 114 cm and for Delaware County is 118 cm (Mesonet, 2020). As for land use/land cover, the low nutrient system is surrounded mainly by pasture/hay, while the high nutrient system is surrounded by some urban development and pasture/hay (USGS, 2016).

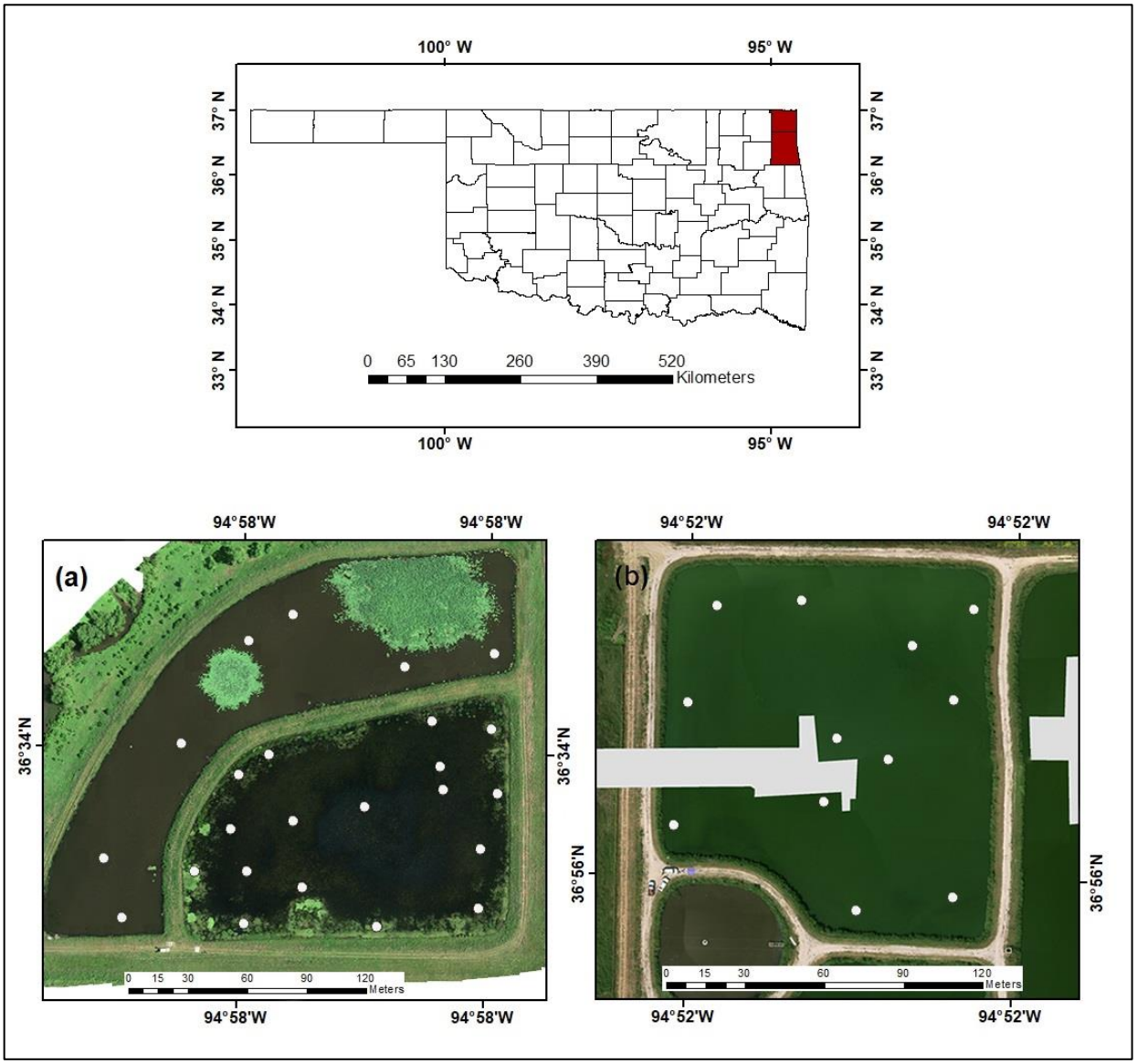

Figure 3.1. Location of (a) Low nutrient System – Nursery Ponds, Delaware County, Oklahoma, and (b) High nutrient system – Wastewater Lagoons, Ottawa County, Oklahoma, and their in-situ sampling locations (white). RGB composite from imagery captured by the sUAS

Table 3.2. Latitude (Lat) and longitude (Long) coordinates of the sampled stations at the low nutrient (LN) and high nutrient (HN) system.

	Nursery Ponds					Wastewater Lagoons		
Site ID	Lat	Long	Site ID	Lat	Long	Site ID	Lat	Long
LN-1	36.56874	-94.9667	LN-13	36.56919	-94.9674	HN-1	36.93211	-94.8597
LN-2	36.56901	-94.9667	LN-14	36.56907	-94.9681	HN-2	36.93253	-94.8597
LN-3	36.56926	-94.9666	LN-15	36.56889	-94.968	HN-3	36.93286	-94.8596
LN-4	36.56955	-94.9666	LN-16	36.56863	-94.968	HN-4	36.93288	-94.8592
LN-5	36.56959	-94.9670	LN-17	36.56887	-94.9683	HN-5	36.93237	-94.8591
LN-6	36.56938	-94.9669	LN-18	36.56865	-94.9687	HN-6	36.93220	-94.8591
LN-7	36.56928	-94.9669	LN-19	36.56893	-94.9688	HN-7	36.93274	-94.8587
LN-8	36.56865	-94.9673	LN-20	36.56946	-94.9684	HN-8	36.93235	-94.8588
LN-9	36.56881	-94.9677	LN-21	36.56989	-94.9681	HN-9	36.93183	-94.8589
LN-10	36.56912	-94.9678	LN-22	36.57006	-94.9678	HN-10	36.93188	-94.8585
LN-11	36.56943	-94.9679	LN-23	36.56981	-94.9671	HN-11	36.93256	-94.8585
LN-12	36.56933	-94.9681	LN-24	36.56988	-94.9666	HN-12	36.93287	-94.8585

3.2.2. In-situ Water Quality

Twenty-four and twelve sampling sites were established at the low nutrient and high nutrient systems, respectively. Figure 3.2 presents the sampling procedure at each location. All samples were collected and preserved according to procedures from the U.S. Environmental Protection Agency (EPA, Washington, DC, USA) (EPA, 2002). Samples were collected on July 12, 2017, and September 8, 2017, for the low nutrient and high nutrient systems, respectively.

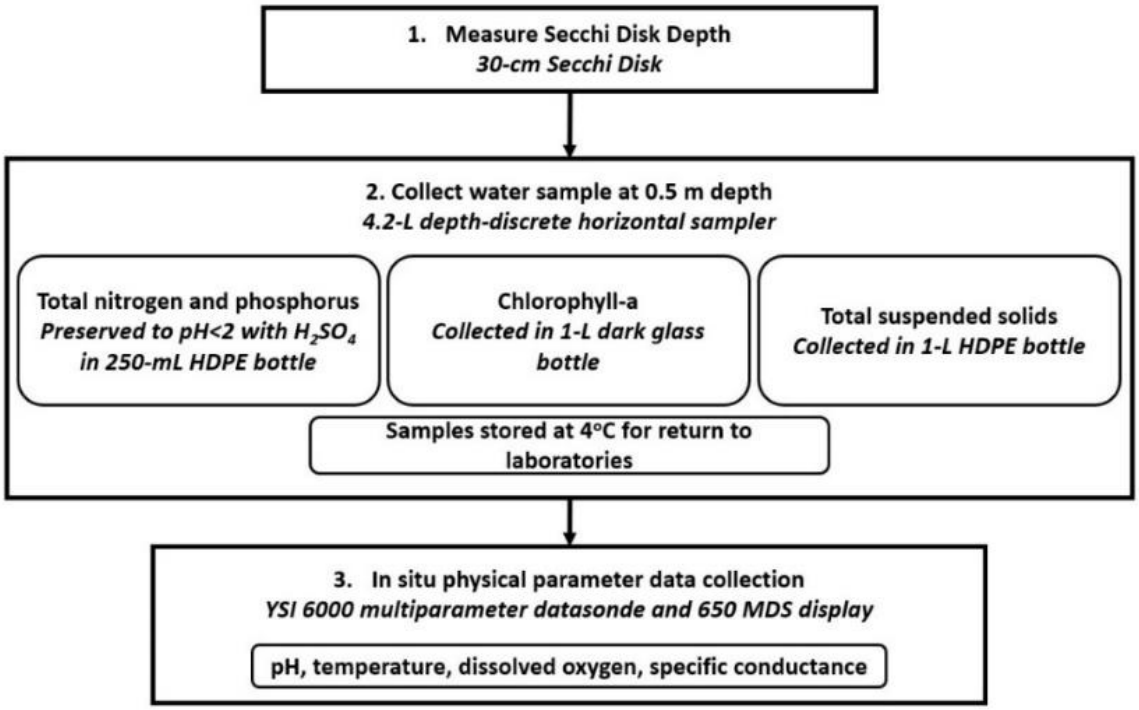

Figure 3.2. Followed field procedure to collect water samples at each station in the low nutrient and high nutrient systems.

3.2.3. Multispectral Imagery Collection

Multispectral imagery for this study was collected by three remote sensing tools: (1) Landsat 8, (2) Sentinel-2, and (3) a compact multispectral sensor on-board an sUAS.

3.2.3.1. Landsat 8

Landsat 8 is the latest mission launched by the National Aeronautics and Space Administration (NASA) under EO program on February 11, 2013. It orbits the Earth in a sun-synchronous, near-polar orbit at an altitude of 705 km. The spatial resolution of Landsat 8 depends on the specific band in question. VNIR and short-wave infrared (SWIR) are produced at resolutions of 30 m, while the panchromatic (Pan) band is produced of 15 m, temporal resolution of 16 days and spectral resolution of nine spectral and two thermal bands. On-board, Landsat 8 includes a push

broom Operational Land Imager (OLI) sensor and a Thermal Infrared Sensor (TIRS). The OLI sensor is capable of capturing information in the coastal blue, blue, green, red, NIR, SWIR 1, SWIR 2, panchromatic and cirrus bands (USGS, 2020). For this project, atmospherically corrected surface reflectance level 2 data (path 26, row 35) were obtained from the United States Geological Survey (USGS) EarthExplorer (USGS, 2020) server.

3.2.3.2. Sentinel-2

Sentinel-2 is the second mission launched by the European Space Agency (ESA) under their next-generation EO program. This mission consists of two identical satellites (Sentinel-2A and Sentinel-2B). Sentinel-2A was launched on June 23, 2015, while Sentinel-2B was launched on March 7, 2017. Both satellites orbit the earth in a sun-synchronous polar orbit at an altitude of 786 km. Sentinel-2 imagery has spatial resolutions of 10 m (bands 2-4, 8), 20 m (bands 5-7, 11, 12) and 60 m (bands 1, 9, 10), temporal resolution of five days (with two satellites) and spectral resolution of 12 bands. On-board, Sentinel-2 includes a push-broom Multispectral Instrument (MSI) capable of capturing information in the ultra-blue, blue, green, red, red edge-1, red edge-2, red edge-3, NIR, narrow NIR, water vapor, cirrus, SWIR-1, and SWIR-2 bands (ESA, 2020). For this project, Level-1C top-of-atmosphere (TOA) data were obtained from the USGS EarthExplorer (USGS, 2020) server. Atmospheric correction was performed in SNAP 7.0 (ESA, 2020) using the Sen2Cor 2.8 tool (ESA, 2020) to obtain Level 2A images.

3.2.3.3. Small Unoccupied Aerial System

An Aerial Technology International (ATI) AgBOT (Figure 3.3) was the drone platform used to collect multispectral imagery. This sUAS is a vertical takeoff and landing (VTOL) quadcopter (38

cm tri-prop and 4012 400Kv motors), made of carbon fiber (frame), and aluminum (fittings). The ATI AgBOT weighs 4.7 kg (including sensor and batteries). On-board, the AgBOT is equipped with two 6S 6500 mAh lithium polymer (LiPo) batteries (that allow for 26+ minutes of flight time), UBlox Global Positioning System (GPS), compass module, and a MicaSense RedEdge multispectral sensor. The MicaSense RedEdge sensor has a radiometric resolution of 16-bit and spectral resolution of five bands, capable of collecting information in the blue, green, red, red edge and NIR portion of the electromagnetic spectrum. This sensor has a ground sample difference of 5.4 cm/pixel (at 60 m above ground level (AGL)), a horizontal field of view (HFOV) of 47.2°, and a capture speed of 1 second/band (ATI, 2020).

Figure 3.3. ATI AgBOT quadcopter in operation.

Multispectral data for this study were collected on July 12, 2017, beginning at 11:00 AM CDT and September 8, 2017, beginning at 2:00 PM CDT for the low nutrient and high nutrient systems,

respectively. Two multiple-waypoint autonomous missions were designed in Mission Planner 1.3.68 (Mission Planner, 2020). Both missions were flown at an altitude of approximately 100 m AGL and a flying speed of 5 m/s. At the low nutrient systems, a total of 164 images were collected (estimated flight time of 10 min), while at the high nutrient systems, a total of 46 images were obtained (estimated flight time of 6.5 min). The ground resolution for the images captured in both missions was 6.20 cm. All the images were georeferenced with the information collected by the onboard GPS via the UBX binary protocol. Given that missions were flown above bodies of water, no ground control points (GCPs) were defined. However, monitoring and real-time position, orientation, and velocity data were obtained via the inertial navigation system (INS) on the aircraft. Light changes during the missions were accounted for by taking photographs of the MicaSense calibration reflectance panel at the beginning and end of each mission.

3.2.4. Model Development and Validation

3.2.4.1. Multispectral Data Selection

Two criteria were considered to select multispectral data from Landsat 8 and Sentinel-2 for the dates of in situ sampling and sUAS imagery collection: (1) Cloud coverage less than 10% in the scene over the study areas and (2) imagery overpass taken as close as possible to the day of the in-situ sampling. Table 3.3 presents the selected images for each mission and their respective selection criteria.

Table 3.3. Landsat 8 and Sentinel-2 selected images. LN and HN correspond to low nutrient and high nutrient systems, respectively. Water quality sampling and sUAS data collection occurred on July 12 (LN) and September 8 (HN), respectively.

Mission	Acquisition Date		Day Difference		Cloud Coverage (%)	
	LN	HN	LN	HN	LN	HN
Landsat 8	7/18/2017	9/20/2017	+6	+12	5.54	7.84
Sentinel-2	7/6/2017	9/4/2017	-6	+4	0	6.96

3.2.4.2. In-Situ Water Quality Processing and Reflectance Data Extraction

Laboratory analyses were conducted following EPA and standard methods (SM) (Baird et al., 2017) for the examination of water and wastewater. TSS concentrations were determined using EPA method 160.2. For TSS, a well-mixed volume of each sample was filtered through individual glass fiber filters and dried to constant weight at 103-105°C. TN and TP concentrations were determined using SM 4500-PJ. For TP, each sample was mixed with 0.1M ascorbic acid ($C_6H_8O_6$), 5N sulfuric acid (H_2SO_4), ammonium molybdate ($(NH_4)_2MoO_4$) and antimony potassium tartrate ($C_8H_{10}K_2O_{15}Sb_2$). For TN, each sample was mixed with nicotinic acid p-toluenesulfonate ($C_{13}H_{13}NO_5S$), 3N sodium hydroxide (NaOH), adenosine triphosphate ($C_{10}H_{16}N_5O_{13}P_3$) and potassium persulfate ($K_2S_2O_8$). Once the individual mixtures were completed, TN and TP concentrations were measured using a Lachat Quikchem 8500 series 2 flow injection analysis system and a Cole Parmer 2800 UV VIS spectrophotometer, respectively. Finally, chlorophyll-a (Chl-a) was determined following EPA method 445.0. For Chl-a, each sample was filtered through individual glass fiber filters with a nominal porosity of 0.7 μm, and then chlorophyll extractions were performed using 90% acetone as the extraction solvent. Once these extractions were completed, Chl-a concentrations were measured with a Trilogy laboratory fluorometer at a wavelength of 460 nm.

Reflectance extraction for all the multispectral imagery was performed in ArcMap 10.6 (ArcMap, 2012). For this purpose, the georeferenced location of each sampling station was used to perform a value to point extraction (Table 8).

3.2.4.3. Water Quality Algorithms – Development and Validation

Three independent datasets were generated in the previous steps, RGB reflectance and in-situ water quality for: (1) Landsat 8, (2) Sentinel-2 and (3) sUAS. To develop and validate optical and non-optical water quality models, these datasets were treated independently. The models were trained and validated, employing the k-fold cross validation methodology (Refaeilzadeh et al., 2009). Each independent dataset (e.g., Landsat 8, Sentinel-2 and sUAS) were randomly split into 10 folds. Each model was run 10 times, each time withholding one division (each division was later used for validation). K-fold cross validation analyses were completed using the caret package in R 3.5.1 (R Core Team, 2017). As a result, algorithms for the use of these three remote sensing tools were developed.

Regressions models were developed using multiple variable linear approaches, where the reflectance data were selected as the independent variables, and the measured water quality parameters were determined as the response/dependent variable. The best fit for the models was determined using two criteria: (1) the coefficient of determination (R^2) and (2) the sample corrected Akaike information criterion (AICc) (Akaike, 1971).

3.3. Results

3.3.1. Water Quality

Table 3.4 summarizes the measured physical and chemical water quality parameters in the low and high nutrient systems. Comparing the water quality of these two systems, it can be observed that indeed they are on opposite sides of the biological productivity spectrum. This difference is especially noticeable when looking at the specific conductance, nutrient (TP and TN) and chlorophyll concentrations that each system had at the time of sampling.

Table 3.4. Physical and chemical measured water quality parameters in the low nutrient (July 12, 2017) and high nutrient (September 8, 2017) system (n=35). TSS, SDD, Chl-a, TN, TP, Temp, DO and Sp Cond refer to total suspended solids, Secchi disk depth, chlorophyll-a, total nitrogen, total phosphorus, temperature, dissolved oxygen, and specific conductance, respectively.

	Statistics	TSS (mg/L)	SDD (cm)	Chl-a (µg/L)	TN (mg/L)	TP (mg/L)	Temp (°C)	pH	DO (%)	Sp Cond (µS/cm)
Low	Min	0.11	40.00	4.26	0.30	0.01	29.1	7.89	74.2	0.08
Nutrient	Max	7.00	70.00	15.37	1.71	0.20	32.88	10.02	140.4	0.18
System	Mean	2.44	60.40	8.52	0.68	0.04	31.45	9.15	114.9	0.12
	Median	2.57	62.00	8.10	0.56	0.02	31.39	9.41	114.4	0.09
High	Min	60.20	15.00	200.40	12.00	2.94	22.97	8.08	60.9	0.79
Nutrient	Max	68.83	18.00	575.80	13.60	4.02	26.08	8.75	216.1	0.84
System	Mean	65.33	16.18	358.30	12.47	3.33	24.28	8.58	122.0	0.82
	Median	65.20	16.00	352.60	12.40	3.27	24.02	8.60	112.6	0.83

3.3.2. Spectral Responses – Landsat 8, Sentinel-2 and sUAS

A comparison of the spectral profiles of the visible portion of the spectrum is presented for each of the remote sensing tools (Landsat 8, Sentinel-2, and the sUAS) as a function of the stations sampled in the low nutrient (Figure 3.4a) and high nutrient (Figure 3.4b) systems. Comparing the visible bands of the different sensors in each system shows that, due to the distinct compositions

and characteristics of each system, the spectral profile in the low and high nutrient system exhibit different patterns.

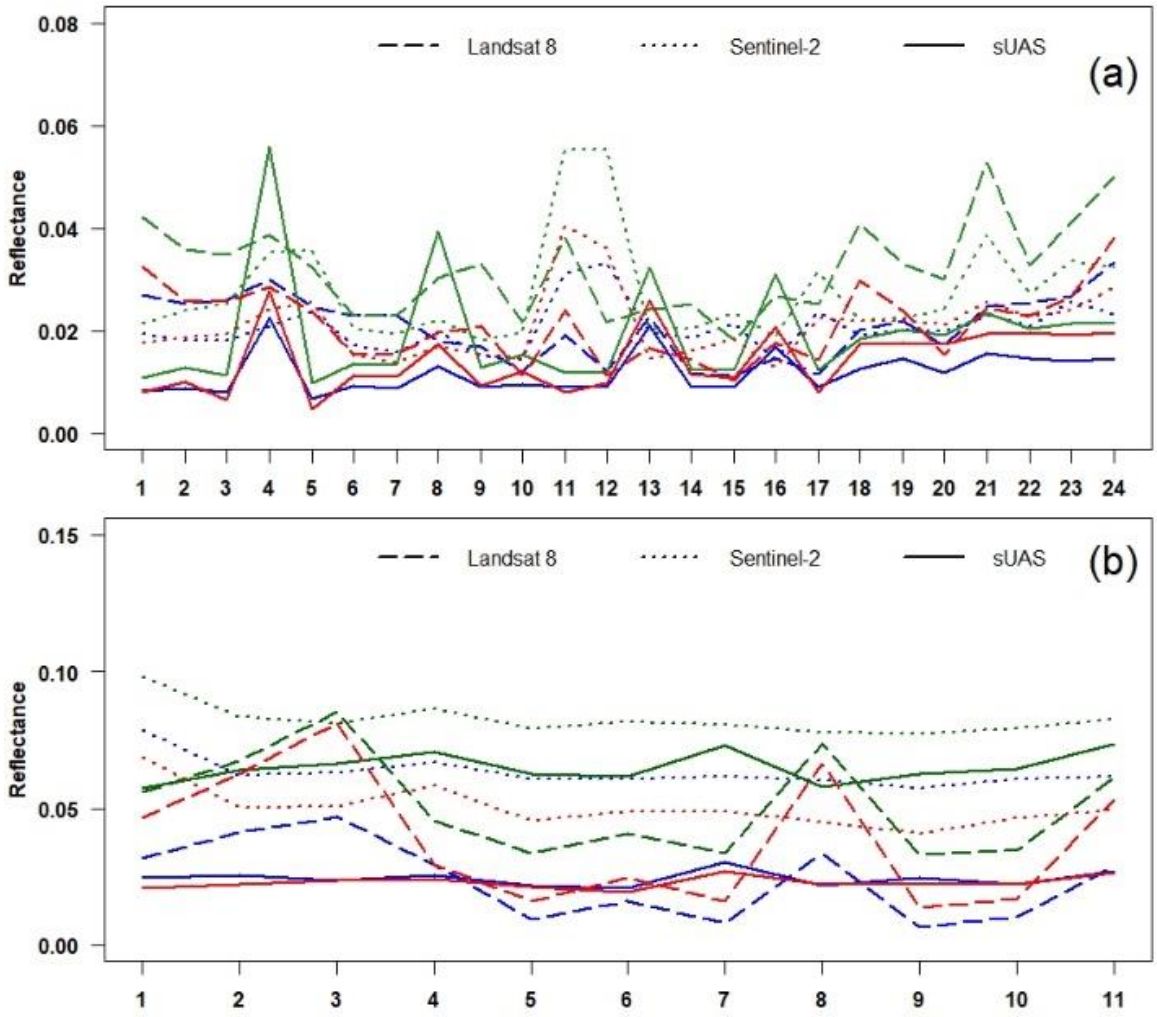

Figure 3.4. Reflectance (y-axis) profile in the blue, green, and red band of the low nutrient (a) and high nutrient (b) system as a function of the number of sampled stations (x-axis). Dashed, dotted, and solid refer Landsat 8, Sentinel-2 and sUAS, respectively.

Additionally, when examining overall reflectance captured by each sensor in the different visible bands, the information captured by the sUAS in each band is statistically different (by means of a Wilcoxon signed-ranked test where all p-values were ≤ 0.05) (Figure 3.5).

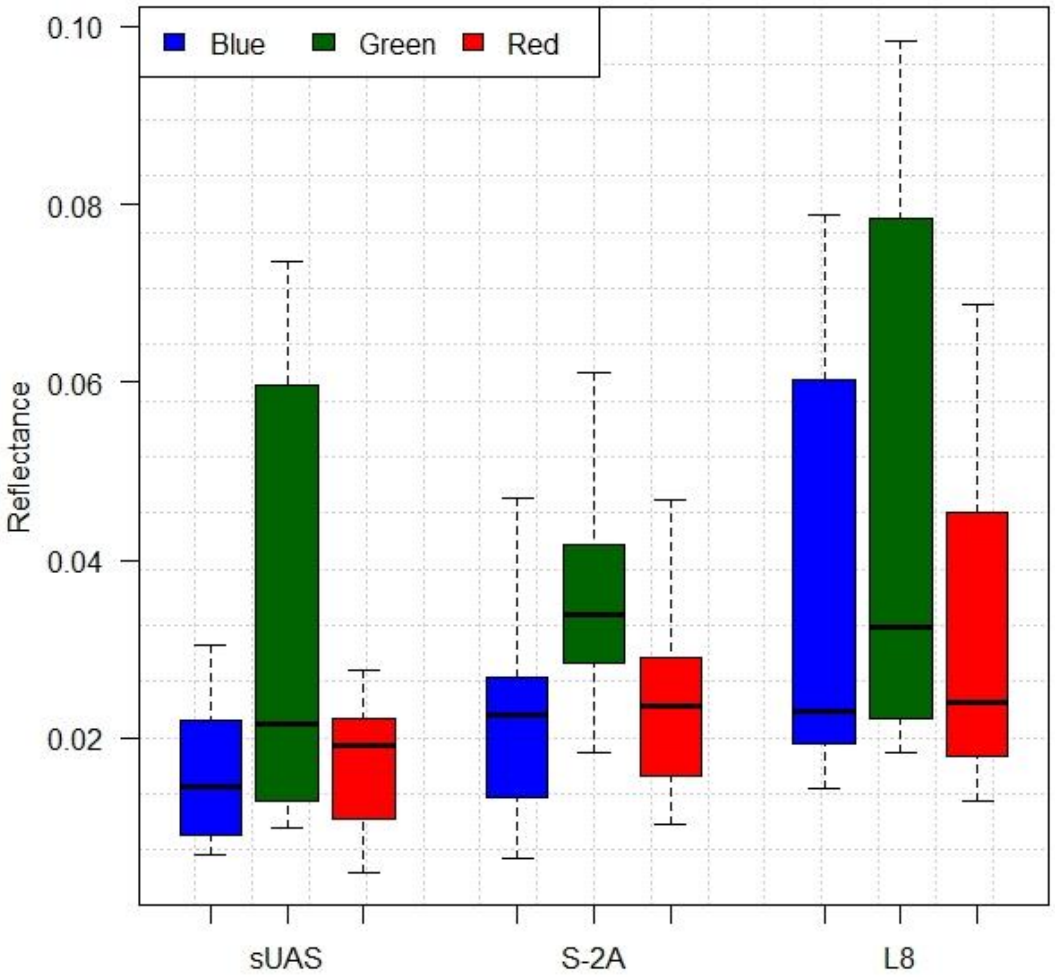

Figure 3.5. Comparison of blue, green, and red reflectance (y-axis) for each remote sensing tool (x-axis). S-2 and L8 refer to Sentinel 2 and Landsat 8 satellites, respectively.

3.3.3. Model Development and Validation

Based on their scores a total of 11 models were selected (3 for Landsat 8, 3 for Sentinel-2 and 5 for the sUAS). Table 3.5 presents the models that best performed using the selection criteria regarding R^2 and AICc values. Table 3.6 presents the estimated coefficients for the selected algorithms.

Table 3.5. Best performing multiple variable water quality parameter (WQP) prediction algorithms derived from Landsat 8, Sentinel-2, and sUAS imagery. m and b refer to estimated slope (m) and y-intercept (b). R, G, B refer to red, green, and blue reflectance values, respectively. Success criterion for R^2 was established as $R^2 > 0.6$. RSME refers to Root Mean Square Error.

Platform	WQP	Model	R^2	AICc	RSME	Bias	p-value
Landsat 8	TSS	m*(B/G) + m*(B/R) – m*(R/B) – b	0.77	307.38	2.80	0.05	≤0.05
	SDD	m*(B/G) + m*(B/R) – m*(R/B) – b	0.66	291.70	6.98	0.03	≤0.05
	Chl-A	m*(R) + m*(B/G) – b	0.75	429.86	76.37	4.28	≤0.05
	TN	----	0.29	105.78	---	---	---
	TP	----	0.33	59.85	---	---	---
Sentinel-2	TSS	m*(B/G) + m*(B/R) – m*(R/B) + b	0.81	300.10	2.82	-0.32	≤0.05
	SDD	m*(B/G) + m*(B/R) – m*(R/B) + b	0.73	287.01	6.39	0.73	≤0.05
	Chl-A	m*(B/G) – m*(R/B) – b	0.78	453.11	71.03	2.34	≤0.05
	TN	----	0.41	223.92	---	---	---
	TP	----	0.33	135.29	---	---	---
sUAS	TSS	m*(B/R) – m*(G/R) + m*(G/B) + b	0.87	228.40	3.16	-0.12	≤0.05
	SDD	m*(B/R) – m*(G/R) + m*(G/B) - b	0.81	247.94	8.60	0.28	≤0.05
	Chl-A	m*(G) – m*(R) + b	0.81	409.76	104.92	-0.54	≤0.05
	TN	m*(B/R) – m*(G/R) + m*(G/B) + b	0.89	103.81	0.87	-0.02	≤0.05
	TP	m*(B/R) – m*(G/R) + m*(G/B) + b	0.88	49.604	0.36	-0.01	≤0.05

Table 3.6. Estimated coefficients for multiple variable water quality parameter (WQP) prediction algorithms derived from Landsat 8, Sentinel-2, and sUAS imagery. R, G, B refer to red, green, and blue reflectance values, respectively.

	WQP	Slope (m)					y-Intercept (b)
		$\frac{B}{G}$	$\frac{B}{R}$	$\frac{R}{B}$	Green	Red	
Landsat-8	TSS	70.11	15.84	103.14	--	--	161.85
	SDD	36.318	33.71	63.574	--	--	150.076
	Chl-a	436.8	--	505.0	--	--	773.0
	TN	--	--	--	--	--	--
	TP	--	--	--	--	--	--
Sentinel-2	TSS	133.253	160.715	3.397	--	--	55.172
	SDD	100.83	84.30	21.55	--	--	41.12
	Chl-a	824.5	--	979.6	--	--	1662.2
	TN	--	--	--	--	--	--
	TP	--	--	--	--	--	--
sUAS	TSS	264.5	148.2	185.2	--	--	215.3
	SDD	164.32	108.33	78.67	--	--	61.91
	Chl-a	--	--	--	9158.79	13,359	27.99
	TN	45.43	26.16	8.810	--	--	36.92
	TP	12.441	6.993	8.810	--	--	9.953

3.3.4. Spatial Distribution - Water Quality Maps Using Landsat 8, Sentinel-2 and sUAS imagery

To expand the limited and discrete in-situ sampling coverage for each system, multivariable prediction algorithms were applied to multispectral data collected by each platform, to generate maps of the spatial distribution of water quality according to Landsat 8 (Figure 3.6), Sentinel-2 (Figure 3.7) and the sUAS (Figure 3.8) in the low and high nutrient systems. From the spatial distribution maps, it can be observed that the output for all water quality parameters of all remote sensing platforms showed heterogenous waters in the low nutrient systems and partially mixed waters in the high nutrient system. These overall trends become clearer as the spatial resolution of the systems increases. Furthermore, when looking at the outputs of the optical water quality parameters (Chl-a, TSS, and SDD) for all platforms, in the low nutrient systems it is possible to observe that aquatic vegetation (located at the north-east section of the system) present at the time

of the in-situ sampling, is recognized by all platforms. This pattern also gets clearer as the spatial resolution of the imagery increases. Due to the low predictability ($R^2 \leq 0.47$) obtained for the non-optical water quality parameters (TN and TP) for Landsat 8 and Sentinel-2, the spatial distributions of these parameters using those platforms were not plotted. However, from the spatial distribution of TN and TP using the imagery collected with the sUAS ($R^2 \geq 0.8$) (Figure 3.9), the same pattern as described before can be observed.

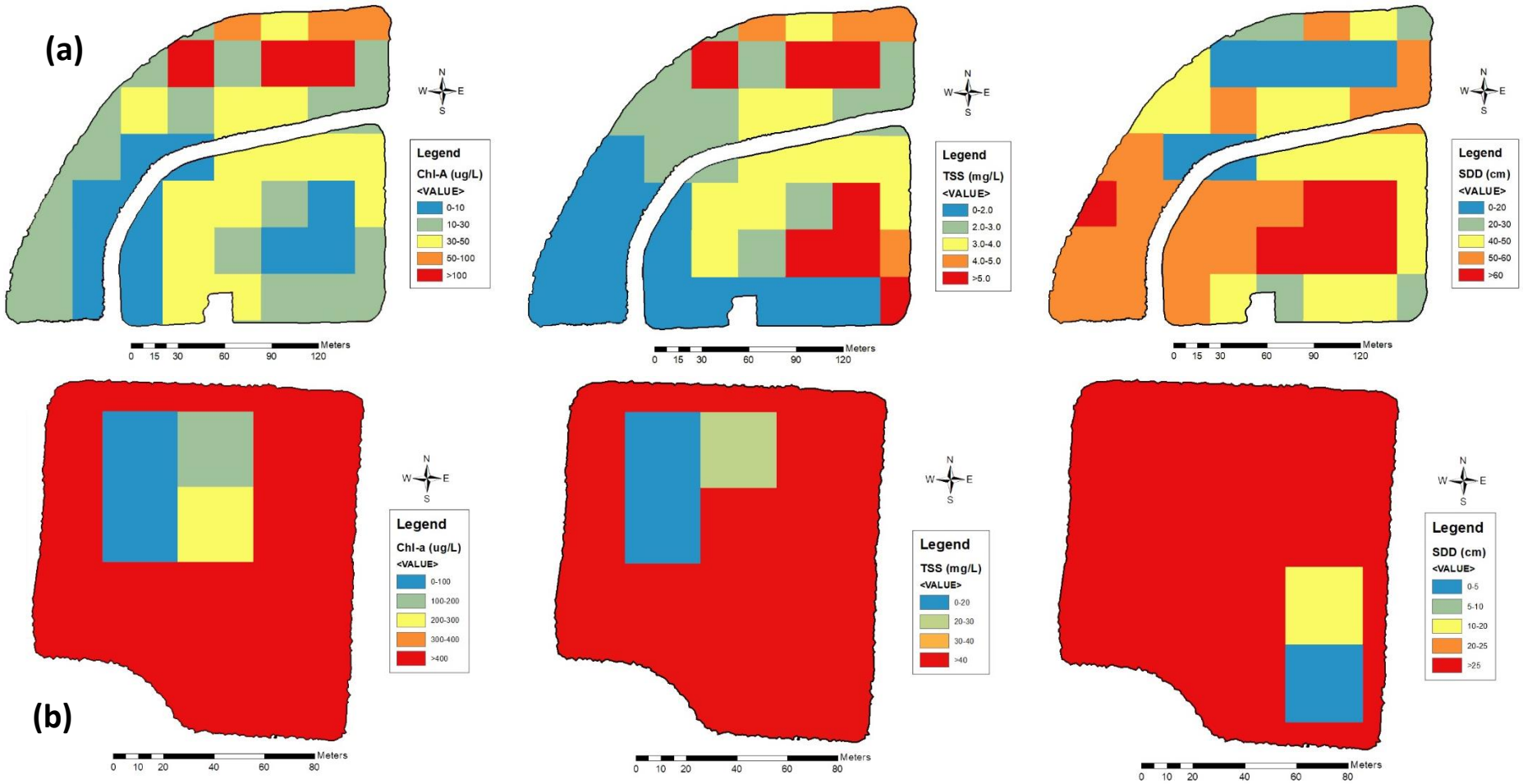

Figure 3.6. Spatial distribution of water quality in the low nutrient (a) and high nutrient (b) systems, using multispectral imagery collected by Landsat 8.

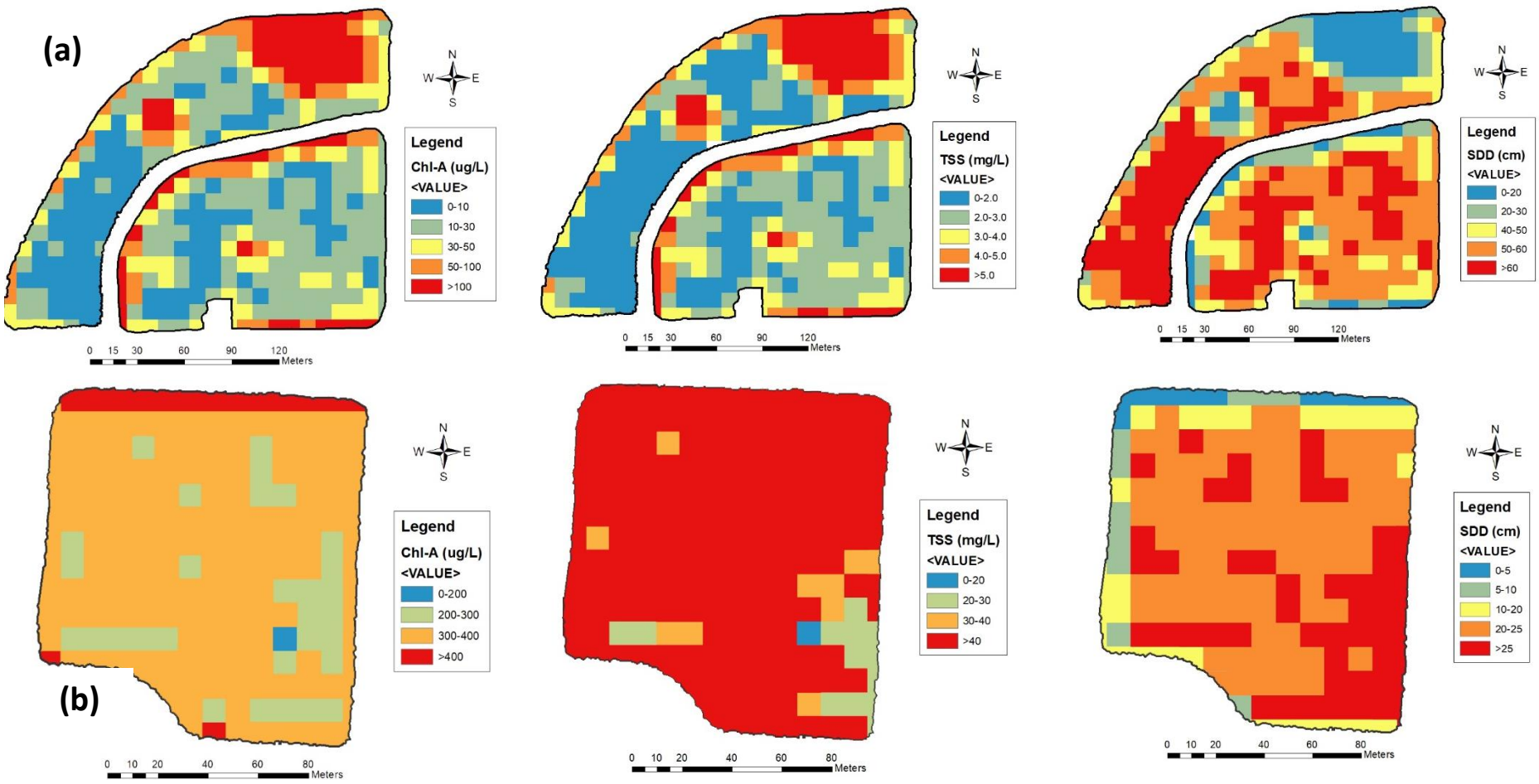

Figure 3.7. Spatial distribution of water quality in the low nutrient (a) and high nutrient (b) systems, using multispectral imagery collected by Sentinel-2.

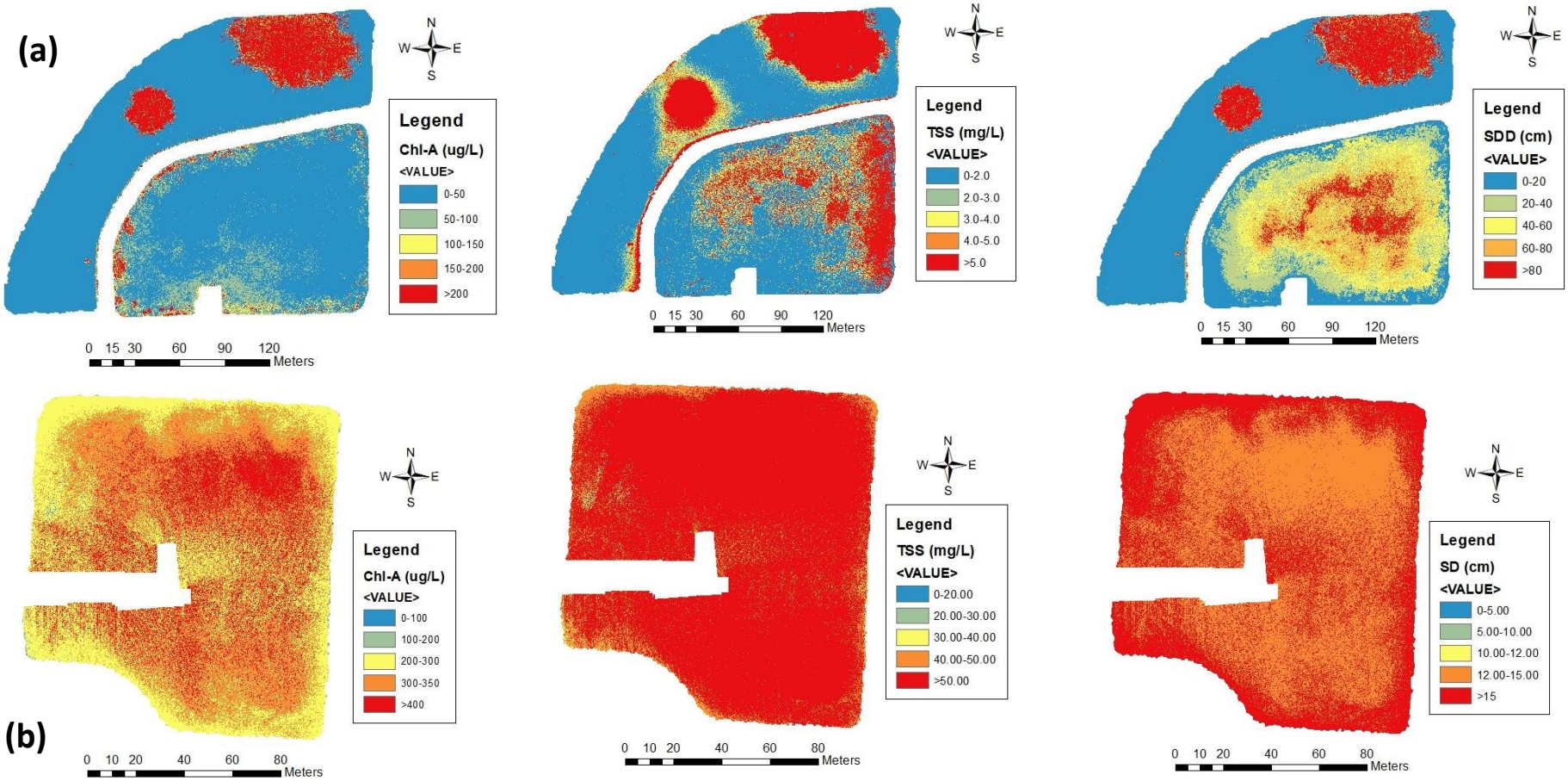

Figure 3.8. Spatial distribution of optical water quality in the low nutrient (a) and high nutrient (b) systems, using multispectral imagery collected by sUAS. Whited-out sections are due to the inability of the pre-processing software to properly stitch images at those locations

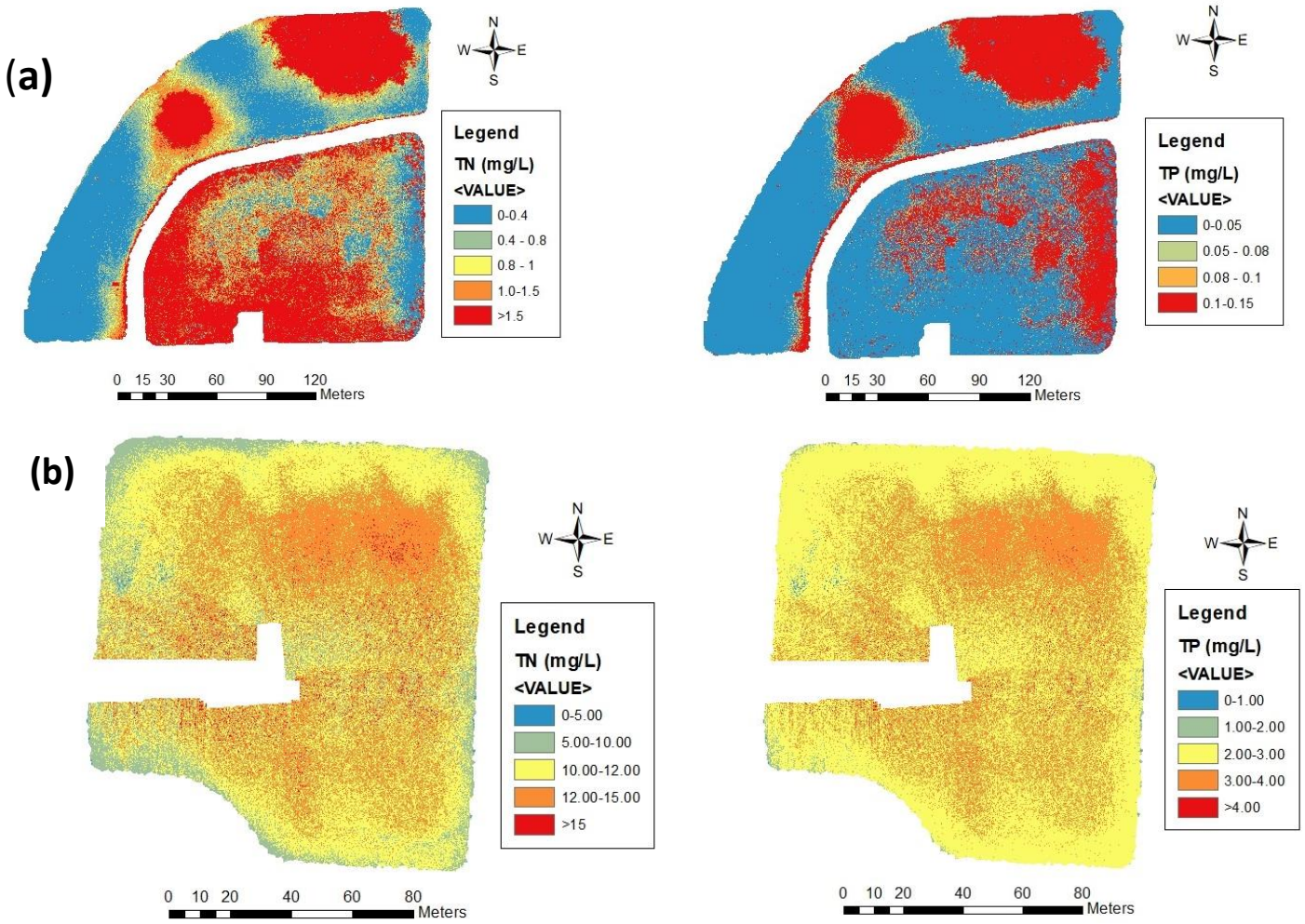

Figure 3.9. Spatial distribution of non-optical water quality in the low nutrient (a) and high nutrient (b) systems, using multispectral imagery collected by sUAS. Whited-out sections are due to the inability of the pre-processing software to properly stitch images at those locations

3.4. Discussion

The main purpose of this study was to use multispectral imagery from two satellite-based remote sensing tools (Landsat 8 and Sentinel-2) and a sUAS to model water quality in ecosystems of different biological productivities. To accomplish this objective, two systems located at opposite ends of the productivity spectrum were examined to derive algorithms capable of estimating optical (Chl-a, SDD, and TSS) and non-optical (TN and TP) water quality parameters. These statistical algorithms were developed by using a multivariable linear approach. It was determined that with the use of Landsat 8 and Sentinel-2, only optical (Chl-a, SDD, and TSS) water quality parameters could be reliably derived ($R^2 \geq 0.6$, p-value ≤ 0.01). However, algorithms using sUAS data reliably estimated not only optical but also non-optical (TN and TP) water quality parameters ($R^2 \geq 0.8$, p-value ≤ 0.01).

In terms of the interactions between the visible portion of the spectrum and optical water quality parameters, the findings are in accordance with Kloiber et al. (2002), Hellweger et al. (2004), Usali and Ismail (2015) and Bonansea et al. (2015), who concluded that different ratios among the visible portions of the spectrum provide strong predictive relationships for Chl-a, TSS and SDD. However (and as presented in Table 3.5), with the multispectral information captured with sUAS, strong relationships between the visible portions of the spectrum and non-optical parameters (TP and TN) can also be derived. To determine if novel compact multispectral sensors on-board sUAS present advantages over traditional satellite-based remote sensing tools (when it comes to modeling water quality), it is important to discuss the reason why these strong relationships between non-optical parameters and multispectral imagery captured by sUAS are possible. Non-optical water quality parameters were able to be estimated due to their relationships with optical parameters (Filstrup and Dowing, 2017). In this study for example, TN and TP exhibited strong collinearity with all

optical water quality parameters examined ($R \geq 0.92$ and $R \leq -0.94$). Statistical analyses performed in this study utilized these documented relationships and although the correlations were causative in nature, the authors believe the resulting non-optical models were environmentally and statistically valid. Furthermore, it was concluded these results were not a limitation to the developed models. Instead, future remote sensing water quality studies of shallow inland water bodies should take advantage of these indirect relationships to expand the predictive capabilities of multispectral driven statistical models (Sharaf and Zhang, 2017).

Gholizabeh et al. (2016) pointed out that in the past 30 years most of the studies that used satellite-based remote sensing tools have focused on predicting and monitoring optical parameters (turbidity, TSS, SDD, Chl-a) and that non-optical parameters (ammonia nitrogen (NH_3-N), TN, TP, and others) have been omitted due to their non-existent optical characteristics and problematically low signal-to-noise-ratio (SNR). In inland waters, low SNR is caused by the small amount of radiance leaving the water and the high amount contributed by the atmosphere (Pahlevan et al., 2014). In the best-case scenario, approximately 85% of the measured radiance is contributed by the atmosphere, while the remaining percentage is from the radiance leaving the water even after atmospheric corrections (Jorge et al., 2017). Currently, most of the satellite missions used for inland water monitoring and prediction (including but not restricted to Landsat 7 and 8, Sentinel-2) are equipped with sensors that have wide bandwidths and low SNR (Cao et al., 2019). The ability to identify substances in water using satellites is limited by the spatial resolution and the bandwidths (1992). Gerace et al. (2013) identified that the ideal product for monitoring and predicting inland water should exhibit four main characteristics: (1) high spatial resolution, (2) high radiometric resolution, (3) high temporal resolution, and (4) free data for the community. With the use of an sUAS, three (out of these four characteristics) are shown. By using an sUAS, spatial resolution can be increased by three orders of magnitude (Landsat 8

= 30 m, Sentinel-2 = 10 m, and sUAS = 6.20 cm or 0.062 m). As a result, sharper images can be obtained (Figure 3.10). With the increased spatial resolution, strong and more predictive optical and non-optical water quality models ($R^2 \geq 0.85$) (Table 3.5) can be obtained. Theoretically, and as described by Vanhellomont and Ruddick (2015), to increase the low SNR problem, degradation of the spatial resolution is employed. Unfortunately, SNR for the data generated with the sUAS was not directly measured in this study, so to confirm these findings, further work should focus on measuring the SNR from the multispectral data collected with sUAS.

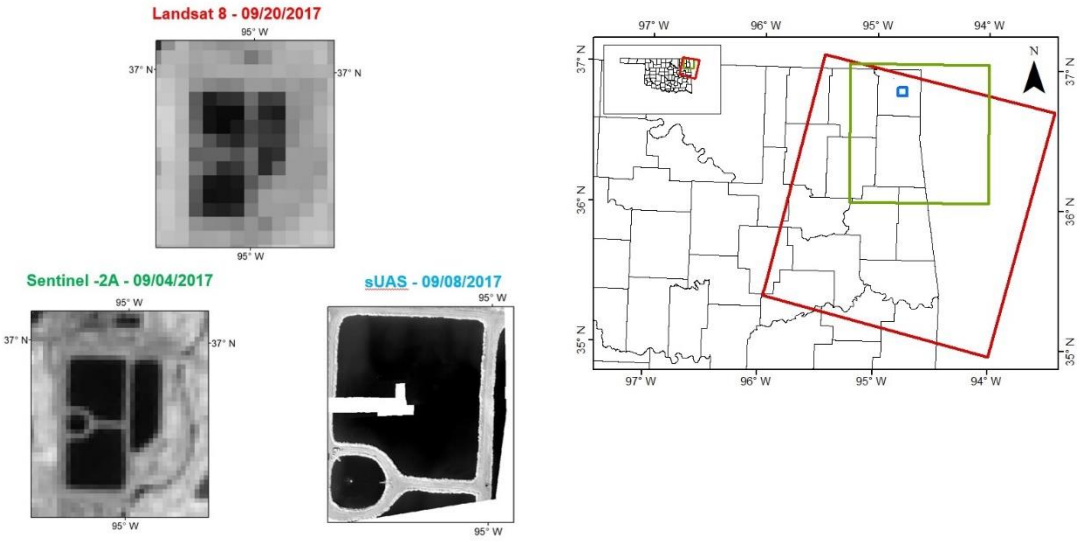

Figure 3.10. Footprint of the imagery taken by Landsat 8 (red), Sentinel-2 (green) and sUAS (blue), with zoomed images on the high nutrient system for both satellites and sUAS.

There is little doubt that spatial resolution improvements obtained with sUAS are one of the most important advantages that these novel systems offer. This improvement is particularly relevant for small inland water bodies and is visible when comparing spatial distribution maps presented in section 3.4. As mentioned previously, when pairing the multivariable prediction algorithms with the multispectral data collected by each platform, the output generated from all platforms presents an overall trend indicating heterogenous waters in the low nutrient systems and partially mixed waters in the high nutrient system. These results are in

accordance with the measured water quality parameters. As presented in Table 3.4, it can be observed that the measured in-situ water quality parameters present the same heterogenous and partially mixed conditions. However, and as observed in Figures 3.6, 3.7, and 3.8, as the spatial resolution increases, more detailed information can be obtained from outputs generated from imagery with higher and sharper spatial resolution. Having the ability of obtaining sharper images becomes particularly relevant when trying to minimize the source of error that can be introduced by mixed pixels (especially with coarse-resolution data (e.g., 30 x 30 m in the case of Landsat-8)) when performing a simple water surface reflectance extraction at the pixel level (Deus et al., 2013; Huang et al., 2018).

Higher spatial resolution is not the only benefit that sUAS may offer. Kloiber et al. (2002) identified that one of the major drawbacks when using satellite-based imagery is data loss due to cloud coverage. Spectral energy cannot be transmitted through clouds, therefore, because sUAS fly below the clouds MS imagery can still be collected with proper planning. However, one must account for changes to illumination throughout the mission, a procedure that can be readily and relatively easily completed. In several cases (especially when performing time-series analyses), data loss due to cloud coverage has inhibited the use of up to 70% of the collected satellite data (Olmanson et al., 2008; Peng et al., 2015; Xiao et al., 2018). Because sUAS fly below the clouds, all imagery collected with these systems is completely cloud-free.

To these advantages, one must also add the flexibility that sUAS offer in terms of temporal resolution. Hicks et al. (2013) note that researchers that attempt to correlate satellite-derived spectral imagery with water quality parameters should perform in situ water quality data no more than one day apart from the satellite imagery collection. As mentioned by several authors, due to the temporal resolution of satellite platforms and cloud coverage limitations,

the probability of doing so is extremely low (Kloiber et al., 2002; Asner, 2010; Peng et al., 2015; Xiao et al., 2018). With sUAS, the operator can decide how often to perform an imagery collection campaign. This flexibility and power become extremely relevant when monitoring small systems or those that are in a constant state of change. At the same time, it gives researchers the ability to collect imagery the same day as the in-situ sampling is completed (as presented in this study).

However, sUAS is by no means a tool free of fault. Because these systems fly below the clouds, meteorological conditions (e.g., winds gusts and wind shear) and adverse weather conditions (e.g., rain, snow, fog, and humidity) are limiting factors that can not only affect the quality and precision of the imagery (Seifert et al., 2019), but also compromise the safety and integrity of the platform. Furthermore, because this technology is relatively new, as are the tools used to process the imagery captured by these platforms, another limiting factor is that proprietary and open-source software used to create full orthomosaic images, digital surface models (DSM), point clouds, index maps, 3D models and thermal maps is unable to properly stitch images over large surfaces of water or dense vegetation without ground control points, due to the lack of individual images with homogeneous surfaces (Arango et al., 2020). As shown in Figures 3.8 and 3.9, this limitation can cause loss of data (whited-out section on both systems).

Taking into consideration all the above information, does the use of sUAS present an advantage over satellite-based remote sensing tools when with regards to the modeling of water quality? From the spatial and temporal resolution perspectives, as well as the ability to predict and monitor optical and non-optical water quality parameters, one may argue that the answer appears to be yes. However, the researcher must clearly define the goals, boundaries,

and extent of the project, and understand the limitations of these novel tools so that the quality of the data and results are not compromised.

3.5. Conclusions

This study aimed to compare multispectral imagery from two satellite-based remote sensing tools (Landsat 8 and Sentinel-2) and a sUAS to determine if traditional remote sensing technologies present advantages over the novel use of compact multispectral sensors on-board sUAS, when developing predictive and monitoring algorithms for water quality parameters. From the results herein, the following conclusions may be drawn:

With the use of imagery captured by an sUAS, and a thorough understanding of the existing relationships between water quality components in the systems involved, optical and non-optical water quality parameters can be estimated. Similar to other studies and as reported in the findings of this manuscript, it is apparent that the visible portion of the spectrum best describes predictive interactions with water quality parameters. Understanding the different limitations of traditional remote sensing (e.g., cloud coverage problems, necessary atmospheric correction, adjacency, temporal and radiometric resolution), sUAS collected data provides the opportunity to improve the reliability of surface water quality models. Although sUAS imagery increased the regression coefficients for the different evaluated models for this study, the major limitations experienced when operating an sUAS are caused by: flight restrictions, safety (improper piloting/ high wind speeds/ unclear airspace designations), battery life (~20 minutes, which in turn decreases the size of the scene), and on-board sensor accuracy (large bandwidths, and limited GPS precision),Further research should focus on addressing the limitations of remotely sensing bottom vegetation and substrate in optical shallow bodies of water.

References

Aerial Technology International. ATI AgBOT Data Sheet. Available online: http://store.aerialtechnology.com/ product/agbot-2/ (accessed on 1 May 2020).

Agudo, P.U.; Pajas, J.A.; Pérez-Cabello, F.; Redón, J.V.; Lebrón, B.E. The potential of drones and sensors to enhance detection of archaeological cropmarks: a comparative study between multispectral and thermal imagery. Drones 2018, 2, 29.

Akaike, H. Information Theory and an Extension of the Maximum Likelihood Principle. In Proceedings of the 2nd International Symposium on Information Theory, Tsahkadsor, Armenia, 2–8 September 1971; Akadémiai Kiadó: Budapest, Hungary, 1973; pp. 267–281.

Arabi, B.; Salama, S.; Pitarch, J.; Verhoef, W. Integration of in-situ and multi-sensor satellite observations for long-term water quality monitoring in coastal areas. Remote Sensing of Environment 2020, 239.

Arango, J.G.; Holzbauer-Schweitzer, B.K.; Nairn, R.W.; Knox, R.C. Generation of geolocated and radiometrically corrected true reflectance surfaces in the visible portion of the electromagnetic spectrum over large bodies of water using images from a sUAS. Journal of Unmanned Vehicle Systems 2020, 1.

Arango, J.G.; Nairn, R.W. Prediction of optical and non-optical water quality parameters in oligotrophic and eutrophic aquatic systems using a small unmanned aerial system. Drones 2020, 4,1.

ArcMap; Computer Software; Environmental Systems Research Institute (ESRI): Redlands, CA, USA, 2012.

Asner, G.P. Cloud cover in Landsat observations of the Brazilian amazon. International Journal of Remote Sensing 2010, 22, 3855–3862.

Avitabile, V.; Baccini, A.; Friedl, M.A.; Schmullius, C. Capabilities and limitations of Landsat and land cover data for aboveground woody biomass estimation of Uganda. Remote Sensing of Environment 2012, 17, 366-380.

Baird, R.B.; Eaton, A.D.; Rice, E.W. 2017. Standard Methods for the Examination of Water and Wastewater, 23rd ed.; American Public Health Association, American Water Works Association, and Water Environment Federation. 1796 pp.

Barnwal, P.; Kotani, K. Climatic impacts across agricultural crop yield distributions: An application of quantile regression on rice crops in Andhra Pradesh, India. Ecological Economics 2013, 87. 95-109.

Becker, R.H.; Sayer, M.; Dehm, D.; Shucman, R.; Quintero, K.; Bosse, K.; Sawtell, R. Unmanned aerial system based spectroradiometer for monitoring harmful algal blooms: A new paradigm in water quality monitoring. Journal of Great Lakes Research 2019, 45(3), 444-453.

Berbar, M.A.; Gaber, S.F. Clouds and shadows detection and removing from remote sensing images. International Conference on Electrical, Electronic and Computer Engineering 2004, 75-79.

Boland, D.H.P. Trophic Classification of Lakes Using Landsat-I (ERTS-l) Multispectral Scanner Data, Corvallis, OR: United States Environmental Protection Agency, Office of Research and Development, Corvallis Environmental Research Laboratory, 1976.

Bonansea, M.; Rodriguez, M.C.; Pinotti, L.; Ferrero, S. Using multi-temporal Landsat imagery and linear mixed models for assessing water quality parameters in Río Tercero Reservoir (Argentina). Remote Sensing of Environment 2015, 158, 28–41.

Bonsch, M.; Popp, A.; Biewald, A.; Rolinski, S.; Schmitz, C.; Weindl, I.; Stevanovic, M.; Högner, K.; Heinke, J.; Ostberg, S.; Dietrich, J.P.; Bodirsky, B.; Lotze-Campen, H.; Humpenöder, F. Environmental flow provision: Implications for agricultural water and land-use at the global scale. Global Environmental Change 2015, 30, 113-132.

Bosch, N.S.; Evans, M.A.; Scavia, D.; Allan, J.D. Interacting effects of climate change and agricultural BMPs on nutrient runoff entering Lake Erie. Journal of Great Lakes Research 2014 40(3), 581-589.

Brezonik, P.L.; Olmanson, L.G.; Finlay, J.G.; Bauer, M.E. Factors affecting the measurement of CDOM by remote sensing of optically complex inland waters. Remote Sensing of Environment 2015, 157, 199-215.

Burns, J. The dynamics of accounting change Inter-play between new practices, routines, institutions, power and politics. Accounting, Auditing & Accountability Journal 2000, 12(5), 566-596.

Butt, M.J.; Nazeer, M. Landsat ETM+ Secchi Disc Transparency (SDT) retrievals for Rawal Lake, Pakistan. Advances in Space Research 2015, 56(7), 1428-1440.

Cannizzaro, J.P.; Carder, K.L. Estimating chlorophyll a concentrations from remote-sensing reflectance in optically shallow waters. Remote Sensing of Environment 2006, 101(1), 13-24.

Cao, Z.; Ma, R.; Xue, K. Effects of broad bandwidth on the remote sensing of inland waters: Implications for high spatial resolution satellite data applications. ISPRS Journal of Photogrammetry and Remote Sensing 2019, 153, 110-122.

Chen, S.; Han, L.; Chen, X.; Li, D.; Sun, L.; Li, Y. Estimating wide range Total Suspended Solids concentrations from MODIS 250-m imageries: An improved method. ISPRS Journal of Photogrammetry and Remote Sensing 2015, 99, 58-69.

Culbertson, A.M., Martin, J.F., Aloysius, N., Ludsin, S.A. Anticipated impacts of climate change on 21st century Maumee River discharge and nutrient loads. Journal of Great Lakes Research 2016, 42(6), 1332-1342.

Darecki, M.; Weeks, A.; Sagan, S.; Kowalczuk, P.; Kaczmarek, S. Optical characteristics of two contrasting Case 2 waters and their influence on remote sensing algorithms. Continental Shelf Research 2003, 23(3-4), 237-250.

de Oca, A. M.; Arreola, L.; Flores, A.; Sanchez, J.; Flores, G. Low-cost multispectral imaging system for crop monitoring. International Conference on Unmanned Aircraft Systems (ICUAS), Dallas, TX, 2018, 443-451.

Decker, A.G.; Malthus, T.J.; Wijnen, M.M.; Seyhan, E. The effect of spectral bandwidth and positioning on the spectral signature analysis of inland waters. Remote Sensing of Environment 1992, 41(2-3), 211-225.

Deus, D.; Gloaguen, R. Remote Sensing Analysis of Lake Dynamics in Semi-Arid Regions: Implication for Water Resource Management. Lake Manyara, East African Rift, Northern Tanzania. Water 2013, 5, 698-727.

Doña, C.; Chang, N.; Caselles, V.; Sánchez, J.M.; Camacho, A.; Delegido, J.; Vannah, B.W. Integrated satellite data fusion and mining for monitoring lake water quality status of the Albufera de Valencia in Spain. Journal of Environmental Management 2015, 151, 416-426.

ESA Senitenl-2 Team. GMES Sentinel-2 Mission Requirements Document. EOP-SM/1163/MR-dr. Date Issued: 30/01/2017. Available online: https://earth.esa.int/pub/ESA_DOC/GMES_Sentinel2_MRD_issue_ 2.0_update.pdf (accessed on 1 May 2020).

European Space Agency. Sentinel Application Platform (SNAP). Available online: https://step.esa.int/main/download/snap-download/ (accessed on 1 May 2020).

European Space Agency. Sentinel-2 Sen2Cor. Available online: http://step.esa.int/main/third-party-plugins-2/sen2cor/sen2cor_v2-8/ (accessed on 1 May 2020).

Filstrup, C.; Dowing, J.A. Relationship of chlorophyll to phosphorus and nitrogen in nutrient-rich lakes. Inland Waters 2017, 7(4), 385-400.

Gerace, A.; Schott, A.D.; Nevins, R. Increased potential to monitor water quality in the near-shore environment with Landsat's next-generation satellite. Journal of Applied Remote Sensing 2013, 7(1).

Gholizadeh, M.H.; Melesse, A.M.; Reddi, L. A Comprehensive Review on Water Quality Parameters Estimation Using Remote Sensing Techniques. Sensors 2016, 16(8), 1298.

Gomes, I.; Peteiro, L.; Bueno-Pardo, J.; Albuquerque, R.; Pérez-Jorge, S.; Oliveira, E.R.; Alves, F.L.; Queiroga, H. What's a picture really worth? On the use of drone aerial imagery

to estimate intertidal rocky shore mussel demographic parameters. Estuarine, Coastal and Shelf Science 2018, 213, 185-198.

Gould, R.; Arnone, R.; Martinolich, P. Spectral dependence of the scattering coefficient in case 1 and case 2 waters. Applied Optics 1999, 38, 2377-2383.

Hails, R. Assessing the risks associated with new agricultural practices. Nature 2002, 418, 685-688.

Han, H.; Allan, J.D., Bosch, N.S. Historical pattern of phosphorus loading to Lake Erie watersheds. Journal of Great Lakes Research 2012, 38(2), 289-298.

Hellweger, F.L.; Schlosser, P.; Lall, U.; Weissel, J.K. Use of satellite imagery for water quality studies in New York Harbor. Estuarine, Coastal and Shelf Science 2004, 61(3), 437-448.

Hertel, T.W.; Lobell, D.B. Agricultural adaptation to climate change in rich and poor countries: Current modeling practice and potential for empirical contributions. Energy Economics 2014, 46, 562-575.

Hicks, B.J.; Stichbury, G.A.; Brabyn, L.K.; Allan, M.G.; Ashraf, S. Hindcasting water clarity from Landsat satellite images of unmonitored shallow lakes in the Waikato Region, New Zealand. Environmental Monitoring Assessment 2013, 185, 7245–7261.

Howarth, R.W.; Sharpley, A.; Walker, D. Sources of nutrient pollution to coastal waters in the United States: Implications for achieving coastal water quality goals. Estuaries 2002, 25, 656–676.

Hu, C.; Lee, Z.; Franz, B. Chlorophyll algorithms for oligotrophic oceans: A novel approach based on three-band reflectance difference. Journal of Geophysical Research Oceans 2012, 117.

Huang, C.; Chen, Y.; Zhang, S.; Wu, J. Detecting, Extracting, and monitoring surface water from space using optical sensors: A review. Reviews of Geophysics, 2018, 56, 33-360.

Jorge, D.S.F.; Barbosa, C.C.F.; De Carvalho, L.A.S.; Affonso, A.G.; Lobo, F.D.L.; Novo, E.M.L.D.M. SNR (Signal-To-Noise Ratio) impact on water constituent retrieval from simulated images of optically complex Amazon Lakes. Remote Sensing 2017, 9, 644.

Keiser, D.A.; Shapiro, J.S. Consequences of the Clean Water Act and the Demand for Water Quality. The Quarterly Journal of Economics 2019, 134(1), 349-396.

Kloiber, S.M.; Brezonik, P.L.; Olmanson, L.G.; Bauer, M.V. A procedure for regional lake water clarity assessment using landsat multispectral data. Remote Sensing of Environment 2002, 82, 38–47.

Kutser, T.; Pierson, D.C.; Kallio, K.Y.; Reinart, A.; Sobek, S. Mapping lake CDOM by satellite remote sensing. Remote Sensing of Environment 2005, 94(1), 535-540.

LaBeau, M.B.; Gorman, H.; Mayer, A.; Dempsey, D.; Sherrin, A. Tributary phosphorus monitoring in the U.S. portion of the Laurentian Great Lake Basin: Drivers and challenges. Journal of Great Lakes Research 2013, 39(3), 569-577.

Laili, N.; Arafah, F.; Jaelani, L. M.; Subehi, L.; Pamungkas, A.; Koenhardono, E. S.; Sulisetyono, A. Development of water quality parameter retrieval algorithms for estimating total suspended solids and chlorophyll-a concentration using Landsat-8 imagery at Poteran Island water. SPRS Ann. Photogramm. Remote Sens. Spatial Inf. Sci. 2015, 2.

Lathrop, R.; Castle, R.; Lillesand, T. Monitoring River Plume Transport and Mesoscale Circulation in Green Bay, Lake Michigan, Through Satellite Remote Sensing. Journal of Great Lakes Research 1990, 16(3), 471-484.

Leon, L.F.; Soulis, E.D.; Kouwen, N.; Farquhar, G.J. Nonpoint source pollution: a distributed water quality modeling approach. Water Research 2001, 35(1), 997-1007.

Liyanage, C.P.; Yamada, K. Impact of Population Growth on the Water Quality of Natural Water Bodies. Sustainability 2017, 9, 1405.

Mannino, A.; Russ, M.E.; Hooker, S.B. Algorithm development and validation for satellite-derived distributions of DOC and CDOM in the US Middle Atlantic Bight. Journal of Geophysical Research Oceans 2008, 113(C7).

Matsushita, B.; Yang, W.; Chang, P.; Yang, F.; Fukushima, T. A simple method for distinguishing global Case-1 and Case-2 waters using SeaWiFS measurements. ISPRS Journal of Photogrammetry and Remote Sensing 2012, 69, 74-87.

Matthews, M.W. A current review of empirical procedures of remote sensing in inland and near-coastal transitional waters. International Journal of Remote Sensing 2011, 32(21), 6855-6899.

Matthews, M.W. A current review of empirical procedures of remote sensing in inland and near-coastal transitional waters. International Journal of Remote Sensing 2011, 32(21), 6855-6899.

McCullough, I.; Loftin, C.; Sader, S. Landsat imagery reveals declining clarity of Maine's lakes during 1995–2010. Freshwater Science 2013, 32(3), 741-752.

Mesonet. Local Conditions. Available online: https://www.mesonet.org/index.php/weather/local (accessed on 1 May 2020).

Mission Planner; Computer Software. ArduPilot Development Team. Available online: https://ardupilot.org/ planner/ (accessed on 1 May 2020).

Mogili, U.R.; Deepak, B.BV.L. Review on application of drone systems in precision agriculture. Procedia Computer Science 2018, 133, 502-509.

Olmanson, L.G.; Bauer, M.E.; Brezonik, P.L. A 20-year Landsat water clarity census of Minnesota's 10,000 lakes. Remote Sensing of Environment 2008, 112, 4086–4097.

Pahlevan, N.; Lee, Z.; Wei, J.; Schaaf, C.B.; Schott, J.R.; Berk, A. On-orbit radiometric characterization of OLI (Landsat-8) for applications in aquatic remote sensing. Remote Sensing of Environment 2014, 154, 272-284.

Park, Y.; Ruddick, K. Model of remote-sensing reflectance including bidirectional effects for case 1 and case 2 waters. Applied Optics 2005, 44, 1236-1249.

Peng, L.; Zhiming, F.; Chiwei, X. Acquisition probability differences in cloud coverage of the available Landsat observations over mainland Southeast Asia from 1986 to 2015. International Journal of Digital Earth. 2015, 11(5), 437-450.

R Core Team. R Computer Software; R Core Team: Vienna, Austria, 2017.

Refaeilzadeh P., Tang L., Liu H. Cross-Validation. In Encyclopedia of Database Systems, 1st ed; Liu, L., Ozsu, M.T.; Springer US: Boston, MA, USA, 2009, Volume 1, pp. 532-538.

Regina, C. L.; Martinez, J.; Da Motta Marques, D.; Cirilo, J. A.; Carlos, R. F. Assessment of chlorophyll-a remote sensing algorithms in a productive tropical estuarine-lagoon system. Remote Sensing 2017, 9(6).

Reilly, J.; Hohmann, N.; Kane, S. Climate change and agricultural trade: Who benefits, who loses? Global Environmental Change 1994, 4(1), 24-36.

Rui, Y.; Fu, D.; Do Minh, H.; Radhakrishnan, M.; Zevenbergen, C.; Pathirana, A. Urban Surface Water Quality, Flood Water Quality and Human Health Impacts in Chinese Cities. What Do We Know? Water 2018, 10, 240.

Sano, E.E.; Ferreira, L.G.; Asner, G.P.; Steinke, E.T. Spatial and temporal probabilities of obtaining cloud-free Landsat images over the Brazilian tropical savanna. International Journal of Remote Sensing 2007, 28(12), 2739-2752.

Schraga, T., Cloern, J. Water quality measurements in San Francisco Bay by the U.S. Geological Survey, 1969–2015. Sci Data 2017, 4.

Scott, A.B.; Frost, P.C. Monitoring water quality in Toronto's urban stormwater ponds: Assessing participation rates and data quality of water sampling by citizen scientists in the FreshWater Watch. Science of The Total Environment 2017, 592, 738-744.

Seifert, E.; Seifert, S.; Vogt, H.; Drew, D.; van Aardt, J.; Kunneke, A.; Seifert, T. Influence of Drone Altitude, Image Overlap, and Optical Sensor Resolution on Multi-View Reconstruction of Forest Images. Remote Sens. 2019, 11, 1252.

Sharaf El Din, E.; Zhang, Y. Estimation of both optical and nonoptical surface water quality parameters using Landsat 8 OLI imagery and statistical techniques. Journal of Applied Remote Sensing 2017, 11(4).

Stavrakoudis, D.; Katsantonis, D.; Kadoglidou, K.; Kalaitzidis, A.; Gitas, I.Z. Estimating rice agronomic traits using drone-collected multispectral imagery. Remote Sensing 2019, 11, 545.

Strokal, M.; Spanier, J.E.; Kroeze, C.; Koelmans, A.A.; Florke, M.; Franssen, W.; Hofstra, N.; Langan, S.; Tang, T.; Vliet, M.T.; Wada, Y.; Wang, M.; Wijnen, J.V.; Williams, R. Global multi-pollutant modelling of water quality: scientific challenges and future directions. Current Opinion in Environmental Sustainability 2019, 36, 116-125.

Tang, L.; Shao, G. Drone remote sensing for forestry research and practices. Journal of Forestry Research. 2015, 26, 791–797.

Thorp, K.R.; Thompson, A.L.; Harders, S.J.; French, A.N.; Ward, R.W. High-throughput phenotyping of crop water use efficiency via multispectral drone imagery and a daily soil water balance model. Remote sensing 2018, 10, 1682.

United States Environmental Protection Agency. 2012 Guidelines for Water Reuse. US EPA Office of Research and Development, Washington, DC, EPA/600/R-12/618, 2012.

United States Environmental Protection Agency. Methods for Chemical Analysis of Waters and Waste Waters; EPA/600/4-79/020 (NTIS PB84128677); U.S. Environmental Protection Agency: Washington, DC, USA, 2002.

United States Geological Survey. EarthExplorer. Available online: https://earthexplorer.usgs.gov/ (accessed on 1 May 2020).

United States Geological Survey. Landsat Missions – Landsat 8. Available online: https://www.usgs.gov/land-resources/nli/landsat/landsat-8?qt-

science_support_page_related_con=0#qt-science_support_page_related_con (accessed on 1 May 2020).

United States Geological Survey. National Land Cover (NLCD) 2016. Available online: https://www.mrlc.gov/national-land-cover-database-nlcd-2016 (accessed on 1 May 2020).

Usali, N.; Ismal, M.H., Use of Remote Sensing and GIS in Monitoring Water Quality. Journal of Sustainable Development 2010, 3(3).

Vanhellemont, Q.; Ruddick, K. Advantages of high-quality SWIR bands for ocean colour processing: Examples from Landsat-8. Remote Sensing of Environment 2015, 161, 89-106.

Wang, C.; Li, W.; Chen, S.; Li, D.; Wang, D.; Liu, J. The spatial and temporal variation of total suspended solid concentration in Pearl River Estuary during 1987–2015 based on remote sensing. Science of The Total Environment 2018, 618, 1125-1138.

Xiao, C.; Li, P.; Feng, Z.; Wu, X. Spatio-temporal differences in cloud cover of Landsat-8 OLI observations across China during 2013–2016. Journal of Geographical Sciences 2018, 28, 429-444.

Zeng, C.; Richardson, M.; King. D.J. The impacts of environmental variables on water reflectance measured using a lightweight unmanned aerial vehicle (UAV)-based spectrometer system. ISPRS Journal of Photogrammetry and Remote Sensing 2017, 130, 217-230.

Zhao, C.S.; Yang, S.T.; Liu, C.M.; Dou, T.W.; Yang, Z.L.; Liu, X.L.; Xiang, H.; Nie, S.Y.; Zhang, J.L., Mitrovic, S.M., Yu, Q., Lim, R.P. Linking hydrologic, physical and chemical habitat environments for the potential assessment of fish community rehabilitation in a developing city. Journal of Hydrology 2015, 523, 384-397.

Zhao, C.S.; Yang, Y.; Yang, S.T.; Xiang, H.; Wang, F.; Chen, X.; Zhang, H.M.; Yu, Q. Impact of spatial variations in water quality and hydrological factors on the food-web structure in urban aquatic environments. Water Research 2019, 153, 121-133.

CHAPTER 4 – Generation of Geolocated and Radiometrically Corrected True Reflectance Surfaces in the Visible Portion of the Electromagnetic Spectrum Over Large Bodies of Water using Images from an sUAS

Work presented in this chapter has been accepted and published in the *Journal of Unmanned Vehicle Systems* 2020, 8(3): 172-185.

Abstract: The focus of this study was to develop true reflectance surfaces in the visible portion of the electromagnetic spectrum from small Unoccupied Aerial System (sUAS) images obtained over large bodies of water when no ground control points were available. The goal of the research was to produce true reflectance surfaces from which reflectance values could be extracted and used to estimate optical water quality parameters utilizing limited in-situ water quality analyses. Multispectral imagery was collected using a sUAS equipped with a multispectral sensor, capable of obtaining information in the blue (0.475 μm), green (0.560 μm), red (0.668 μm), red edge (0.717 μm) and near infrared (0.840 μm) portions of the electromagnetic spectrum. In order to develop a reliable and repeatable protocol, a five-step methodology was implemented: (1) image and water quality data collection, (2) image processing, (3) reflectance extraction, (4) statistical interpolation and (5) data validation. Results indicate that the created protocol generates geolocated and radiometrically corrected true reflectance surfaces from sUAS missions flown over large bodies of water. Subsequently, relationships between true reflectance values and in-situ water quality parameters were developed.

Keywords: Remote Sensing, Small Unoccupied Aerial System, Stitching, Water Quality

4.1. Introduction

The collection of high-resolution images using small Unoccupied Aerial Systems (sUAS) is widespread (e.g., Colomina and Molina, 2014; Rusnak et al., 2018; Louhaichi et al., 2018; Doughty and Cavanaugh, 2019; Melville et al., 2019;). Equipping a sUAS with multispectral sensors allows collection of cloud free images with shorter temporal resolutions and smaller spatial resolutions (compared to satellites) at relatively low cost (Berni et al., 2008; Nebiker et al., 2016).

A typical image collection using a sUAS involves three stages: mission planning, flight and data acquisition, and image pre-processing (Nex and Romondino, 2013). The mission planning stage refers to using software to create the flight path that the sUAS follows. The most common approach for flight path planning is the creation of a closed polygonal path on a two-dimensional map, supplemented with information such as mission altitude (height above ground level (AGL)), ground speed, focal length, camera field of view (FOV), image overlap and shutter speed, in order to generate optimal flyable routes (Tulum et al., 2009; Fraichard, 2012; Valero-Gomez et al., 2013; Shi and Ng, 2018).

The second stage (flight and data acquisition) executes the designed mission. The sUAS can perform flights in manual (i.e., pilot in command via remote control) or autonomous mode, i.e., navigation and control determined by onboard inertial sensors (e.g., accelerometers, gyroscopes, magnetometers) and Global Positioning Systems (GPS) waypoints (Nex and Romondino, 2013). Data acquisition is achieved using these features (Eisenbesis, 2004). In manual mode, image overlapping can be irregular; in autonomous mode, overlapping shows significant improvement (Nex and Romondino, 2013).

After collection, raw sUAS images contain geometric distortions that inhibit use in Geographic Information Systems (GIS) applications (Toutin, 2002). Distortions are associated with variations in movement and attitude of the aircraft, atmospheric effects (i.e., refraction), or topographic effects (Xiang and Tian, 2010). The image pre-processing stage refers to geometric and radiometric corrections to the raw sUAS data (Perez et al., 2012). Two approaches have traditionally been used: (1) georectification using Ground Control Points (GCPs) and (2) georectification using inertial navigation systems (De Leeuw et al., 1988). GCPs are markers with known locations that can be observed/identified in the obtained imagery and used to empirically determine a mathematical coordinate transformation to correct the geometry of the sUAS images (Kardoulas et al., 1996). Inertial navigation system data refers to the actual position and movement of the aircraft (i.e., pitch, roll, yaw, velocity and AGL). Once corrected, images undergo a stitching process where identification and selection of matching tie points on the overlapping sections of the images helps to create a complete orthorectified image of the flown area (Laliberte et al., 2011).

The processes described above can be automated by proprietary or open-source software. Available products can create point clouds, Digital Surface Models (DSM), 3D Models, index maps, thermal maps and full orthomosaic images. However, currently these tools are not capable of properly stitching images captured over large bodies of water or dense terrestrial vegetation (Li et al., 2016; Agisoft, 2019; Pix4D, 2019). The fundamental issue is the lack of tie points in individual images with homogeneous surfaces. For this reason, current image processing protocols fail to generate fully orthorectified images for such missions. This paper presents an alternative approach that can generate complete geolocated and radiometrically corrected true reflectance surfaces in the visible portion of the electromagnetic spectrum, of large bodies of waters, using a statistical interpolation method from images taken with a multispectral sensor onboard a sUAS.

4.2.Methodology

To develop the overall protocol, a five-step methodology was implemented: (1) Image and water quality data collection, (2) Image processing, (3) Reflectance extraction, (4) Statistical interpolation and (5) Data validation. Figure 4.1 shows the postprocessing protocol for the multispectral imagery.

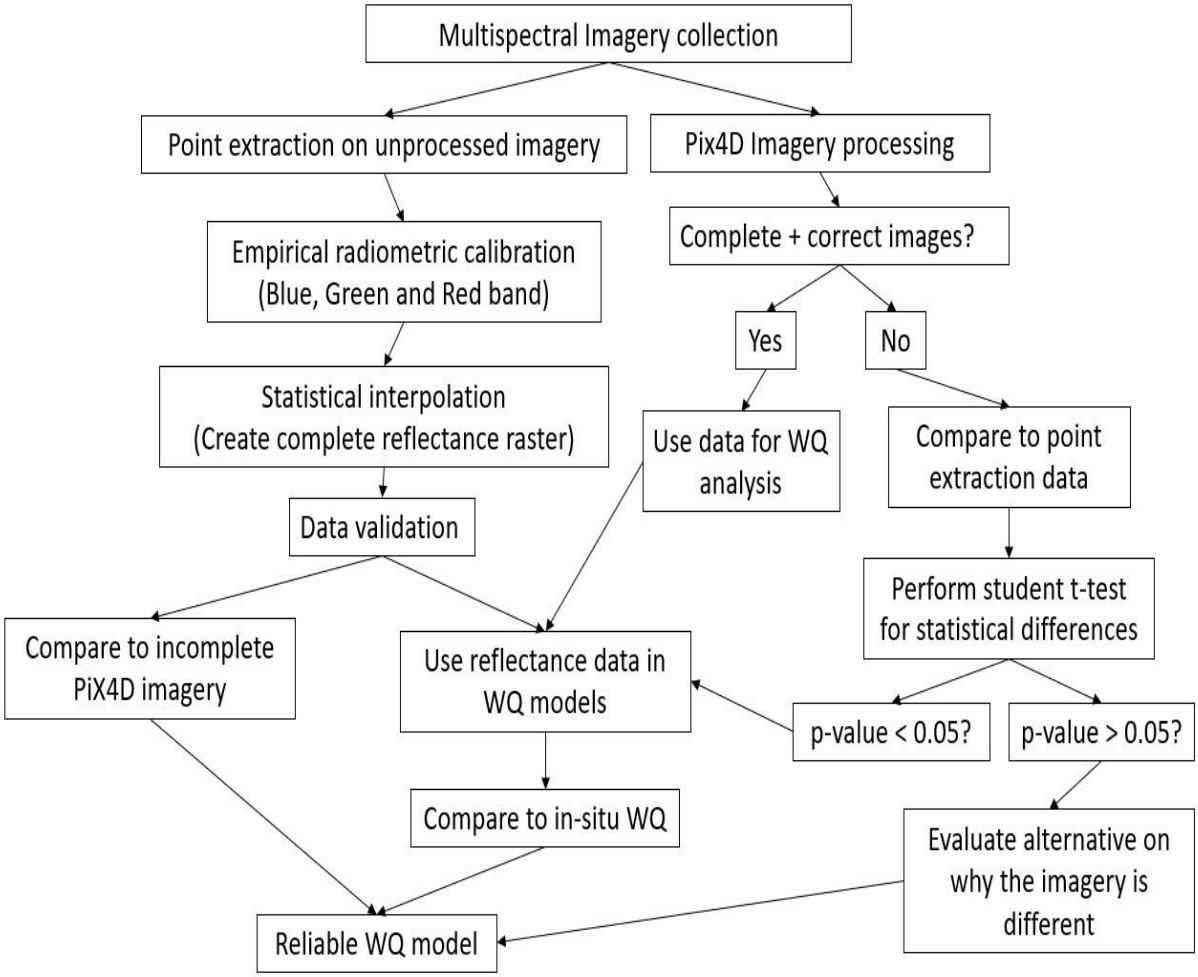

Figure 4.1. Multispectral imagery postprocessing protocol

4.2.1. Study Site

The area of interest for this project was the Horse Creek Arm of Grand Lake O' the Cherokees (Grand Lake), Oklahoma, USA (Figure 4.2.). Located in the northeast part of the state (36.619° N and 94.8415° W), Grand Lake is a multiuse reservoir with beneficial uses

including public and private water supply, warm water aquatic community, agriculture, municipal and industrial uses, hydroelectric power generation, primary body contact recreation, and aesthetics (OWRB, 2005). The Grand Lake watershed encompasses over 26000 km^2 and includes portions of Arkansas, Kansas, Missouri, and Oklahoma. The land use in the watershed is "diverse and complex" (GLWAF, 2008). According to the National Land Cover Database (NLCD), the land usage inside the watershed is mainly planted pasture (36%), followed by natural grass (21%), cropland (20%), forest (14%), low- and high-density development (6%) and open waters (3%).

In recent years, and likely due to the increase of specific land use activities in the watershed, the quality of inflow waters, mainly from the Neosho, Spring and Elk Rivers, has been negatively impacted, thus impacting overall water quality of Grand Lake (OSE, 2004; GLWAF, 2008; Morrison et al., 2017). Since 2011, the Grand River Dam Authority (GRDA), an agency of the state of Oklahoma in charge of monitoring and managing Grand Lake, has been forced to issue blue-green algae (BGA) advisories for some parts of the lake during the summer months (GRDA, 2017).

Regular, traditional in-situ monitoring conducted by staff from the GRDA Ecosystems and Education Center (EEC) has determined that activities near the reservoir are dramatically affecting water quality, especially nutrient concentrations (GRDA, 2017b). Data obtained by EEC personnel have identified that most of the recent BGA blooms began in the Horse Creek Arm of the lake, the study area for this paper.

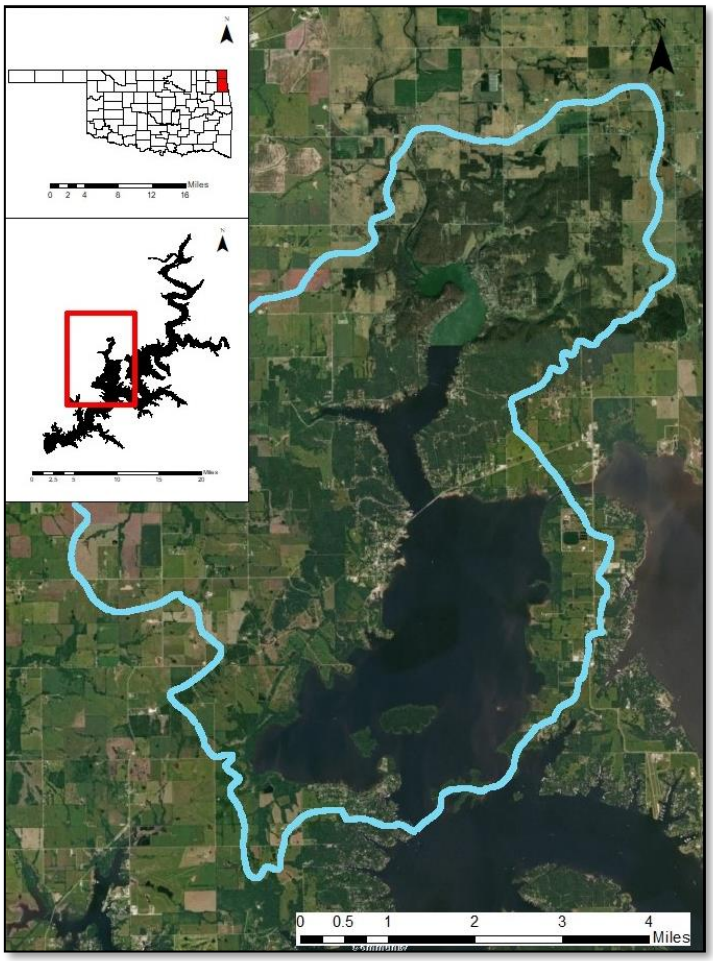

Figure 4.2. Grand Lake O' the Cherokees – Lower Horse Creek Sub-Watershed Boundaries (Blue) (12-digit HUC) – Ottawa and Delaware Counties, Oklahoma

4.2.2. Water Quality and Imagery Collection

Twelve water samples were collected in the Horse Creek Arm during two sampling events. At each sampling location, a Secchi Disk Depth (SDD) reading was taken. One water sample was collected using an alpha bottle submerged 0.5 meters from the water's surface. Once collected, the sample was divided into five portions. The first portion was transferred to a 250-mL high-density polyethylene (HDPE) bottle for field turbidity analysis. The second portion was transferred to another 250-mL HDPE bottle to be analyzed for total nitrogen (TN) and total phosphorus (TP). The third portion was transferred to a 1-L dark bottle to be analyzed for chlorophyll-a (Chl-a). The fourth portion was transferred to a 250-mL HDPE bottle to be analyzed for ammonia nitrogen (NH_3-N). Finally, the remaining portion of the

sample was transferred to a 1-L bottle to be analyzed for total suspended solids (TSS). Once the discrete samples were generated, a YSI 600 multiparameter datasonde was used to measure in-situ dissolved oxygen (DO), temperature, conductivity, salinity, Chl-a and pH values at each location. All samples were collected and preserved according to procedures from the U.S. Environmental Protection Agency (EPA) (USEPA, 2002)

Multispectral imagery was collected using an ATI AgBot sUAS (Figure 4.3a) equipped with a MicaSense RedEdge multispectral sensor (Figure 4.3b). The ATI Agbot, is a vertical takeoff and landing (VTOL) quadcopter, made of carbon fiber. Onboard, the sUAS carries two 6S 6500 mAh lithium polymer (LiPo) batteries, a compass module, one Ublox GPS and the RedEdge multispectral sensor. The MicaSense RedEdge multispectral sensor has the capability of capturing data in the blue (0.475 µm), green (0.560 µm), red (0.668 µm), red edge (0.717 µm) and near infrared (0.840 µm) portions of the spectrum. With respect to the platform, the multispectral sensor is fixed to the bottom via a gimbal. The two-axis gimbal positions the sensor, so imagery is always collected with respect to nadir.

a b

Figure 4.3. Small Unoccupied Aerial System (a) and MicaSense RedEdge multispectral sensor (b)

Missions were flown at an altitude of 100 m AGL with a flying speed of 5 m/sec, and estimated flight time of 10 min. A total of 267 images per band with ground resolution of 6.82 cm were obtained. Figure 4.4 presents the flight path for imagery collection using

Mission Planner (version 1.3.37). Multispectral imagery was acquired within 2 hours of the in-situ water sampling.

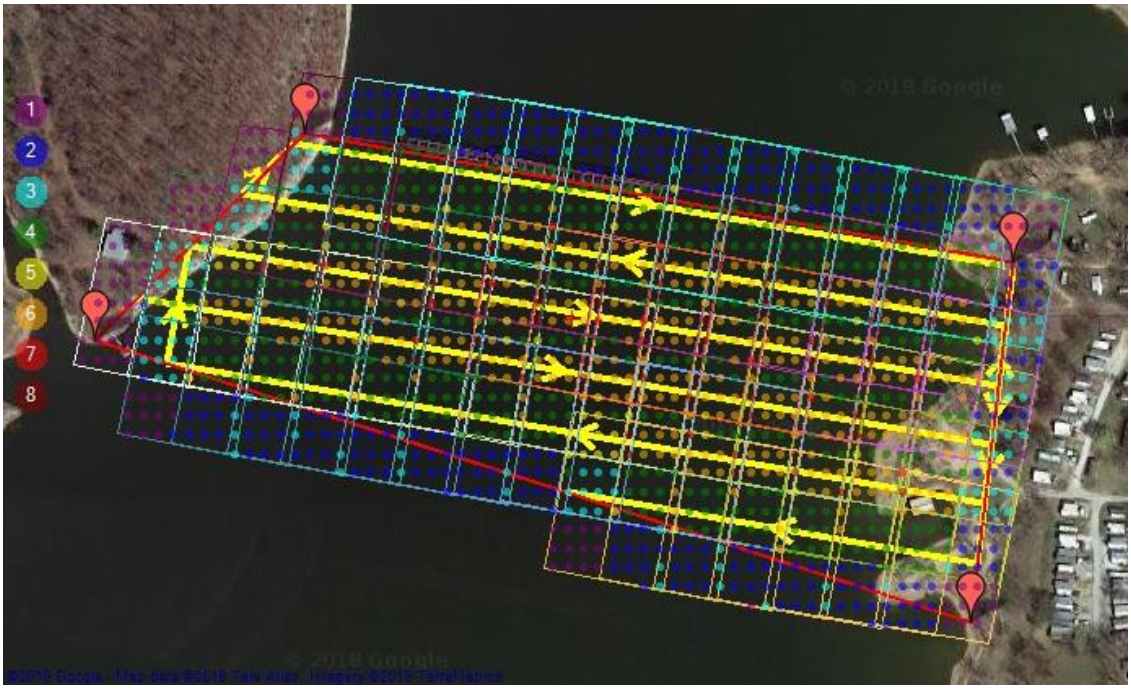

Figure 4.4. sUAS flight path (yellow arrows) and images footprint (with number of overlapping pictures) - Horse Creek

4.2.3. Image Processing

As specified by the manufacturer, the MicaSense RedEdge multispectral sensor has the capability of georeferencing each image. However, georeferencing only takes place at the true centroid of each image. Due to this limitation and the lack of GCPs, it was necessary to calculate the "missing" coordinates of each image to have a partially georeferenced overlap image.

To calculate the image coordinates, it was necessary to estimate the image width and length, using the Vertical Field of View (VFOV) and Horizontal Field of View (HFOV) metrics of the sensor, respectively. MicaSense stipulates that the HFOV and the VFOV are fixed

nominal values that must be considered in order to properly calculate the vertical and horizontal dimensions of an image.

Once the image length and width were calculated, the "missing" coordinates of the image were obtained. All the calculations used the Universal Transverse Mercator (UTM) coordinate system, and, due to the information captured by the sensor, centroid coordinates were known. Inertial Measurement Units (IMU) recorded by the sensor were not used for this process, given that the centroids of each picture were properly geolocated by the onboard GPS.

4.2.4. Reflectance Extraction

A value to point extraction procedure using the GPS location of each centroid was performed using the statistical computing software R (R Core Team, 2017). After extraction, an empirical linear calibration model for each band was used in order to radiometrically correct the extracted values (Wang and Myint, 2015). The empirical calibration equations (Figure 4.5) were developed using a linear regression approach, with the reflectance values (for each individual band) of the black (0% reflectance), grey (70% reflectance) and white (100% reflectance) colors from the MicaSense calibrated reflectance panel for RedEdge data. Calibrated reflectance panel pictures were taken on-site before and after the mission, in order to account for changes in light conditions during the duration of the flight. For the entire length of the flight (10 min), light conditions were assumed to be constant due to the minuscule change in solar position reported by National Oceanic and Atmospheric Administration (NOAA) (NOAA ESRL, 2019).

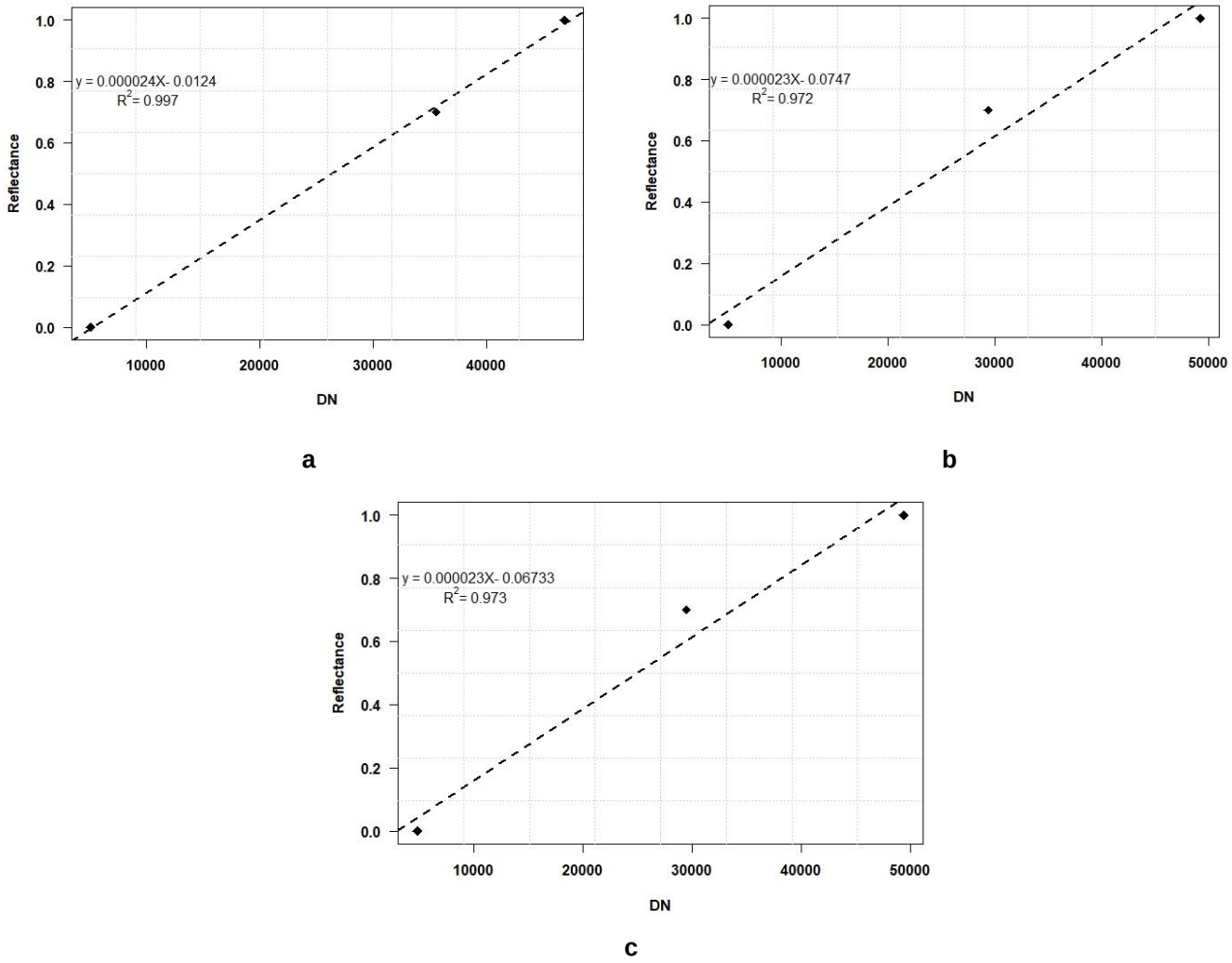

Figure 4.5. Empirical linear calibration models for the blue (a), green (b) and red (c) bands

4.2.3. Statistical Interpolation

The corrected radiometric values then were used to create full reflectance rasters for each band in the visible portion of the electromagnetic spectrum (blue, green, and red). These rasters were developed using Local Polynomial Interpolation (LPI) in ArcMap v10.6.1. LPI is considered an inexact deterministic method of interpolation. Inexact deterministic interpolation makes predictions based on the measured values in defined overlapping neighborhoods. The model fits a user-defined order polynomial (e.g., zero, first, second, etc.) using only points within the defined neighborhoods. The predicted values will differ slightly from the measured values but produces a smoother (real-world) surface. The highest accuracy of LPI is achieved when the measured sample points are taken on a grid (Figure 4.6) and

when the measured data exhibits normal distribution. In addition, LPI provides a measure of model reliability in the form of a critical spatial condition number threshold value (ESRI, 2019). These values are generated by the model to determine how sensitive a predicted value is to minute changes to the coefficients in the linear prediction equations. Values that are similar or equal to the threshold value should be examined and applied with extreme care; values that are greater than the threshold value should not be used because they are unreliable. Each predicted pixel is assigned a value that is then averaged for the entire surface. For first-order polynomial models, the surface's threshold value should not exceed ten (ESRI, 2019).

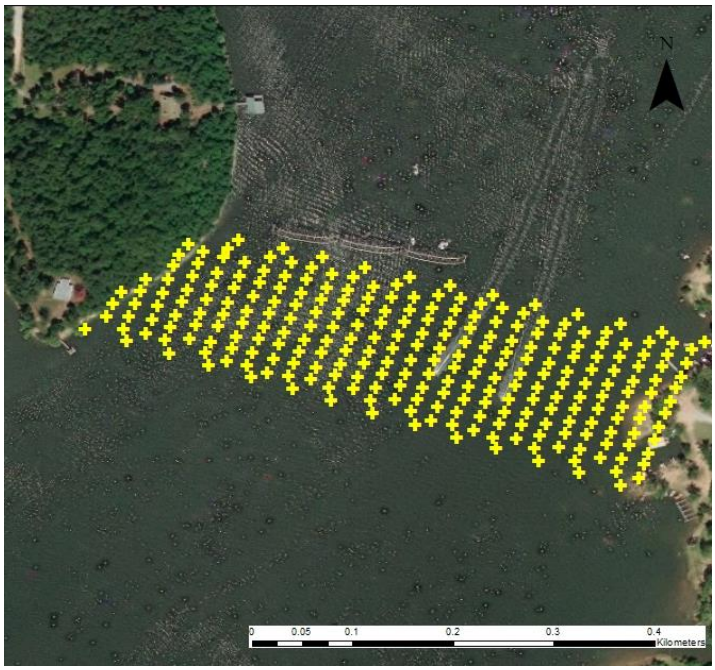

Figure 4.6. Centroid coordinates used for Kriging

To maintain the original spatial resolution of the sUAS-derived reflectance raster, an output cell size of 6.82 cm was utilized. In order to minimize model complexity and ensure the model was not overfitting the data, a first-order polynomial was selected. The circular neighborhoods used to identify which surrounding points will be used to control the predicted output had radii of approximately 68.15 meters, and a smoothing factor of 0.25. To

understand the reliability of the model (i.e., the predicted values) a critical spatial condition number threshold value of ten was selected (ESRI, 2019).

4.2.4. Validation

Available proprietary and open-source software fail to generate fully orthorectified images taken over large bodies of water. However, if a portion of the image is terrestrial (i.e., containing GCPs), the software generates incomplete orthorectified images. Figure 4.7 shows an incomplete image generated by Pix4D of a mission flown for this study.

In order to validate the data generated in the above steps, the reflectance values at the centroids of the pixels located wholly in water (i.e., with no land coverage and therefore no GCPs) were extracted from the incomplete images from Pix4D. These values were compared to the values generated from the above methodology. In order to determine if the generated values had the capability of predicting water quality variables (i.e., TSS, SDD and Chl-a), equations developed in previous studies (Kloiber et al., 2002; Allan et al., 2011; Shahzard et al., 2018) were used to generate modeled water quality data. These modeled data were statistically compared with in-situ data collected during the mission.

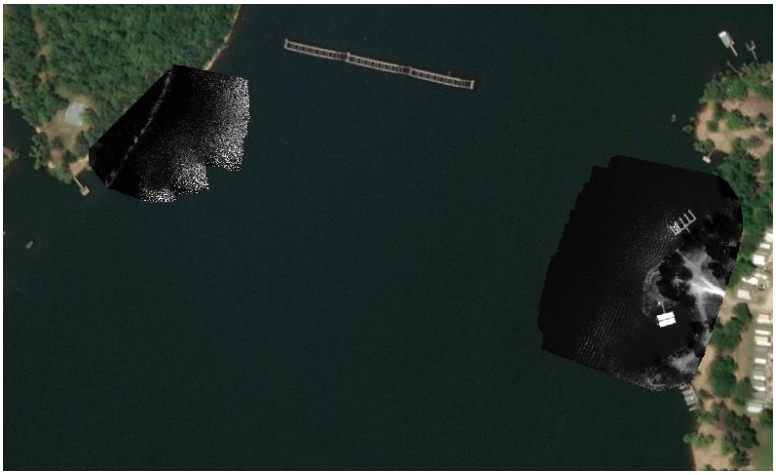

Figure 4.7. Incomplete Image generated by Pix4D – Horse Creek, Grand Lake O' the Cherokees

4.3. Results

4.3.1. Image processing

Figure 4.8 presents the generated complete image of the mission flown in this study, corresponding to the blue band. The image processing protocol was successful in positioning each individual image in its correct relative position. However, the protocol failed to consider the orientation of the image with respect to the location of the camera at the time the picture was taken. Because all statistical work was completed using the coordinates of the centroids of each image, orientation with respect to true north was not relevant.

Figure 4.8. Georeferenced images over Horse Creek, Grand Lake O' the Cherokees (blue band).

4.3.2. Statistical Interpolation

The LPI surfaces were generated using the corrected extracted values for the blue, green, and red bands, with no statistical outliers, in order to fit the best model in the variogram. Statistical outliers were attributed to those centroids that were affected by sun glint effects (Figure 4.8). These points were removed, given that imagery with sun glint effects can lead to errors (30% or more) when used to determine water quality (Kay et al., 2009). The results of this interpolation were determined to be reliable and accurate based on an evaluation of spatial

error. The mean critical spatial condition threshold values for the interpolated blue (Figure 4.9a), green (Figure 4.9b), and red (Figure 4.9c) surfaces were 9.86, 3.93, and 4.69, respectively. The increased threshold value for the blue band is attributed to unstable, yet acceptable, predictions in the northeast portion of the study area likely caused by the increased distance to the nearest neighbors. Furthermore, the unfilled locations within the study area were determined to be unstable (threshold value > 10) and therefore were not included in the final output. Once the surfaces were generated, a point extraction using the GPS locations of the in-situ sampling locations was performed on all interpolated surfaces in order to obtain the reflectance values at each location, for each band. These values were used in the validation process.

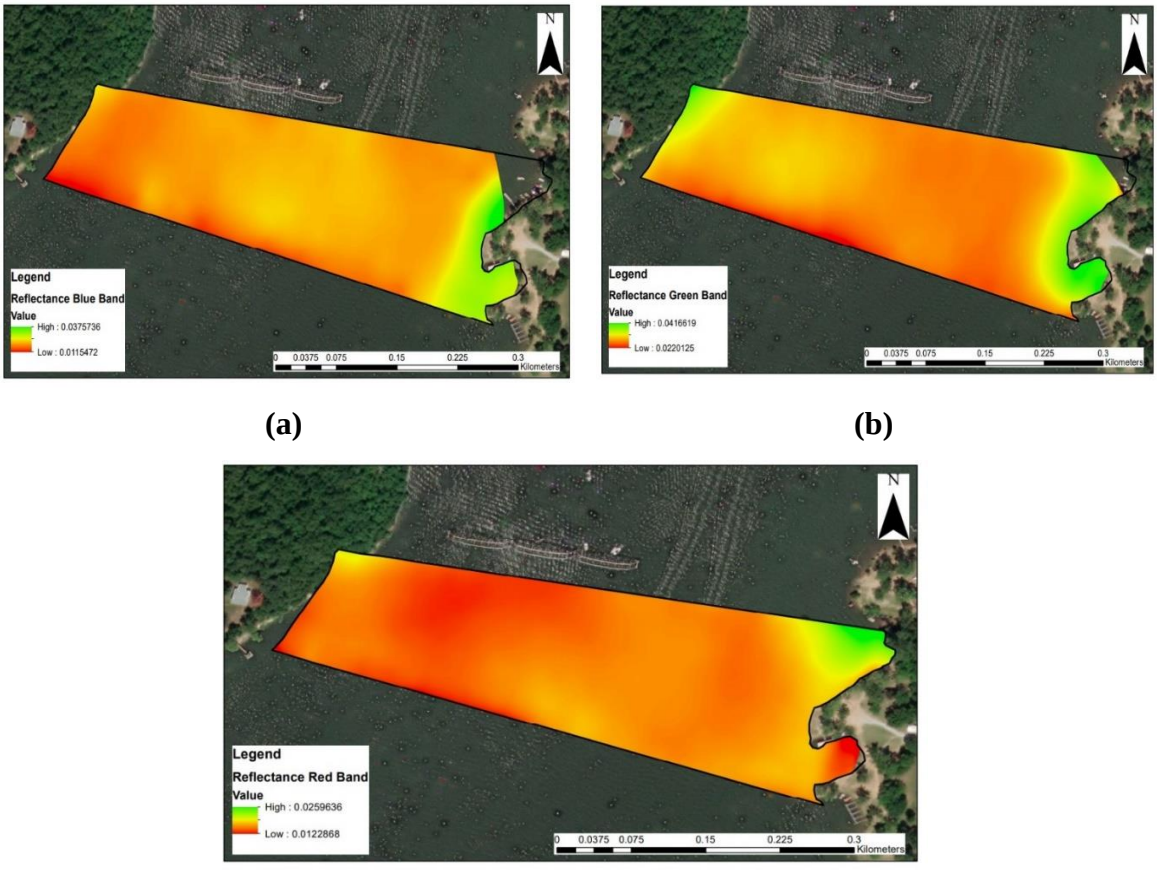

Figure 4.9. Geolocated and radiometrically corrected true reflectance surfaces, local polynomial interpolation result – Blue (a), Green (b) and Red (c) bands

4.3.3. Validation

The first step in the validation process was to compare the extracted values from the incomplete Pix4D (Figure 4.7) images to the generated values from the kriged surfaces (Figure 4.9). These comparisons showed that the kriged surfaces values were statistically different, although on the same order of magnitude for all three bands.

The second step of the validation process was to determine how well the point extracted values predicted water quality parameters. The approach utilized the equations presented in Table 4.1. These equations were obtained from different studies that used linear regression approaches to develop mathematical relationships capable of statistically determining optical water quality parameters from Landsat 7 images. Landsat 7 images were used for validation because the visible wavelengths of the sensor used in this study resemble those in Landsat 7. Due to the difference in scale ("actual" > "predicted" by an order or magnitude) all measurements were normalized by their respective mean. Statistical comparisons between the normalized predicted and actual measurements were performed for each water quality parameter, using a paired Student's t-test; all p-values for these comparisons were above 0.05, showing that there is no statistical difference between these two datasets.

Table 4.1. Regression equations to predict water quality parameters

Water Quality Parameter	***Equation***	***Reference***
TSS	$TSS = \beta*TM3 + \rho$	Shahzard et al., 2018
SDD	$Ln(SDD) = \beta*(TM1/TM3) + \rho*TM1$	Kloiber et al., 2002
Chl-a	$Ln(Chl\text{-}a) = \beta*Ln(TM3) + \rho$	Allan et al., 2011

*ρ and β are estimated coefficients fitting the regression analysis

4.4. Discussion

The protocol developed in this study produced complete geolocated and radiometrically corrected true reflectance surfaces for the visible portion of the electromagnetic spectrum

over a large body of water using statistical interpolation of images taken with a multispectral sensor onboard a sUAS. These generated surfaces were then used to determine optical water quality parameters (TSS, SDD and Chl-a). Two factors that played important roles in producing these reflectance surfaces are the radiometric calibration methods and the predictive models developed by other researchers that were not developed for this area of research.

For this study, radiometric calibration was performed by deriving empirical models based on measurements of a calibrated reflectance panel. Wang and Myint (2015) determined that this simplified method had the ability to derive linear equations ($R^2 \geq 0.90$) capable of radiometrically calibrating multispectral imagery taken with sUAS. By following this approach, true reflectance values were obtained. However, when the empirically derived values were compared to the corrected reflectance values from the incomplete Pix4D images, the values were statistically different (p-value ≤ 0.05). Due to restricted proprietary information, it is not possible to determine the difference between the radiometric calibration methods used by Pix4D and the simplified empirical calibration method.

The second factor to consider is the application of predictive models that were not developed for this particular area of research. Different authors have determined that relationships between optical water quality parameters and reflectance values from remote sensing platforms can be obtained using different linear regression approaches (Kloiber et al., 2002; Allan et al., 2011; Shahzard et al., 2018). However, Kloiber et al. (2002) points out that these predictive models must be developed for each area of interest, given that external environmental factors particular to each region could influence the slope of these empirical models. Therefore, it is important to note that even though the water quality data generated from reflectance surfaces in this study are not statistically different from the collected in-situ

data, the predicted values fail to accurately track the in-situ measurements. As mentioned previously, one of the most probable reasons for this is that the models used in this validation were not developed for this particular area of research. Despite this shortcoming, it is important to note that all measured concentrations in this study fall in range of those concentrations measured by the Kloiber et al., (2002), Allan et al., (2011) and Shahzard et al., (2018).

Finally, it is also important to note that all of the optical water quality models used above were developed from imagery obtained from a Landsat 7 measurements. Even though the visible wavelengths of the sensor used in this study resemble those in Landsat 7, the question of comparability of these two remote sensing platforms (i.e., satellites and sUAS) arises, especially as it relates to different spatial resolutions between these two platforms.

4.5. Conclusion

This study aimed to develop a protocol to address current limitations when stitching sUAS images obtained over large bodies of water without any GCPs. The objective was to produce a true reflectance surface from which values could be extracted and used in order to estimate optical water quality parameters based on statistical models. From the results herein, it can be concluded that: (1) the created protocol successfully generates complete geolocated and radiometrically corrected true reflectance surfaces for large bodies of waters, (2) optical water quality parameters can be estimated from the created true reflectance surfaces using linear approaches and (3) further studies are needed to determine the difference between models developed from satellite imagery versus images taken from a sUAS.

References

Agisoft LLC. 2019. Fully automated professional photogrammetric kit. [Online]. [Accessed August 29, 2019]. Available from: https://www.agisoft.com/pdf/photoscan_presentation.pdf

Allan, M.G., Hamilton, D.P., Hicks, B.J. and Brabyn, L. Landsat remote sensing of chlorophyll a concentrations in central North Island lakes of New Zealand. International Journal of Remote Sensing, 2011, 32(7), pp. 2037-2055.

Anderson, D., Gilbert, P.M. and Burkholder, J.M. Harmful algal blooms and eutrophication: Nutrient sources, composition, and consequences. Estuaries and Coasts, 2002, 25(4), pp. 704-726.

Colomina, I. and Molina, P. Unmanned aerial systems for photogrammetry and remote sensing: A review. ISPRS Journal of Photogrammetry and Remote Sensing, 2014, 92, pp. 79-97.

Doughty, C. and Cavanaugh, K. Mapping coastal wetlands biomass from high resolution unmanned aerial vehicle (UAV) Imagery. Remote Sensing, 2019, 11(5), pp. 540-556.

Eisenbeiss, H. 2004. A mini–Unmanned Aerial Vehicles (UAVs): system overview and image acquisition. International Archives of Photogrammetry, Remote Sensing and Spatial Information Sciences, International Workshop on Processing and Visualization Using High Resolution Imagery, Pitsanulok, Thailand.

Environmental Services Research Institute (ESRI). Deterministic Methods for Spatial Interpolation. [Online]. [Accessed February 21, 2020]. Available from: https://desktop.arcgis.com/en/arcmap/10.6/extensions/geostatistical-analyst/deterministic-methods-for-spatial-interpolation.htm

Fraichard, T. Trajectory planning in a dynamic workspace: a 'state-time space' approach. Advanced Robotics, 1998, 13(1), pp. 75-94.

Grand Lake Watershed Alliance Foundation. 2008. Grand Lake Watershed Plan: For Improving Water Quality Throughout the Grand Lake Watershed. Groove, OK. Grand Lake O' the Cherokees Watershed Alliance Foundation Inc.

Grand River Dam Authority. 2017. GRDA expanding blue green algae advisory. [Online]. [Accessed February 1, 2018]. Available from http://www.grda.com/grda-expanding-blue-green-algae-advisory/

Grand River Dam Authority. 2017b. Water Quality Grand Lake. [Online]. [Accessed February 1, 2018]. Available from http://www.grda.com/grda-installs-new-water-quality-monitoring-equipment-on-grand-hudson/

Kardoulas, N.G., Bird, A.C. and Lawan, A.I. Geometric correction of spot and landsat imagery: A comparison of map and GPS-derived control points. Photogrammetric Engineering & Remote Sensing, 1996, 62(10), pp. 1173-1177.

Kay, S., Hedley, J.D. and Lavander, S. Sun glint correction of high and low spatial resolution images of aquatic scenes: a review of methods for visible and near-infrared wavelengths. Remote Sensing, 2009, 1(4), pp. 697-730.

Kloiber, S.M., Brezonik, P.L., Olmanson, L.G. and Bauer M.V. A procedure for regional lake water clarity assessment using Landsat multispectral data. Remote Sensing of Environment, 2002, 82(1), pp. 38-47.

Laliberte, A.S., Goforth, M.A., Steele, C.M. and Rango, A. Multispectral remote sensing from unmanned aircraft: Image processing workflows and applications for rangeland environments. Remote Sensing, 2011, (11), pp. 2529-2551

Li, W., Niu, Z., Chen, H., Li, D., Wu, M., and Zhao W. Remote estimation of canopy height and aboveground biomass of maize using high-resolution stereo images from a low-cost unmanned aerial vehicle system. Ecological Indicators, 2016, 67, pp. 637-648.

Li, W., Sun, K., and Bai, T. Algorithm for automatic image dodging of unmanned aerial vehicle images using two-dimensional radiometric spatial attributes. Journal of Applied Remote Sensing, 2016, 10(3), pp. 23-36.

Louhaichi, M., Petersen, S., Gomez, T., Jensen, R.R., Morgan, G.R., and Butterfield, C. Remote Spectral Imaging Using a Low Cost sUAV System for Monitoring Rangelands. Advances in Remote Sensing and Geo Informatics Applications, 2018, 1, pp. 143-145.

Melville, B., Fisher, A. and Lucieer, A. Ultra-high spatial resolution fractional vegetation cover from unmanned aerial multispectral imagery. International Journal of Applied Earth Observation and Geoinformation, 2019, 78, pp. 14-24.

Morrison, J.M., Bajer, K.D., Zamor, R.M., Nikolai, S., Elshahed, M.S. and Youssef, N.H. Spatiotemporal analysis of microbial community dynamics during seasonal stratification events in a freshwater lake (Grand Lake, OK, USA). PLoS ONE, 2017, 12(5), e0177488.

National Oceanic and Atmospheric Administration Earth System Research Laboratory. [Online]. [Accessed August 29, 2019]. Available from: https://www.esrl.noaa.gov/gmd/grad/solcalc/azel.html

Nebiker, S., Lack, N. and Abacherli, M. Light-weight multispectral UAV sensors and their capabilities for predicting grain yield and detecting plant diseases. International Archives of the Photogrammetry, Remote Sensing and Spatial Information Sciences, 2016, XLI-B1, pp. 963-970.

Nex, F. and Remondino, F. UAV for #D mapping applications: a review. Applied Geomatics, 2014, 6(1), pp. 1-5.

Office of the Secretary of the Environment. 2014. Comprehensive study of the Grand Lake watershed: Initial report office of the secretary of the environment. Oklahoma City, OK. [Online]. [Accessed August 29, 2019]. Available from: https://www.fws.gov/southwest/es/Oklahoma/Documents/Contaminants/FinalforLake.pdf

Oklahoma Water Resources Board. 2005. Grand Watershed Planning Region Report. Edition 1. Oklahoma: Oklahoma Water Resources Board.

Papoutsa, C., Retalis, A., Toulios, L. and Hadjimitsis, D.G. Defining the Landsat TM/ETM+ and CHRIS/PROBA spectral regions in which turbidity can be retrieved in inland waterbodies using field spectroscopy. International Journal of Remote Sensing, 2014, 35(5), pp. 1674-1692.

Perez, D., Maza, I., Caballero, F., Scarlatti, D., Casado, E. and Ollero, A. A ground control station for a multi-UAV surveillance system. Journal of Intelligent & Robotic Systems, 2013, 69(1), pp. 119-130.

Pix4D. 2019. Selecting the Image Acquisition Plan Type. [Online]. [Accessed August 29, 2019]. Available from: https://support.pix4d.com/hc/en-us/articles/202557459-Step-1-

Before-Starting-a-Project-1-Designing-the-Image-Acquisition-Plan-a-Selecting-the-Image-Acquisition-Plan-Type

Rusnak, M., Sladek, J., Kidova, A., and Lehotsky, M. Template for high-resolution river landscape mapping using UAV technology. Measurement, 2018, 115, pp. 139-151.

Shahzad, M.I., Meraj, M., Nazeer, M., Zia, I., Inam, A., Mehmood, K., and Zafar, H. Empirical estimation of suspended solids concentration in the Indus Delta Region using Landsat-7 ETM+ imagery. Journal of Environmental Management, 2018, 29, pp. 254-261.

Shi, Z. and Ng, W. A collision-free path planning algorithm for unmanned aerial vehicle delivery. International Conference on Unmanned Aircraft Systems (ICUAS), 2018, Dallas, TX, USA.

Toutin, T. Geometric processing of remote sensing images: models, algorithms and methods. International Journal of Remote Sensing, 2004, 20(10), pp. 1893-1924.

Tulum, K., Durak, U. and Ider, S.K. Situation aware UAV mission route planning. IEEE Aerospace conference, 2009, Big Sky, MT, USA.

United States Environmental Protection Agency. 2002. Methods for chemical analysis of waters and waste waters. U.S. Environmental Protection Agency, Washington, D.C., EPA/600/4-79/020 (NTIS PB84128677).

Valero-Gomez, A. and Gomez, J. Fast Marching Methods in Path Planning. IEEE Robotics & Automation Magazine, 2013, 20(4), pp. 111-120.

Wang, C. and Myint, S. A Simplified Empirical Line Calibration Method for sUAS-based Remote Sensing. Journal of Selected Topics in Applied Earth Observations and Remote Sensing, 2015, 8(5), pp. 1876-1885.

Xiang, H. and Tian, L. Method for automatic georeferencing aerial remote sensing (RS) images from an unmanned aerial vehicle (UAV) platform. Biosystems Engineering, 2011, 108(2), pp. 104-113.

Zhang, C. and Kovacs, J.M. The application of small unmanned aerial systems for precision agriculture: a review. Precision Agriculture, 2012, 13 (6), pp. 693-712.

CHAPTER 5 – Land Use/Land Cover Impacts on Water Quality Inside the Upper Horse Creek watershed – Understanding the Past in Order to Act in the Future

Abstract: Land use/land cover (LULC) influences the water quality of a watershed. Understanding the relationships between the activities that take place within a watershed and its water quality has become a must when it comes to comprehensively addressing water quality concerns. More importantly, understanding these complex relationships provides knowledge that helps to properly design and implement restoration strategies that aim to improve water quality. As part of a larger long-term study, a series of riparian conservation easements have been implemented on Horse Creek and its tributaries to improve water quality. Horse Creek directly discharges into Grand Lake o' the Cherokees, Oklahoma, which has been the site of several harmful algae blooms (HABs). The purposes of this study were to: (1) determine the relationship between land use patterns and historical and present water quality, (2) estimate nutrient loads that are being discharged by Horse Creek and Little Horse Creek, (3) capture the current status of the riparian conservation easements and (4) provide initial baseline data to document potential changes in water quality as a result of the implementation of the riparian conservation areas. Results indicate that: (1) Water quality in HC and LHC has been relatively stable for the past two decades, (2) LULC inside the Upper Horse Creek watershed has seen minimal changes, (3) the watershed is dominated by pasture/hay (62%) and cultivated crops (28%), (4) based on the redundancy analysis, historical water quality for Horse Creek and Little Horse Creek has been influenced by pasture/hay and cultivated crops land use/land cover and (5) a source of elevated nutrient concentrations may be attributed to nonpoint source pollution from actively managing pasture/hay and agricultural land.

Keywords: land use land cover, water quality, nutrients, agriculture.

5.1. Introduction

Driven by the urge of obtaining and exploiting natural resources to satisfy agricultural, industrial, and commercial needs and practices, humans have been responsible for the most drastic changes on the planet's land cover (LC, e.g., "the observed biophysical cover on the Earth's surface", FAO, 2020) and land use (LU, e.g., purposes given by humans for the land, NOA, 2020). As a direct result of these land use/land cover (LULC) changes, there have been measurable alterations in global and regional climate patterns (Stohlgren et al., 1998; Stone, 2005; Boysen et al., 2014), degradation/destruction of both aquatic and terrestrial ecosystems (Salazar et al., 2015; Nobre et al., 2016), changes in geomorphologic and ecological processes (Vitousek, 1994; Foley et al., 2005; Abe and Driscoll, 2012), transformation of the hydrological cycle (Gordon et al., 2015; Poff et al., 2006; Pokhrel et al., 2017) and introduction of anthropogenic nutrient inputs into rivers, lakes, and streams (Hale et al., 2015; Alverez et al., 2017; Giacomazzo et al., 2020).

The relationships between land use type and water quality have been widely recognized by different researchers (Lenat, 1994; Wang, 2001; Ren et al., 2003; Goonetilleke, et al., 2005; Carle et al., 2005; Galbraith and Burns, 2007; Tran et al., 2010; Brion et al., 2011; Haidary et al., 2013; Bu et al., 2014; Wilson, 2015; Dai et al., 2017). The United States Environmental Protection Agency (EPA) has identified that the two primary areas of concern are land development and agricultural use, due to the wide variety of potentially harmful environmental effects that include (but are not restricted to): (1) contributions of non-point source (NPS) water pollution, (2) increased soil erosion due to changes in water quantity, (3) loss of native habitats, (4) spread of invasive species and (5) transport of residential (e.g., soil, oil, or toxic compounds) and agricultural (e.g., soil, pesticides and fertilizers) pollutants

via runoff into bodies of water. Giri and Qiu (2016), in their paper "*Understanding the relationship of land uses and water quality in Twenty First Century: A review*" referenced that within a watershed, land use changes are one component that has a vital role in degrading water quality, not only due to the presence of point sources, but, also due to NPS.

NPS pollution can be described as a function of climatic factors (e.g., rainfall) and site-specific land uses (Corbett et al., 1997; Leon et al., 2001; Sheng et al., 2012; Wu et al., 2012; Fraga et al., 2016; Yoon et al., 2016; Wang et al., 2018). When precipitation occurs, the produced surface runoff transports excess constituents on the ground surface (products of land use practices (e.g., fertilizers, oil, dust, pesticides, animal feces) and naturally occurring substances) across the landscape, to finally discharge into the nearest body of water contributing major pollutant loadings (Glandon et al., 1981; Anbumozhi et al., 2005). As a direct result of this pollutant loading, water quality is degraded, affecting not only ecosystems, but potentially also human health (Chen and Wu, 2018; Chen et al., 2019). On a global scale, and as Krauskopf and Loague (2003) mention, "30-50% of all surface and subsurface water resources are impacted by NPS".

Due to its high variability and diffuse nature, the identification of NPS pollution sources has proven to be a challenging task (EPA, 1999; Munafo et al., 2005; Dowd et al., 2008; EPA, 2016; Lui et al., 2016). In recent decades and due to the growing concerns of increasing water quality degradation and water scarcity, efforts have focused on (1) decreasing/treating excess nutrients on landscapes and (2) identifying the most probable sources of NPS pollution (Basnyat et al., 2000; Baker et al., 2001; Matejicek et al., 2003; Giri and Qiu, 2016).

From the perspective of decreasing/treating excess nutrients on landscapes, the implementation of best management practices (BMPs) has proven useful to address water quality (e.g., decreased dissolved and particulate pollutant concentrations and loads) and

quantity (e.g., reduction of peak discharge and total storm volume during runoff) issues (Aust and Blinn, 2004; Hunt et al., 2006; Ahiablme et al., 2012; Ice, 2014; Liu et al., 2017; Cristan et al., 2018). The general concept is the adoption and implementation of structural BMPs (on-ground interventions) or non-structural BMPs (education leading to changes in practice) that avoid, control, trap or treat the discharge of pollutants into receiving waters (Roesner et al., 2001; Sharpley et al., 2006). Some of the most common structural BMPs are conservation cover, conservation crop rotation, contour farming, nutrient management, drainage water management, culvert sizing, grassed waterways, grade stabilization structures at side inlets, wetland restoration, field border, filter strips and riparian forest buffers (MDA, 2017; Liu et al., 2017).

Riparian buffers are "grasses, grass-like, forbs, shrubs, trees or other vegetation growing along streams" (USDA, 2011), that have proven useful to not only reduce the transport of NPS pollutants into a stream (significantly reducing nutrient concentrations from surface runoff), but also, to reduce flood heights and improve stability of streambanks (Osborne and Kovacic, 1993; Lowrance et al., 1997; Snyder et al., 1998; Spruill 2000; Anbumozhi et al., 2005; Li et al., 2009 and Wang et al., 2020). The biological, physical, and geochemical mechanisms that allow riparian buffers to act as nutrient sinks are friction, sediment deposition, filtration, sorption, plant uptake, reduction, oxidation, and immobilization (Hoffmann and Kjaergaard, 2009). Due to the environmental benefits that these areas bring, the Oklahoma Conservation Commission (OCC 1998) in their "*Riparian Area – Management Handbook"* identified that "design or engineered riparian buffers, should consist of three-zones" (Figure 5.1). Table 5.1. presents the design criteria suggested by OCC.

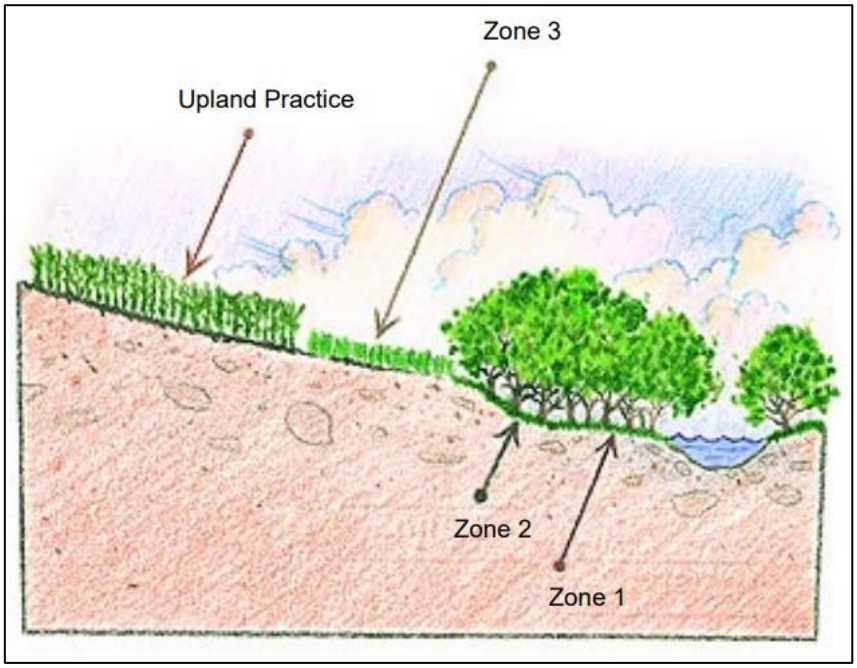

Figure 5.1. Cross sectional view of the three zones riparian buffer design. (OCC, 1998)

Table 5.1. Riparian Buffers suggested design criteria

Zone	Purpose	Vegetation	Minimum Width (m)
1	- Streambank stabilization - Provide shade (lower water temperature) - Provide aquatic habitat	- Native trees - Nonnative short-lived (areas with severely eroded banks)	5
2	- Contact time - Carbon source (for buffering) - Long-term storage for nutrients	- Deciduous trees - Native riparian trees - Forb - Shrub	18
3	- Runoff control - Sediment filtering - Nutrient uptake - Reduction of flow velocity	- Dense perennial grasses - Forbs	6

In terms of identifying the most probable sources of NPS pollution, the implementation and use of geographical information systems (GIS) and satellite remote sensing technologies,

paired with in-situ water quality and quantity measurements, have given researchers the opportunity to focus on the analysis and understanding of the influences of land cover in order to potentially identify NPS pollution sources (Baker et al., 2001; Yang and Liu, 2007; Huang, et al 2013). The general concept of this methodology is the use of different datasets (e.g., land use/landcover maps, digital elevation models (DEM), digital terrain elevation data (DTED), time series in-situ water quality and quantity information, climatological data, among others), paired with statistical and spatial statistical tools/methods, to explain the influence of LULC on water quality (Chen, 2002; Ruiz-Luna and Berlanga-Robles, 2003; Giri and Qiu, 2016).

Understanding that combining these two approaches could be an effective step to decrease nutrient inputs into one of Oklahoma's most iconic human-made bodies of water (Grand Lake o' the Cherokees (Grand Lake)), the Grand River Dam Authority (GRDA, a state agency in charge of managing Grand Lake), in cooperation with OCC and an influential private land owner in the watershed, have implemented a series of riparian conservation easements on a stream that directly discharge its waters into Grand Lake. Since 2011, GRDA has issued blue-green algae (BGA) advisories, promoted by excess nutrients and eutrophication, for some parts of the lake during the summer months (GRDA 2017). Regular monitoring plans have been developed and implemented, and the staff from the GRDA Ecosystems and Education Center (EEC) have hypothesized that activities near the reservoir are dramatically affecting water quality in the lake, especially increases in summer BGA blooms (GRDA, 2017b). Data obtained by the EEC have demonstrated that most of the BGA blooms began in the Horse Creek (HC) arm of the lake. Based on that information, the purpose of this study is to: (1) determine the relationship between land use patterns and historical and present water quality in the Horse Creek watershed, (2) estimate nutrient loads, (3) capture the current status of the riparian conservation easements and (4) provide initial baseline data to evaluate potential

changes in water quality which may result from the implementation of riparian conservation areas.

5.2.Materials and Methods

5.2.1. Study Area

The area of research for this project is the Upper Horse Creek watershed (HUC 12 110702060402), located in the north-east portion of the state of Oklahoma (Figure 5.2). The Upper Horse Creek watershed has an approximate area of 130 km^2 and is drained by two major streams: (1) Horse Creek (HC) and (2) Little Horse Creek (LHC). According to the Oklahoma Water Resources Board (OWRB), HC (WBID OK121600030160_00) is a stream that directly discharges its waters into Grand Lake. The entire longitudinal extents of HC and LHC (WBID OK121600030190_00) are 17.6 and 10.4 river kilometers, respectively. The Oklahoma Department of Environmental Quality (DEQ) identifies HC and LHC as impaired or threatened streams for one or more designated uses by a pollutant (ODEQ, 2020). Results of the latest (2018) integrated water quality report by ODEQ, placed HC and LHC on the 303 (d) list of impaired waters for dissolved oxygen (DO), sulfate (SO_4^{2-}), and *Escherichia coli* (*E. coli*), In addition, LHC is listed for macroinvertebrate bioassessment and enterococcus bacteria (ODEQ, 2020).

In 2018, the first in a series of parcels of land were enrolled in riparian protection efforts (Figure 5.3). These riparian buffers temporarily remove 0.7 km^2 of land around HC from agricultural production.

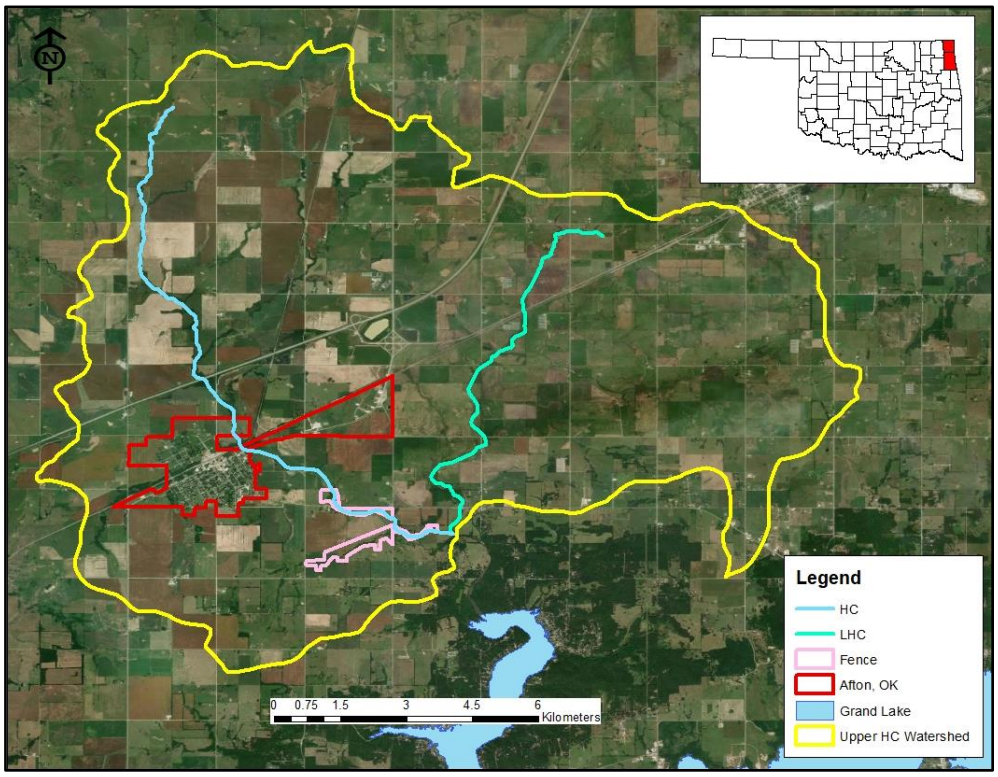

Figure 5.2. Location of the research area with respect to the City of Afton, Oklahoma.

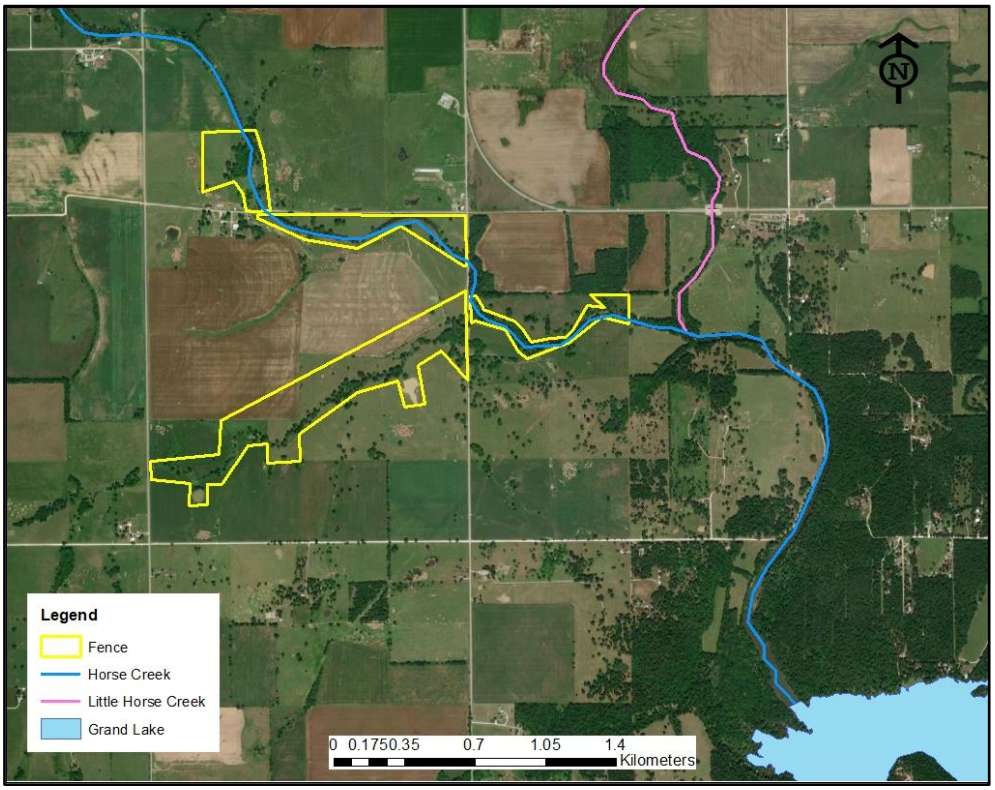

Figure 5.3. Location and extent of the first riparian conservation easements.

5.2.2. Water Quality and Water Quantity

Water quality and quantity data for this study were composed of two datasets. The first dataset was collected by the OCC at LHC and HC (Figure 5.4). For these locations, OCC has recorded water quality and water quantity data since 1999 through 2018, as part of their routine rotating basin monitoring plan for streams in Oklahoma. Table 5.2 presents the analytes and methods used by OCC for water quality analyses. Physical water quality parameters (e.g., conductivity, dissolved oxygen (DO), pH, total dissolved solids (TDS), and temperature) were collected using a YSI ProPlus Multimeter.

The second dataset was collected by the University of Oklahoma (OU) Center for Restoration of Ecosystems and Watersheds (CREW) at LHC and HC (Figure 5.4) as part of this dissertation. For these locations, CREW personnel collected monthly water quality and water quantity data since May 2018 through September 2020 for HC, and since January 2019 through September 2020 for LHC. Table 5.2 presents the analytes and methods used by CREW for water quality analyses. Physical water quality parameters (e.g., conductivity, DO, pH, TDS, salinity, and temperature) were collected using a YSI 600 multiparameter data sonde and 650 MDS controller.

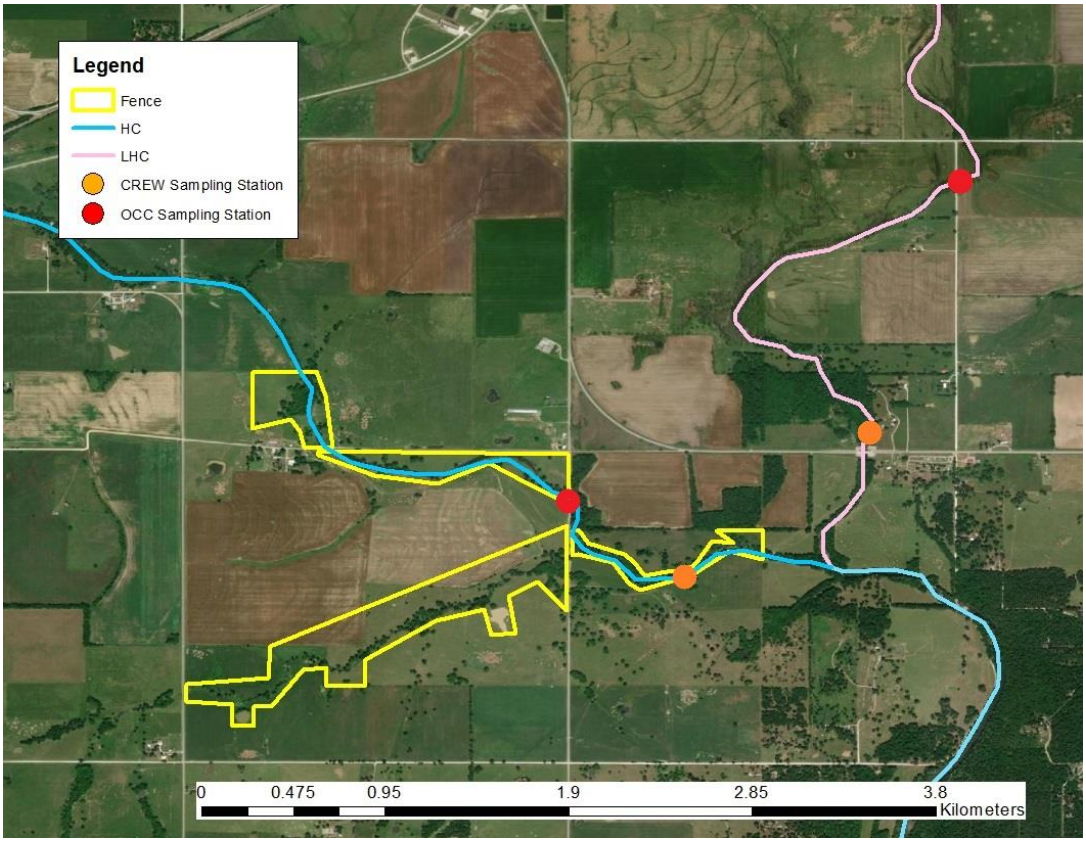

Figure 5.4. Location of sampling points for OCC and CREW at HC and LHC.

Table 5.2. OCC and CREW water quality analytes and methods

Analyte	Method OCC	Method CREW
Total Nitrogen	--	HACH TNT 10071
Ammonia	APHA-4500 – NH_3(H)	HACH TNT 10031
Kjeldahl Nitrogen (TKN)	EPA-351.2	--
Nitrate	EPA-9056	EPA-127-A
Nitrite	EPA-9056	EPA-115-A
Total Phosphorus	AEPA-365.1	--
Ortho Phosphorus	EPA-365.1	EPA-145-A
Chloride	EPA-9056	--
Sulfate	EPA-9056	EPA-165-D
Total Suspended Solids	APHA-2540-D	EPA-160.2
Chlorophyll-a	--	EPA- 445.0

Figure 5.5a presents the frequency of the data collection efforts by OCC at both creeks. As for the data collected by CREW, water quality and water quantity data collection started in

June 2018 (for HC), and January 2019 (for LHC) on a monthly basis (Figure 5.5b), and the last data recorded for this study were collected in September 2020 for both creeks.

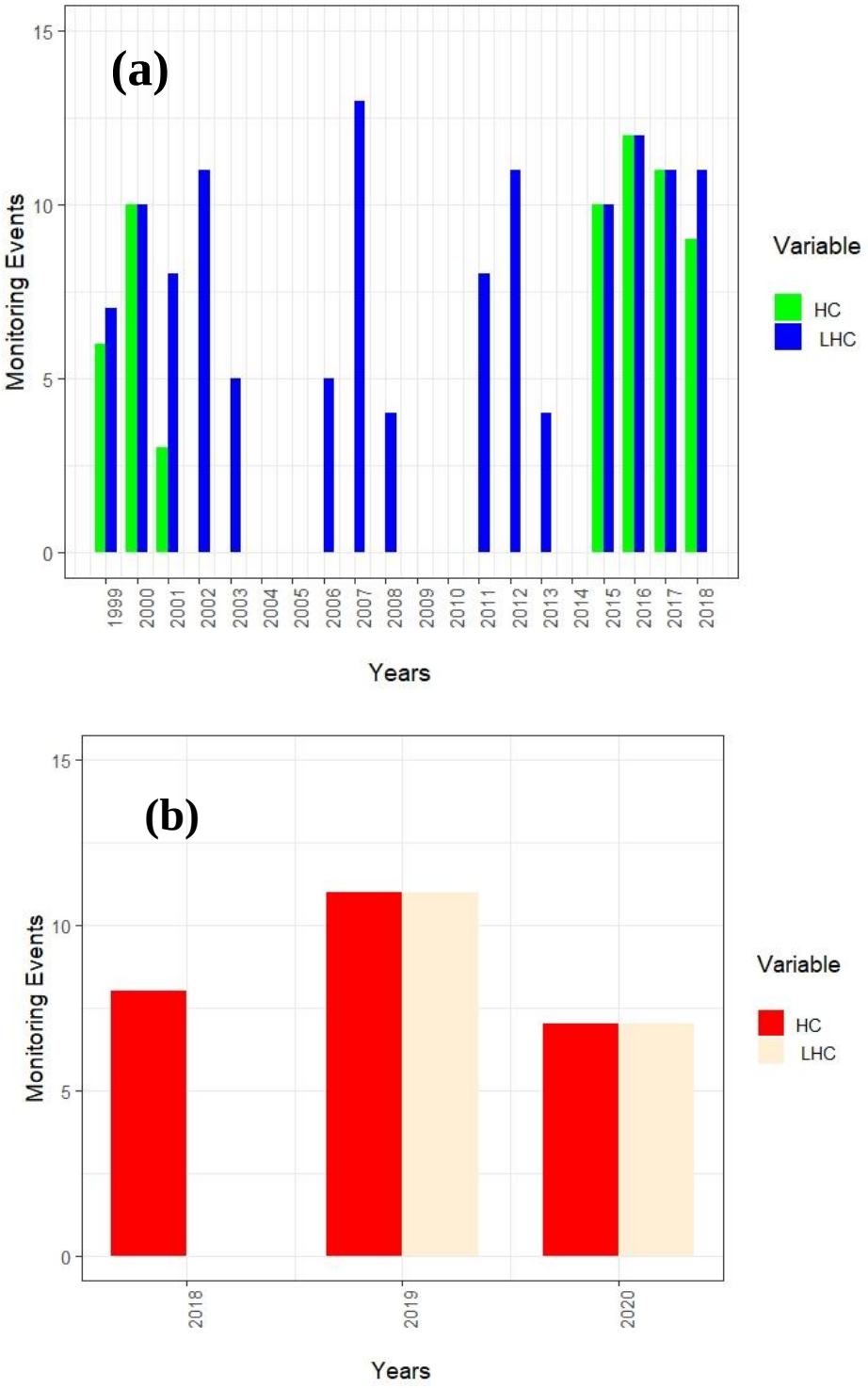

Figure 5.5. Frequency of data collection efforts at HC and LHC by (a) OCC 1999 - 2018 and (b) CREW 2018 - 2020.

5.2.3. Spatial Land Cover and Land Use Data

To determine LULC status for the watershed, the National Land Cover Database (NLCD) (USGS, 2020) was used. The NLCD is a Landsat-based database developed by the United States Geological Survey (USGS). This product provides spatial reference and descriptive data for the LULC of the continental United States (US). This product has a spatial resolution of 30 m and the temporal resolution includes annualized data for 2001, 2004, 2006, 2008, 2011, 2013 and 2016 (USGS, 2020).

5.2.3.1. National Land Cover Database (NLCD)

NLCD datasets were obtained from the Multi-Resolution Land Characteristics Consortium server (MRLC, 2020). For this project, LULC data for the Upper Horse Creek watershed (HUC 12 110702060402) were used.

5.2.3.2. Multispectral Data – Small Unoccupied Aerial System

Multispectral data for this project were collected with an Aerial Technology International (ATI) AgBOT small Unoccupied Aerial System (sUAS). This sUAS is a vertical takeoff and landing (VTOL) quadcopter (38 cm tri-prop and 4012 400Kv motors), made of carbon fiber (frame), and aluminum (fittings) weighing 4.7 kg (including sensor and batteries). On-board, the AgBOT is equipped with two 6S 6500 mAh lithium polymer (LiPo) batteries (that allow for 26+ minutes of flight time), UBlox Global Positioning System (GPS), compass module, downwelling light sensor (DLS) (an addition made in mid-2020) and a MicaSense RedEdge multispectral sensor. The MicaSense RedEdge sensor has a radiometric resolution of 16-bit and spectral resolution of five bands, capable of collecting information in the blue, green, red, red edge and NIR portion of the electromagnetic spectrum. This sensor has a ground

sample difference of 5.4 cm/pixel (at 60 m above ground level (AGL)), a horizontal field of view (HFOV) of 47.2°, and a capture speed of 1 second/band (ATI, 2019).

For this project, multispectral imagery of the riparian conservation easements was collected on October 16, 2020 at 12:00 PM CDT. For this purpose, three missions were flown at a 150-m altitude and at a flying speed of 15 m/s. In total, 622 images were captured, with a spatial resolution of 10.5 cm. Radiometric calibration of the images was performed using the on-board DLS which was recently purchased and installed on the sUAS. All three missions were designed in Mission Planner 1.3.74 (Mission Planner, 2019) and the stitching of all images was performed using Pix4Dmapper 4.6.1 (PiX4Dmapper, 2011).

5.2.4. Spatial Data Analysis

To examine the relationship between water quality and LULC, redundancy analysis (RDA) was used. To perform this analysis (and due to the temporal constraints of NLCD products) water quality data from 2001 – 2016 were used. Because the NLCD data does not have a product for each year since 2001, it was assumed that the LULC for those years that had no product (e.g., 2002, 2003, 2005, 2007, 2009, 2010, 2012, 2014, and 2015) were the same as the next closest year. Normality of the datasets was determined by the Shapiro–Wilk test. For those parameters where the assumption was not met, a ln(x+1) transformation was performed to account for reported zero values. All statistical analyses were conducted in R 3.5.1 (R Core Team, 2017).

5.3.Results

5.3.1. Water Quality and Water Quantity

Tables 5.3 and 5.4 summarize the water quality and water quantity parameters measured in HC and LHC by OCC and CREW, respectively.

In terms of nutrient analytes, between the OCC and CREW datasets, five parameters can be directly compared (e.g., ortho-phosphorus (PO_4^{3-}), nitrate (NO_2^-), nitrite (NO_3^-), SO_4^{2-}, and TSS) for both creeks. When statistically comparing these five parameters by creek (LHC OCC with LHC CREW and HC OCC with HC CREW), it was determined by means of a Welch's t-test that the data generated in each creek were not statistically different (p-value $\geq$ 0.05). By performing this same comparison between each creek (LHC OCC with HC OCC and LHC CREW with HC CREW), it was determined that data for LHC and HC in both datasets were statistically different (p-value $\leq$ 0.05). As for water quantity (e.g., flow (Q)), the same trend was determined, for both datasets LHC and HC were statistically different (p-value $\leq$ 0.05), but between the data presented in both datasets there was not a statistical difference (p-value $\geq$ 0.05). On the basis of these results, and to perform trend analyses (and future statistical analysis) for PO_4^{3-}, NO_2^-, NO_3^-, SO_4^{2-}, and TSS, both datasets (OCC and CREW) were merged.

Figure 5.6 and 5.7 present a graphical trend analysis for PO_4^{3-}, NO_2^-, NO_3^-, SO_4^{2-}, and TSS in HC and LHC between 2000 – 2020. By looking at fitted trendlines, it can be observed that during the two decades of sampling, NO_2^- , NO_3^-, SO_4^{2-}, and TSS concentrations have remained relatively constant in both creeks. and PO_4^{3-} (in HC and LHC) concentrations have seen a slight increase during the sampling period. It is imperative to mention that with the collected data, it is unknown if that slight increase in PO_4^{3-} for HC and LHC is responsible for the BGA blooms in 2011 and subsequent years.

Table 5.3. Water quality and water quantity statistical summary. Data collected at LHC and HC by OCC between 1999 - 2018. Min, Max, and SE refer to minimum, maximum, and standard error, respectively.

LHC									
Parameter	**Min**	**1st Qu.**	**Median**	**Mean**	**3rd Qu.**	**Max**	**SE**	**No Data**	**n**
Flow (cfs)	0.000	0.000	0.344	4.254	3.741	95.233	1.085	11	108
Ammonia (mg/L)	0.008	0.021	0.050	0.132	0.128	2.240	0.032	41	78
Conductivity (µS/cm)	64.4	240.5	321.3	302.8	366.3	713.0	10.3	11	108
DO (mg/L)	2.320	5.815	7.790	8.196	10.480	14.600	0.365	46	73
TKN (mg/L)	0.110	0.500	0.720	0.866	1.089	3.930	0.058	9	110
Nitrate (mg/L)	0.020	0.060	0.265	0.550	0.670	9.850	0.109	18	101
Nitrite (mg/L)	0.002	0.020	0.020	0.158	0.033	10.800	0.108	18	101
PO_4^{3-} (mg/L)	0.005	0.049	0.134	0.187	0.251	0.852	0.018	9	110
TP (mg/L)	0.027	0.094	0.176	0.243	0.310	1.068	0.021	9	110
Sulfate (mg/L)	1.12	12.48	17.45	56.59	26.17	1907.40	24.46	10	109
TSS (mg/L)	1.00	10.00	10.00	20.13	10.00	401.00	5.26	25	94
HC									
Parameter	**Min**	**1st Qu.**	**Median**	**Mean**	**3rd Qu.**	**Max**	**SE**	**No Data**	**n**
Flow (cfs)	0.053	0.202	0.398	3.582	2.608	31.366	1.089	13	40
Ammonia (mg/L)	0.015	0.048	0.120	0.369	0.305	2.990	0.121	21	32
Conductivity (µS/cm)	50.9	206.1	289.1	306.9	379.8	676.0	20.0	0	53
DO (mg/L)	2.930	5.000	9.000	8.590	10.880	17.140	0.566	8	45
TKN (mg/L)	0.250	0.880	1.230	1.505	1.820	4.930	0.129	0	53
Nitrate (mg/L)	0.020	0.050	0.350	0.520	0.730	2.740	0.086	8	45
Nitrite (mg/L)	0.013	0.020	0.020	0.080	0.070	0.680	0.019	8	45
PO_4^{3-} (mg/L)	0.008	0.110	0.201	0.268	0.366	0.805	0.029	0	53
TP (mg/L)	0.067	0.237	0.278	0.376	0.514	0.943	0.031	0	53
Sulfate (mg/L)	4.20	16.20	23.40	68.80	44.10	2007.20	37.42	0	53
TSS (mg/L)	1.00	10.00	10.00	20.63	18.00	180.00	3.88	0	53

Table 5.4. Water Quality and Water Quantity statistical summary. Data collected at LHC and HC collected dataset by CREW between 2018-2020. Min, Max, and SE refer to minimum, maximum, and standard error, respectively.

LHC									
Parameter	**Min**	**1st Qu.**	**Median**	**Mean**	**3rd Qu.**	**Max**	**SE**	**No Data**	**n**
Flow (cfs)	0	0.1	1.3	4.1	2.9	39.5	2.4	1	16
Ammonia (mg/L)					<BDL*				
Conductivity (µS/cm)	114	215	276	263	311	371	18.6	0	17
DO (mg/L)	6.4	8.3	12.3	11.7	15.1	18.1	0.9	0	17
TN (mg/L)	0.3	0.5	0.7	0.9	1.3	2.4	0.1	0	17
Nitrate (mg/L)	0.1	0.3	0.4	0.6	0.8	1.7	0.1	0	17
Nitrite (mg/L)	0.01	0.01	0.02	0.03	0.03	0.1	0.01	4	13
PO_4^{3-} (mg/L)	0.1	0.2	0.3	0.3	0.3	1.4	0.1	0	17
Sulfate (mg/L)	13.1	17.1	27.3	24.9	29.3	40.9	2.1	2	15
TSS (mg/L)	1.6	5.6	6.7	9.9	12.6	35.9	2.1	0	17
HC									
Parameter	**Min**	**1st Qu.**	**Median**	**Mean**	**3rd Qu.**	**Max**	**SE**	**No Data**	**n**
Flow (cfs)	0	0.1	1.2	5.5	2.5	47.5	2.4	1	24
Ammonia (mg/L)					<BDL*				
Conductivity (µS/cm)	104	210	308	292	352	431	18.8	0	25
DO (mg/L)	1.4	6.9	11.4	10.4	13.4	17.3	0.9	0	25
TN (mg/L)	0.3	1.1	1.5	1.9	2.1	7.8	0.3	0	25
Nitrate (mg/L)	0.2	0.3	0.5	1	1.3	5.4	0.2	0	25
Nitrite (mg/L)	0.02	0.02	0.03	0.04	0.04	0.1	0.01	12	13
PO_4^{3-} (mg/L)	0.1	0.3	0.4	0.5	0.6	1.5	0.1	0	25
Sulfate (mg/L)	21.3	25.3	31.2	32.7	37.1	56.3	2.6	10	15
TSS (mg/L)	3.4	7.1	9.7	33.4	18.4	315.3	13.9	0	25

*BDL = Below Detection Limit (0.4 mg/L)

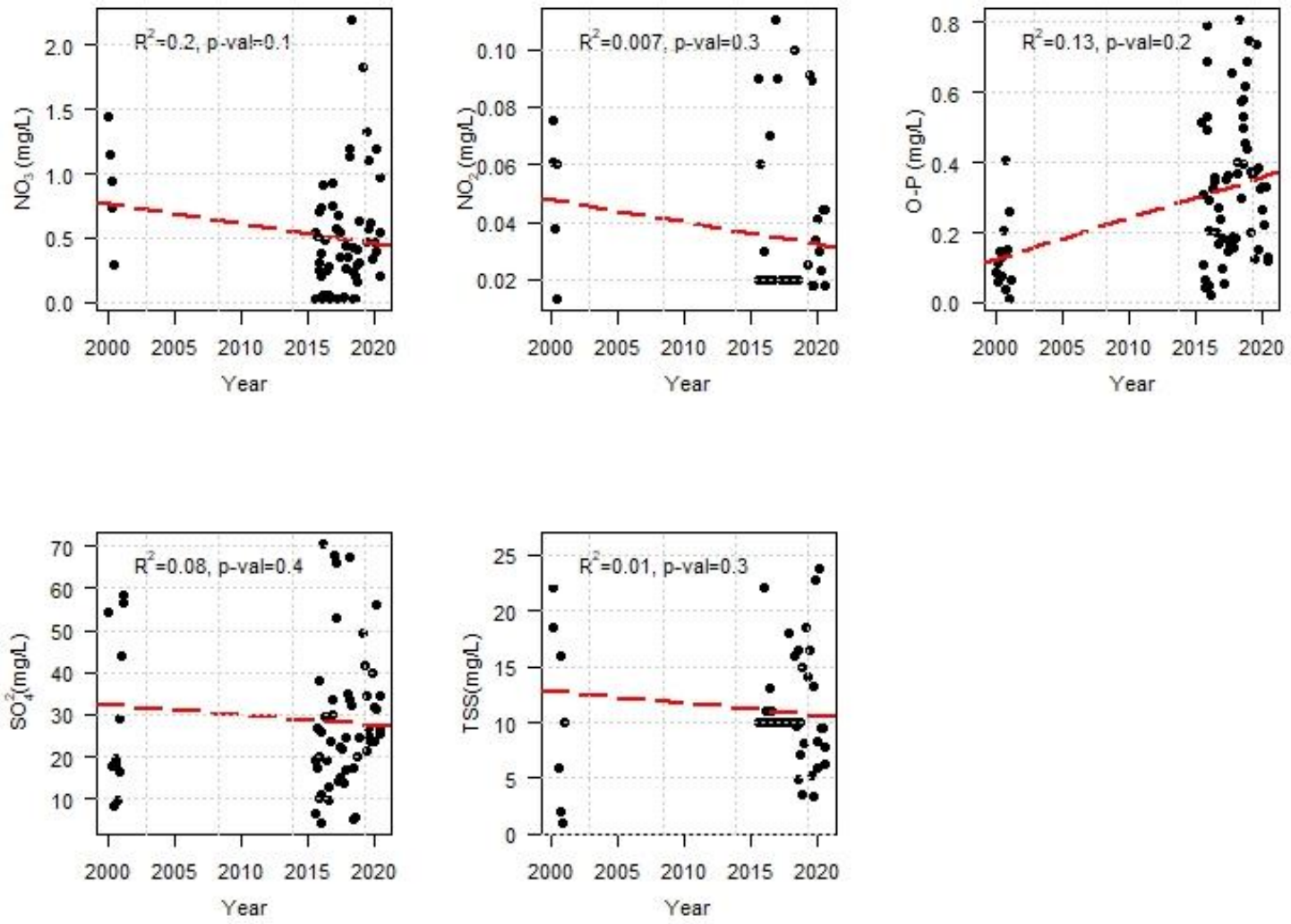

Figure 5.6. Trend analysis for PO_4^{3-}, NO_2^-, NO_3^-, SO_4^{2-}, and TSS in HC between 2000 – 2020.

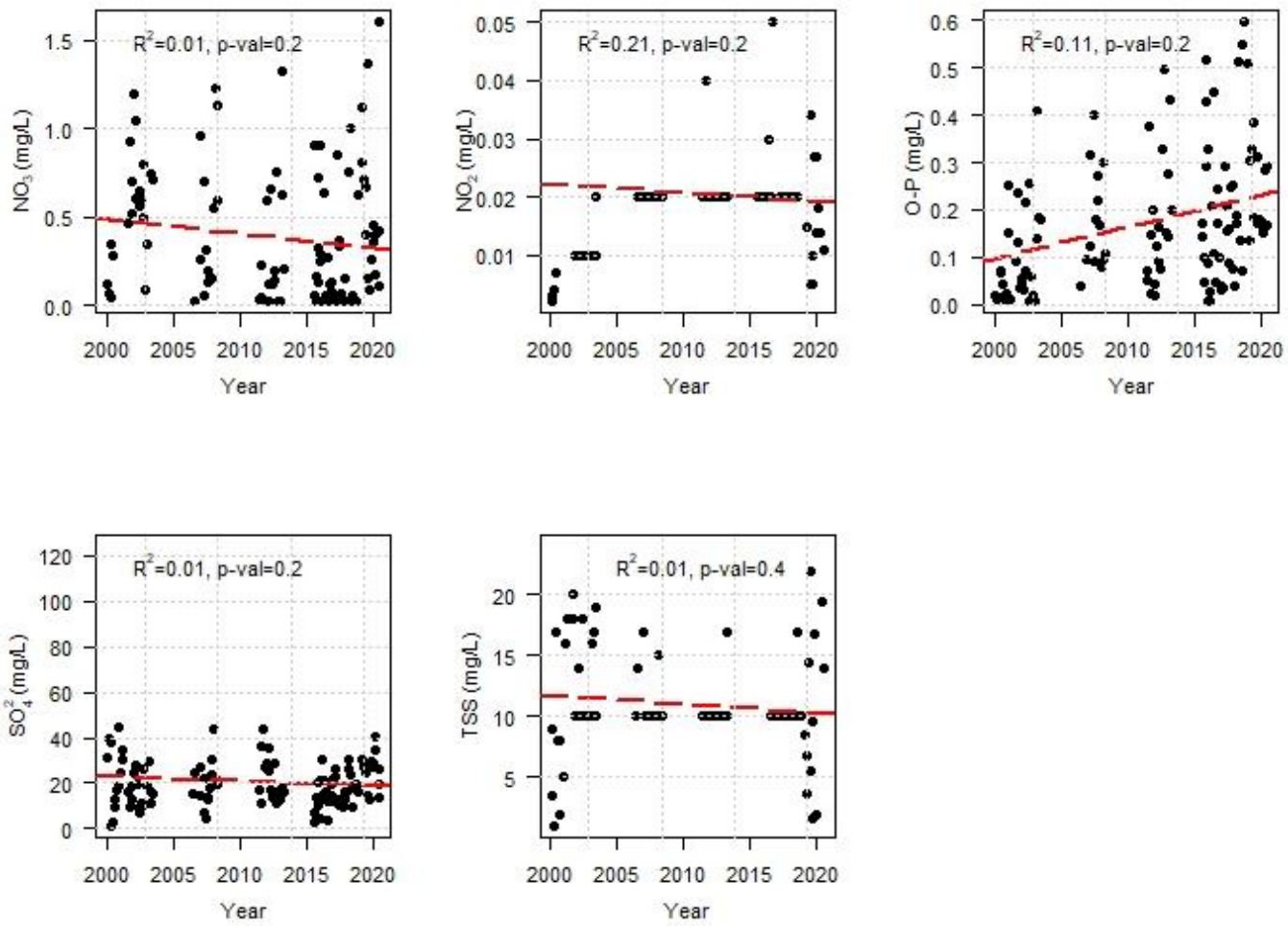

Figure 5.7. Trend analysis for PO_4^{3-}, NO_2^-, NO_3^-, SO_4^{2-}, and TSS in LHC between 2000 – 2020.

By merging the two datasets (OCC and CREW) and analyzing the behavior of nutrient and TSS concentrations throughout the almost the two decades of sampling, it was determined that there was no significant difference in any parameter from year to year (Tukey-Kramer test), with the exception of NO_2^- in LHC during 2003.

As for HC nutrients (PO_4^{3-}, NO_2^-, NO_3^-, SO_4^{2-}) and TSS concentrations, and as presented in Figure 5.6, it can be observed that the missing data between 2001 to 2011, creates a bimodal distribution among the datasets. Further statistical analysis between these distributions (treating each as two separate temporal sets) shows that statistically there is no difference (p-value $\geq$ 0.05) throughout the sampling period for all nutrients and TSS concentrations. Figures 5.8 and 5.9 present annualized box and whisker plots of the nutrients compared throughout the sampling period for LHC and HC, respectively.

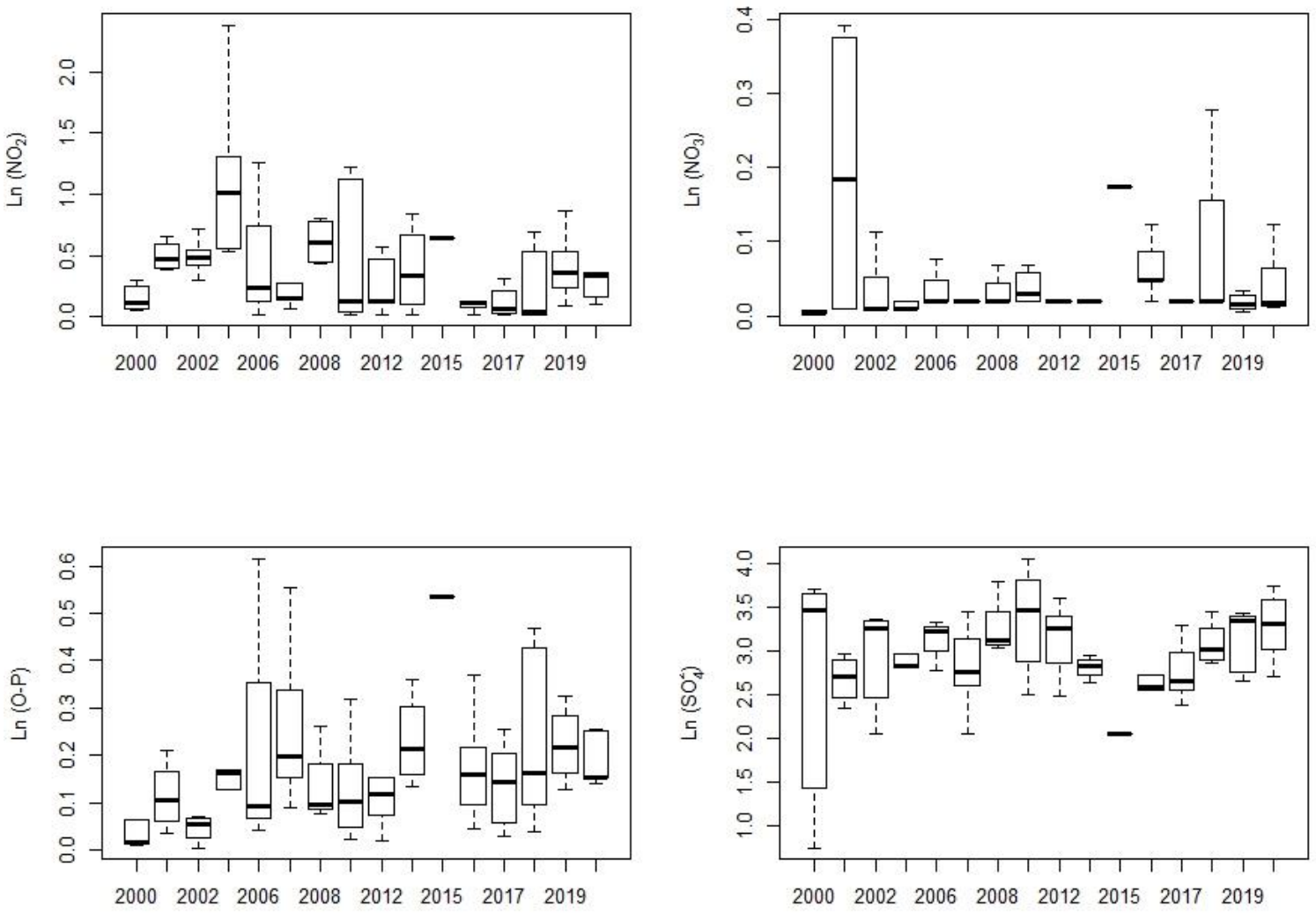

Figure 5.8. Box and whiskers plot for PO_4^{3-}, NO_{2-}, NO_{3-}, and SO_4^{2-} in LHC from 2000 to 2020. All units in ln(mg/L)

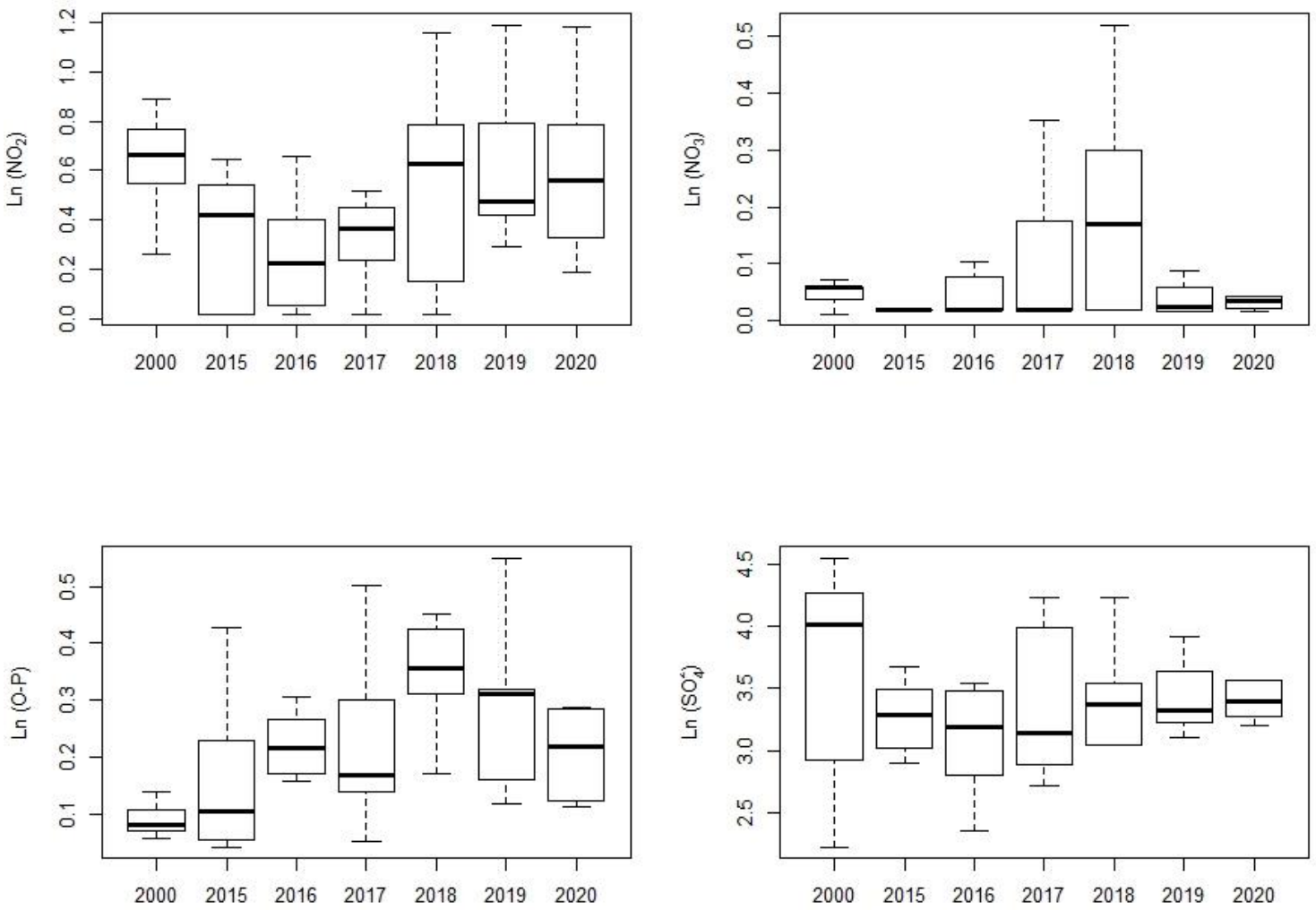

Figure 5.9. Box and whiskers plot for PO_4^{3-}, NO_2^-, NO_3^-, and SO_4^{2-} in HC from 2000 to 2020. All units in ln(mg/L)

5.3.2. Seasonal Variability

Nutrients (e.g., TKN, TN, TP, PO_4^{3-}, NO_2^-, NO_3^-, and SO_4^{2-}) and TSS concentration seasonal variability among the overall datasets was examined by dividing the data collected at LHC and HC into the four predominant seasons for the region (e.g., winter (December-February), fall (September-November), spring (March-May) and summer (June-August)). Figures 5.10 and 5.11 present graphical summaries of the seasonal variability analyses for LHC and HC, respectively. From these analyses, it can be determined that at HC, mean concentrations of TKN, PO_4^{3-}, and TP were greater in the spring and summer seasons, and TN, NO_2^-, and NO_3^- were greater in the spring and winter months. As for LHC, mean concentrations of TKN, TP and PO_4^{3-} were greater during the summer and spring seasons and TN, NO_2^- and NO_3^- were greater during the spring and winter months. For both creeks, mean concentrations of SO_4^{2-} were greater during the spring and winter seasons. Statistical difference (by means of a Tukey-Kramer test) was determined only for NO_2^-, NO_3^-, and SO_4^{2-} in both datasets (p-value ≤ 0.05).

The same seasonal analyses were performed using precipitation data from 1999 to 2020. For this purpose, data from the three closest Mesonet stations (e.g., Jay (25.23 km), Vinita (28.64 km), and Miami (24.28 km)) were used to interpolate (by means of inverse distance weighting (IDW) interpolation) precipitation values at the HC sampling station. Table 5.5 presents a statistical summary of the calculated precipitation data. It can be determined that during the past two decades, the spring and summer months had on average more rain than the fall and winter months.

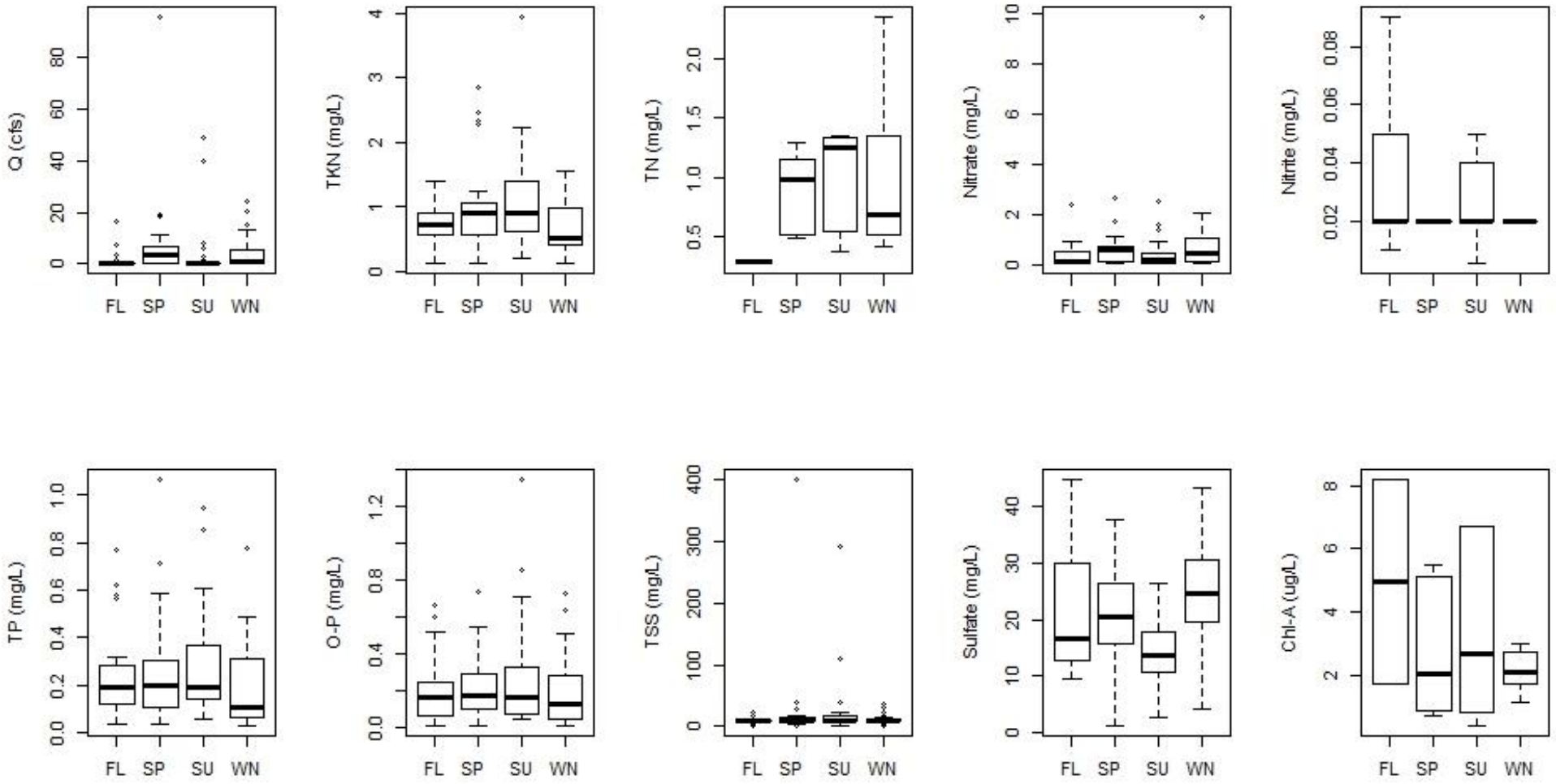

Figure 5.10. Seasonal water quality variability in LHC. FL, SP, SU and WM refer to fall, spring, summer, and winter, respectively.

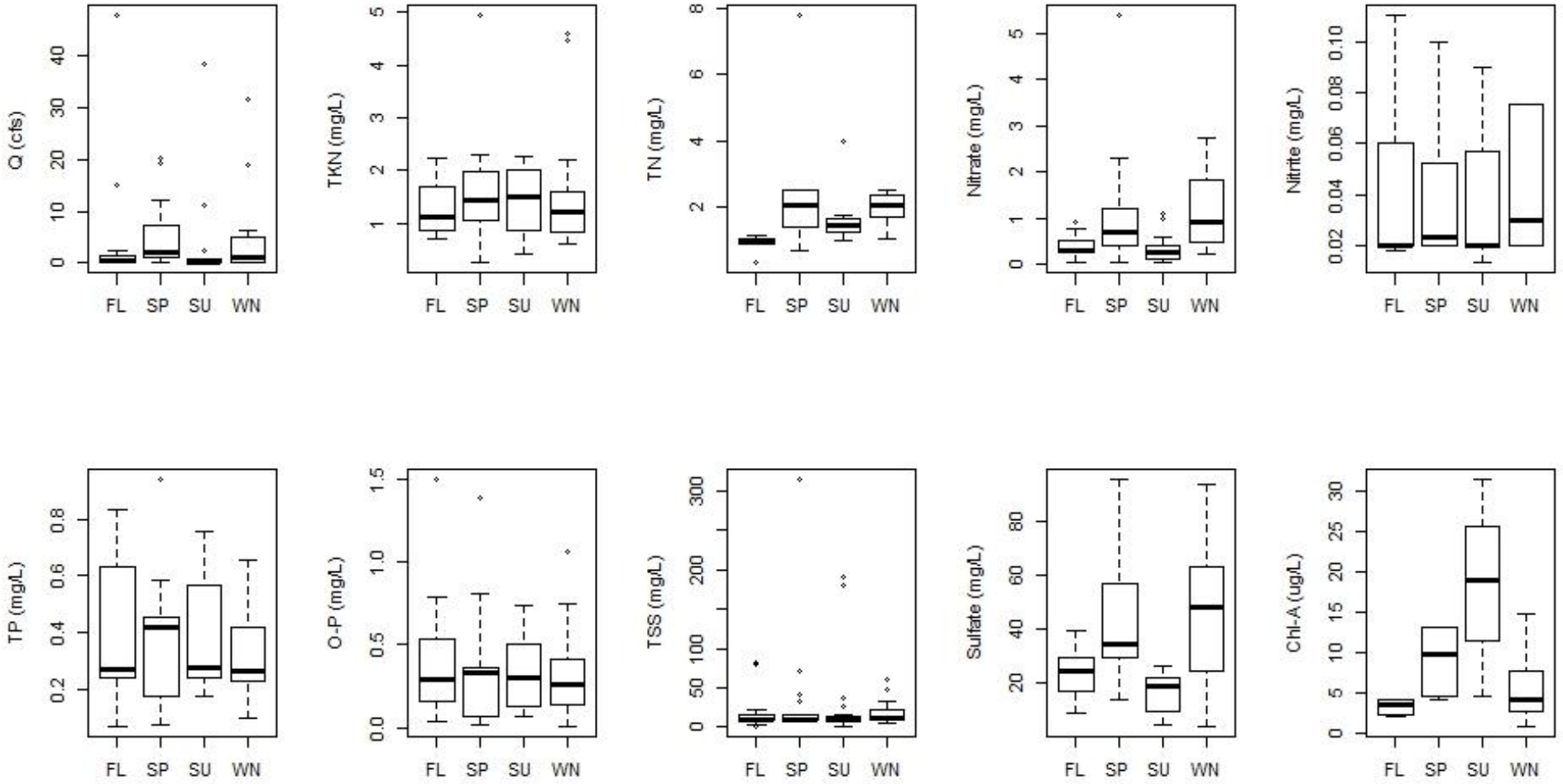

Figure 5.11. Seasonal water quality variability in HC. FL, SP, SU and WM refer to fall, spring, summer, and winter, respectively.

Table 5.5. Statistical summary of the calculated/interpolated precipitation (inches/month) data at HC sampling stations between 1999 – 2020. Min, Max, and SE refer to minimum, maximum, and standard error, respectively.

	Winter	**Fall**	**Summer**	**Spring**
Mean	2.14	3.43	5.23	4.26
SE	0.203	0.49	1.05	0.532
Min	1.90	2.48	3.61	3.55
Max	2.55	4.14	7.21	5.30

5.3.3. Mass Loadings

Calculations of mass loading rates for LHC and HC between 2000 and 2020 were based on the product of the measured volumetric flow rate (Q) multiplied by the concentrations of PO_4^{3-}, NO_2^-, NO_3^-, SO_4^{2-} and TSS to estimate "absolute" mass loads. That load was divided by the surface area of the contributing watershed upgradient of each CREW sampling point (e.g., HC = 76 km^2 and LHC = 50 km^2) to estimate area-adjusted mass loads. Due to the nature of the collected dataset, it was assumed that the measurement of nutrient concentrations and Q at a specific location in time and space, was representative of the conditions of each stream at that time and location.

Tables 5.6 and 5.7 present statistical summaries of the calculated mass loads (kg day^{-1}) and the area-adjusted mass loads (kg day^{-1} ha^{-1}) for PO_4^{3-}, NO_2^-, NO_3^-, SO_4^{2-} and TSS at HC and LHC, respectively from 2000 to 2020. From Table 5.6, it can be observed that, on average, the mass loading rates for NO_3^-, PO_4^{3-}, and SO_4^{2-} were generally greater at HC than at LHC. However, when statistically comparing these mass loading rates, it was determined by means of a Welch's t-test that statistically there was no difference (p-value ≥ 0.05) between HC and LHC in terms of mass loading rates. When looking at Table 5.7, it can be observed that on average the area-adjusted mass loading rates in HC were higher than in LHC; however, statistically (by means of a Welch's t-test) there was no difference (p-value ≥ 0.05) between them.

Table 5.6. Statistical summary of the calculated absolute mass loading rates (kg day^{-1}) for PO_4^{3-}, NO_2^-, NO_3^-, SO_4^{2-} and TSS in HC and LHC from 2000 - 2020.

HC						
Analyte	**Mean**	**Median**	**SE**	**Min**	**Max**	**n**
NO_2^-	7.8	1.4	1.8	$3x10^{-3}$	53.7	53
NO_3^-	0.8	0.1	0.4	$2x10^{-3}$	11.9	45
O-P	4.4	0.4	1.3	$1x10^{-2}$	44.4	59
SO_4^{2-}	363.3	66.3	107.8	1.3	19250.9	53
TSS	287.5	20.3	94.1	0.6	3498.2	59
LHC						
Analyte	**Mean**	**Median**	**SE**	**Min**	**Max**	**n**
NO_2^-	9.8	1.1	2.5	$2x10^{-3}$	151.4	75
NO_3^-	0.7	0.1	0.4	$2.7x10^{-4}$	23.3	73
O-P	3.9	0.4	1.1	$2.8x10^{-3}$	50.6	80
SO_4^{2-}	272.4	84.2	62.5	$5.2x10^{-2}$	3740.6	77
TSS	212.8	52.2	67.3	$4.2x10^{-2}$	4190.9	71

Table 5.7. Statistical summary of the calculated contributing area mass loading rates (g day^{-1} ha^{-1}) for PO_4^{3-}, NO_2^-, NO_3^-, SO_4^{2-} and TSS at HC and LHC from 2000 - 2020.

HC						
Analyte	**Mean**	**Median**	**SE**	**Min**	**Max**	**n**
NO_2^-	1.1	0.2	0.2	$6.43x10^{-4}$	7.1	52
NO_3^-	0.1	0.1	0.1	$6.43x10^{-4}$	1.6	43
O-P	0.6	0.1	0.2	$1.66x10^{-3}$	5.9	58
SO_4^{2-}	47.8	8.8	14.2	0.164	2533.1	53
TSS	0.1	$2.6x10^{-3}$	0.1	$7.7x10^{-5}$	0.5	59
LHC						
Analyte	**Mean**	**Median**	**SE**	**Min**	**Max**	**n**
NO_2^-	1.9	0.2	0.5	$2.35\ x10^{-4}$	30.2	76
NO_3^-	0.1	0.1	0.1	$5.38\ x10^{-5}$	4.6	74
O-P	0.8	0.1	0.2	$5.59x10^{-4}$	10.1	81
SO_4^{2-}	56.5	17.4	13.1	0.011	748.6	78
TSS	0.1	0.1	0.1	$8.4x10^{-6}$	0.8	71

Figure 5.12 and Figure 5.13 present the seasonal distribution of the calculated mass loading rates and the area-adjusted mass loading rates in HC and LHC. For both cases, mass loading rates for PO_4^{3-}, NO_2^-, NO_3^-, SO_4^{2-} and TSS were higher in winter and spring compared to the summer and fall months.

Analyzing the behavior of the mass loading rates (absolute and area-adjusted) throughout the sampling period, it was determined by means of a Tukey-Kramer test that in LHC and HC mass loading rates did not present statistical differences (p-value ≥ 0.05).

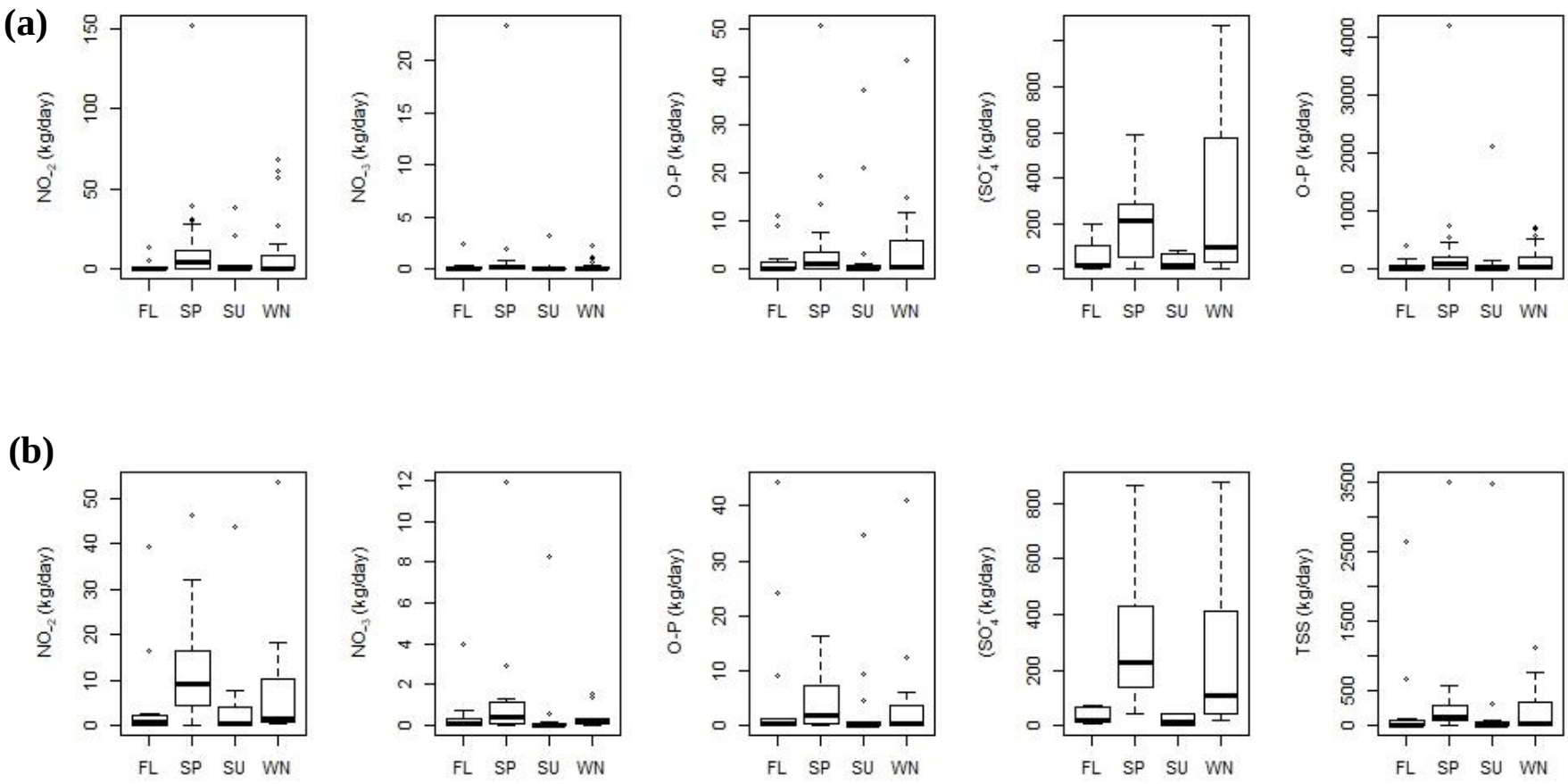

Figure 5.12. Seasonal distribution of the absolute mass loading rates in (a) LHC and (b) HC. FL, SP, SU and WN refer to fall, spring, summer, and winter, respectively.

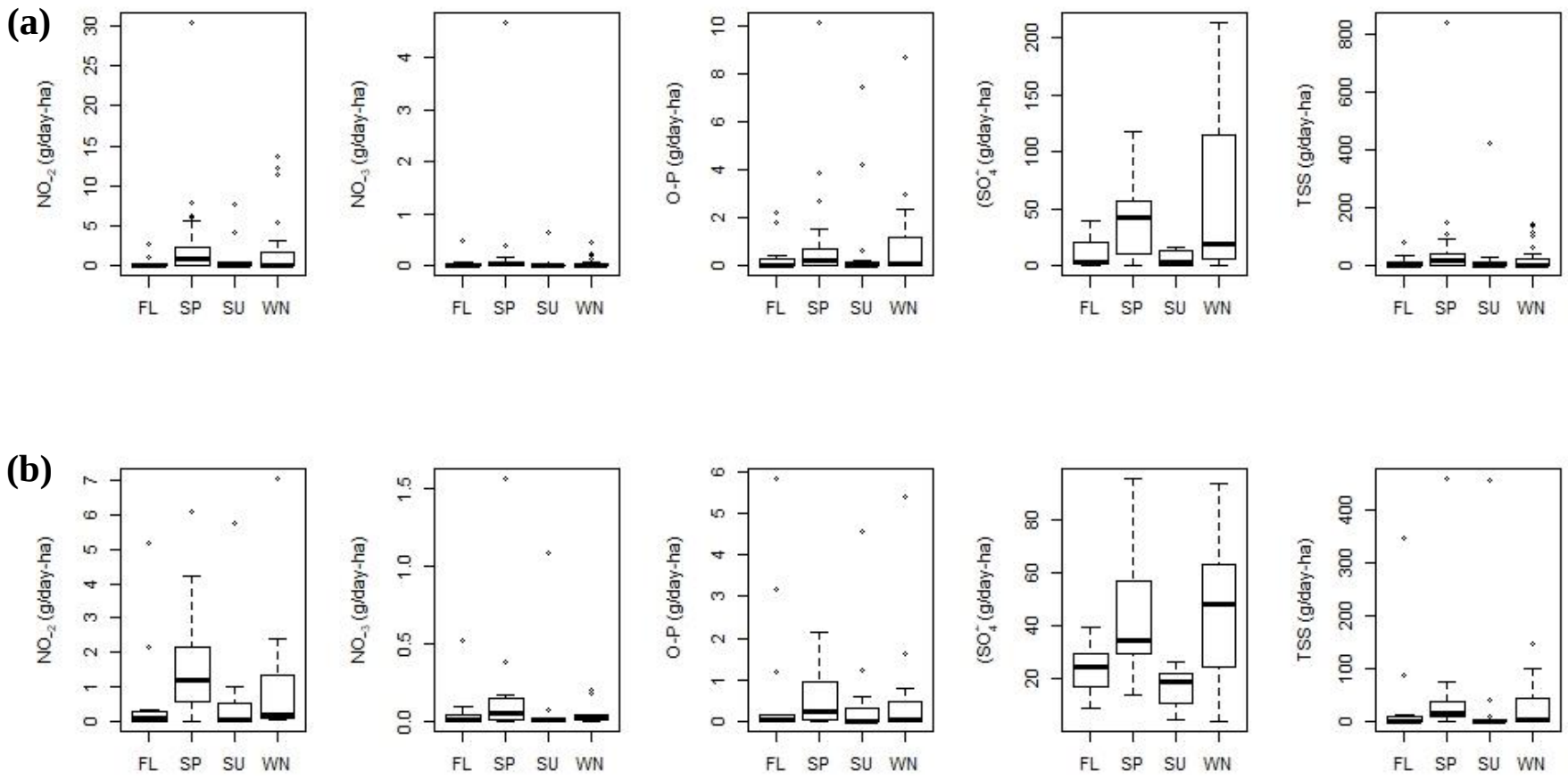

Figure 5.13. Seasonal distribution of the contributing area mass loading rates in (a) LHC and (b) HC. FL, SP, SU and WN refer to fall, spring, summer, and winter, respectively.

5.3.4. Land Use/Land Cover Changes

5.3.4.1. NLCD – 30 m Resolution

Figure 5.14 presents the LULC class percentage distribution for the Upper Horse Creek watershed from 2001 to 2016 according to the NLCD dataset. Currently for the watershed there are 14 LULC classes, however, 90% of the area is dominated by two classes: (1) pasture/hay and (2) cultivated crops, with percentage distribution of 62% and 28%, respectively (Figure 5.15).

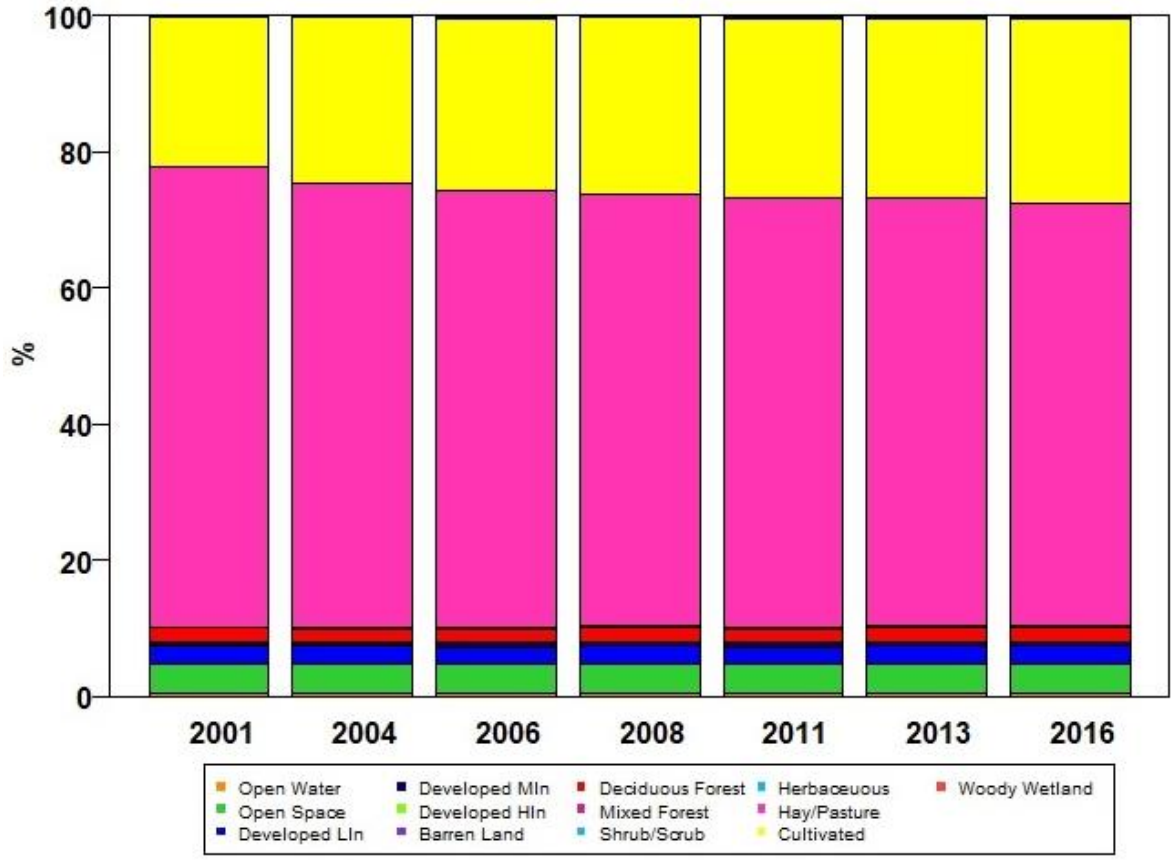

Figure 5.14. LULC for the sub-watershed Upper Horse Creek (HUC 12 110702060402) using NLCD data from 2001 to 2016.

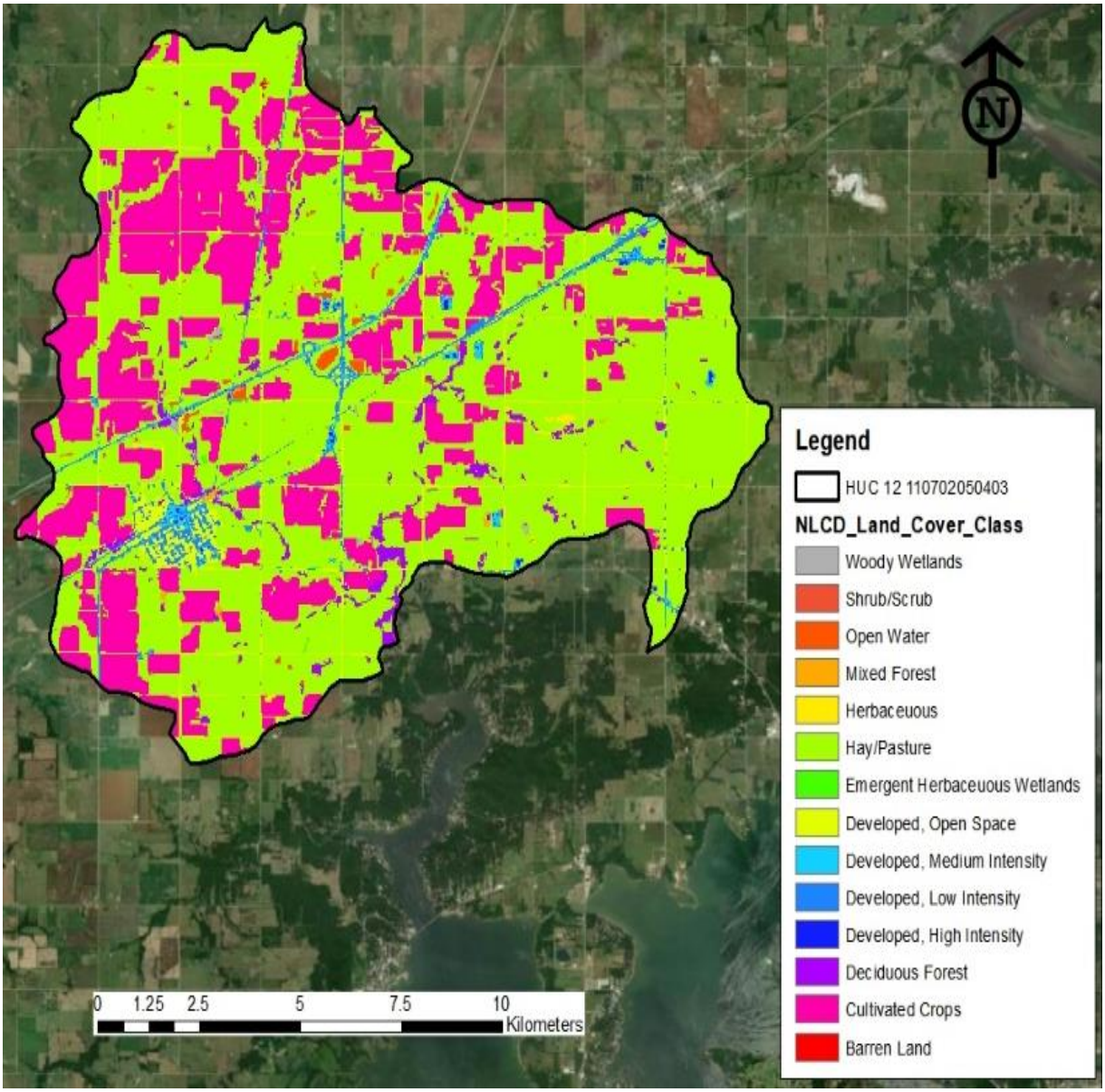

Figure 5.15. LULC distribution of the Upper Horse Creek sub-watershed (HUC 12 110702060402) according to the 2016 NLCD.

From 2001 to 2016, LULC for the watershed was relatively stable. Table 5.8 presents the LULC changes for the watershed in this 15-year period. The only major changes (> 5%) are the loss of 5.56% of pasture/hay and the gain of 5.36% of cultivated crops.

Table 5.8. LULC changes for the Upper Horse Creek sub-watershed (HUC 12 110702060402) using NLCD data from 2001 to 2016. Δ indicates de difference between 2016 and 2001.

Land Cover Class	2001 (%)	2004 (%)	2006 (%)	2008 (%)	2011 (%)	2013 (%)	2016 (%)	Δ (%)	Overall Mean (%)
Open Water	0.45	0.46	0.43	0.49	0.45	0.51	0.49	0.04	0.47
Developed, Open Space	4.34	4.34	4.34	4.34	4.34	4.34	4.35	0.01	4.34
Developed, Low Intensity	2.54	2.54	2.54	2.54	2.53	2.53	2.54	0.00	2.54
Developed, Medium Intensity	0.54	0.54	0.60	0.60	0.63	0.63	0.64	0.10	0.60
Developed, High Intensity	0.08	0.08	0.12	0.12	0.12	0.12	0.14	0.06	0.11
Barren Land	0.02	0.02	0.02	0.02	0.02	0.02	0.02	0.00	0.02
Deciduous Forest	2.13	2.03	2.03	2.03	2.01	2.01	2.02	-0.10	2.04
Mixed Forest	0.14	0.14	0.14	0.14	0.14	0.14	0.14	0.00	0.14
Shrub/Scrub	0.00	0.002	0.001	0.004	0.02	0.04	0.03	0.03	0.01
Herbaceous	0.11	0.16	0.18	0.16	0.22	0.17	0.18	0.07	0.17
Hay/Pasture	67.56	65.19	64.01	63.49	62.87	62.79	62.00	-5.56	63.99
Cultivated Crops	21.90	24.30	25.37	25.87	26.45	26.51	27.25	5.36	25.38
Woody Wetlands	0.13	0.14	0.14	0.14	0.14	0.13	0.13	0.00	0.13
Emergent Herbaceous Wetlands	0.07	0.07	0.07	0.07	0.07	0.06	0.07	0.00	0.07

By examining HC and LHC riparian areas using a 25-m buffer around the creeks, it can be determined that HC and LHC riparian areas have been dominated (≥ 50%) by pasture/hay (Table 5.9).

Table 5.9. LULC inside the riparian corridor using a 25 m buffer around HC and LHC using NLCD data from 2001 to 2016.

LHC								
LULC	**2001 (%)**	**2004 (%)**	**2006 (%)**	**2008 (%)**	**2011 (%)**	**2013 (%)**	**2016 (%)**	**Overall Mean (%)**
Develop, Open Space	1.3	1.3	1.3	1.3	1.3	1.3	1.3	1.3
Hay/Pasture	53.5	56.7	56.7	56.7	56.7	56.7	56.7	56.24
Deciduous Forest	43.2	42.0	42.0	42.0	42.0	42.0	38.3	41.7
Cultivated Crops	0.0	0.0	0.0	0.0	0.0	3.7	0.0	0.5
HC								
LULC	**2001 (%)**	**2004 (%)**	**2006 (%)**	**2008 (%)**	**2011 (%)**	**2013 (%)**	**2016 (%)**	**Overall Mean (%)**
Develop, Open Space	2.2	0	2.2	2.2	2.2	2.2	2.2	1.9
Develop, Low	1.0	0	1.0	1.0	1.0	1.0	1.0	0.8
Develop, Medium	0.1	0.1	0.1	0.1	0.1	0.1	0.1	0.1
Deciduous Forest	29.3	29.0	29.3	29.3	29.3	29.3	28.9	29.2
Mixed Forest	1.5	5.2	1.5	1.5	1.5	1.5	1.4	2.0
Hay/Pasture	62.7	62.2	62.5	62.7	62.6	62.7	61.0	62.4
Cultivated Crops	0.1	0.1	0.1	0.1	0.1	0.1	0.8	0.2
Woody Wetlands	3.1	3.0	3.1	3.1	3.1	3.1	4.2	3.2
Emergent herbaceous wetlands	0.0	0.1	0.1	0.0	0.1	0.0	0.1	0.1
Herbaceous	0.0	0.1	0.1	0.0	0.0	0.0	0.2	0.1

5.3.5. Effects of Land Use/ Land Cover on Water Quality

5.3.5.1. HC and LHC 2001 – 2016

Figures 5.16 and 5.17 present the graphical relationships (biplots) between LULC and seasonal water quality concentrations (e.g., PO_4^{3-}, NO_2^-, NO_3^-, and SO_4^{2-}) in HC and LHC, respectively, during winter, fall, summer, and spring from 2001 to 2016 using a 30-m spatial resolution. From the RDA it can be determined that HC and LHC present similar behaviors (the major difference is that in LHC there is no urban land use) when it comes to the influence that LULC has on water quality. At the same time, the RDA indicated that the two LULC (response variables) that statistically explain the variance in the seasonal water quality are pasture/hay and cultivated crops (cumulative eigenvalues for all cases were higher than 85%).

When looking at the biplots, it is imperative to point out that the distance between the constrained explanatory variables (e.g., pasture/hay, cultivated crops, forest, and developed

land (for LHC)) and the different water quality parameters (response variables) represents the linear relationship between these variables. The statistical correlation between such can be determined by the angular distance of the predictors and responses variables; when the included angle (between predictor and response variable) is less than 90 degrees, the relationship between them is positive (high correlation), in contrast, when included angle distance is over 90 degrees, the relationship between them is negative (low correlation). For these biplots, the direction of each arrow in the four plotting quadrants is random (interpretation based on distance not based on direction) and the magnitude is determined by the number of samples used (ter Braak, 1994).

For this analysis, and as observed in Figures 5.16 and 5.17 in all cases the relationship that the water quality analytes have with agricultural or urban land cover is positive (angle between lines is < 90°), while the relationship with forest cover is negative.

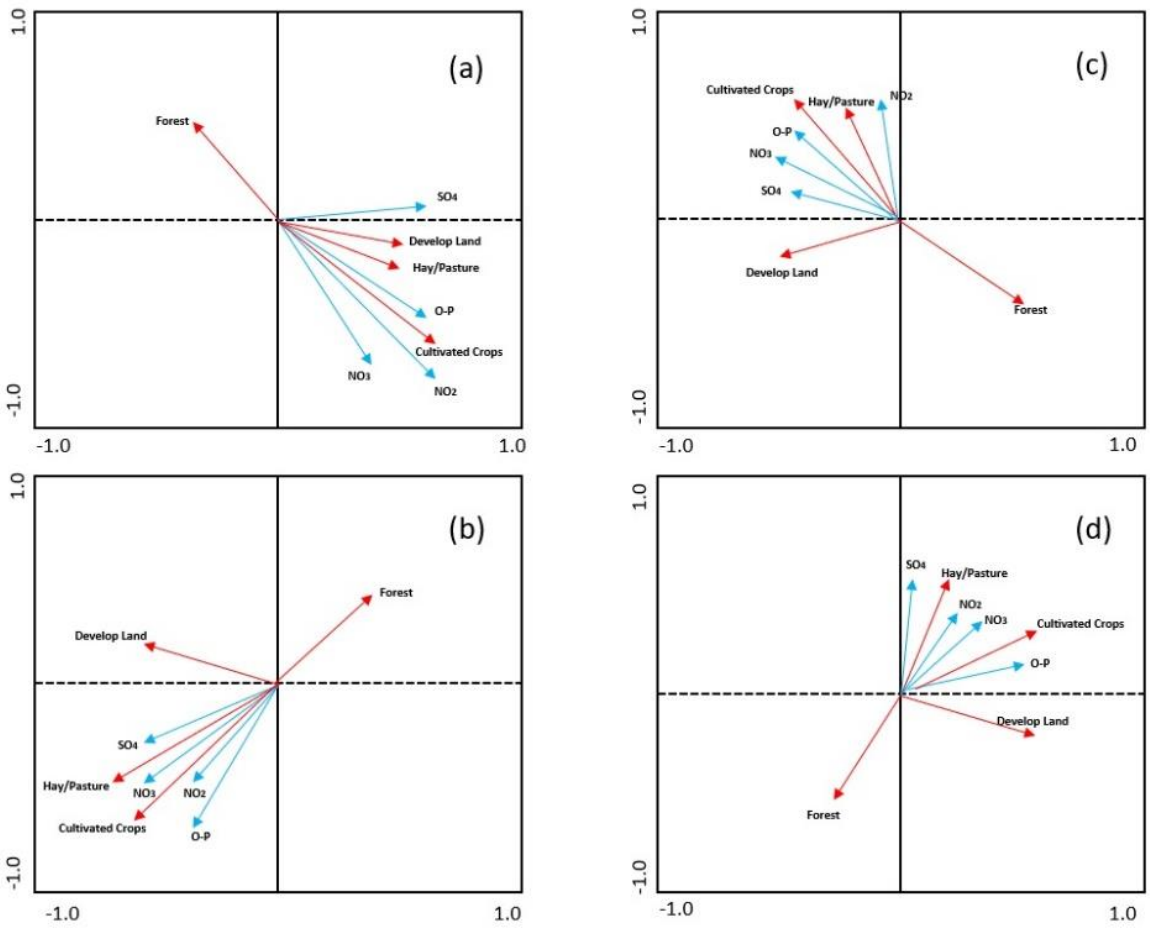

Figure 5.16. Relationship between LULC and (a) winter, (b) fall, (c) summer and (d) spring in HC using the 30 m spatial resolution from the NLCD data using RDA – 2001 to 2016.

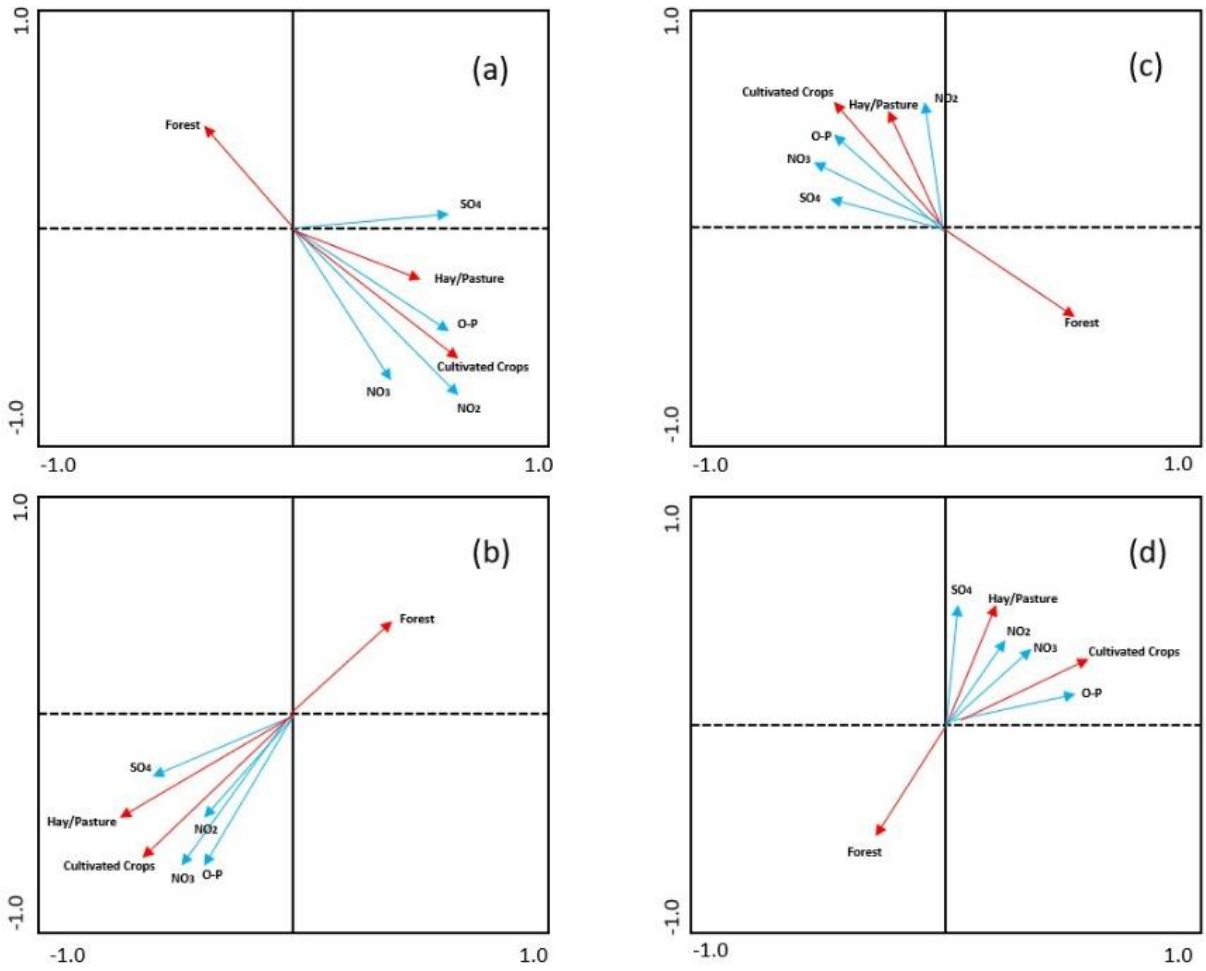

Figure 5.17. Relationship between LULC and (a) winter, (b) fall, (c) summer and (d) spring in LHC using the 30 m spatial resolution from the NLCD data using RDA – 2001 to 2016.

5.3.5.2. sUAS Imagery

Figures 5.18 and 5.19 present the surface elevation models and the calculated normalized difference vegetation index (NDVI) at the initial riparian conservation easements, using the imagery captured by the sUAS. NDVI was calculated using Equation 1 using as input the reflectance values of NIR and red band from captured multispectral imagery. NDVI is an index between -1 and 1 that represents the difference between visible and near-infrared reflectance of vegetation cover and can be used to estimate the greenness of an area (Weier and Herring, 2000; CGL, 2020). This is possible because "healthy vegetation has low red-light reflectance and high near-infrared reflectance that produce high NDVI values. The amount of positive NDVI values indicates the increase in the amounts of green vegetation. The NDVI values near zero and decreasing negative values indicate non-vegetated features, such as barren surfaces (rock and soil), water, snow, ice, and clouds" (Subbarayan, et al., 2019).

$$NDVI = \frac{NIR - RED}{NIR + RED} \qquad Equation\ 1$$

As part of the agreement entered by GRDA, OCC, and the private landowner, the conservation areas are to remain out of agricultural production for at least the next ten years. To do that, in 2018 barbed-wire fences were built around 0.7 km^2 of HC riparian zone in three different areas. The purpose of these fences is not only to keep cattle out of the stream, but also to allow the vegetation to naturally recolonize. Currently (based on monthly visits to the site), the area inside the fences is dominated by tall pasture, but there is a presence of clusters of trees on both sides of the channel in the north and east easements. Figure 5.20 presents an upstream view of the east easement.

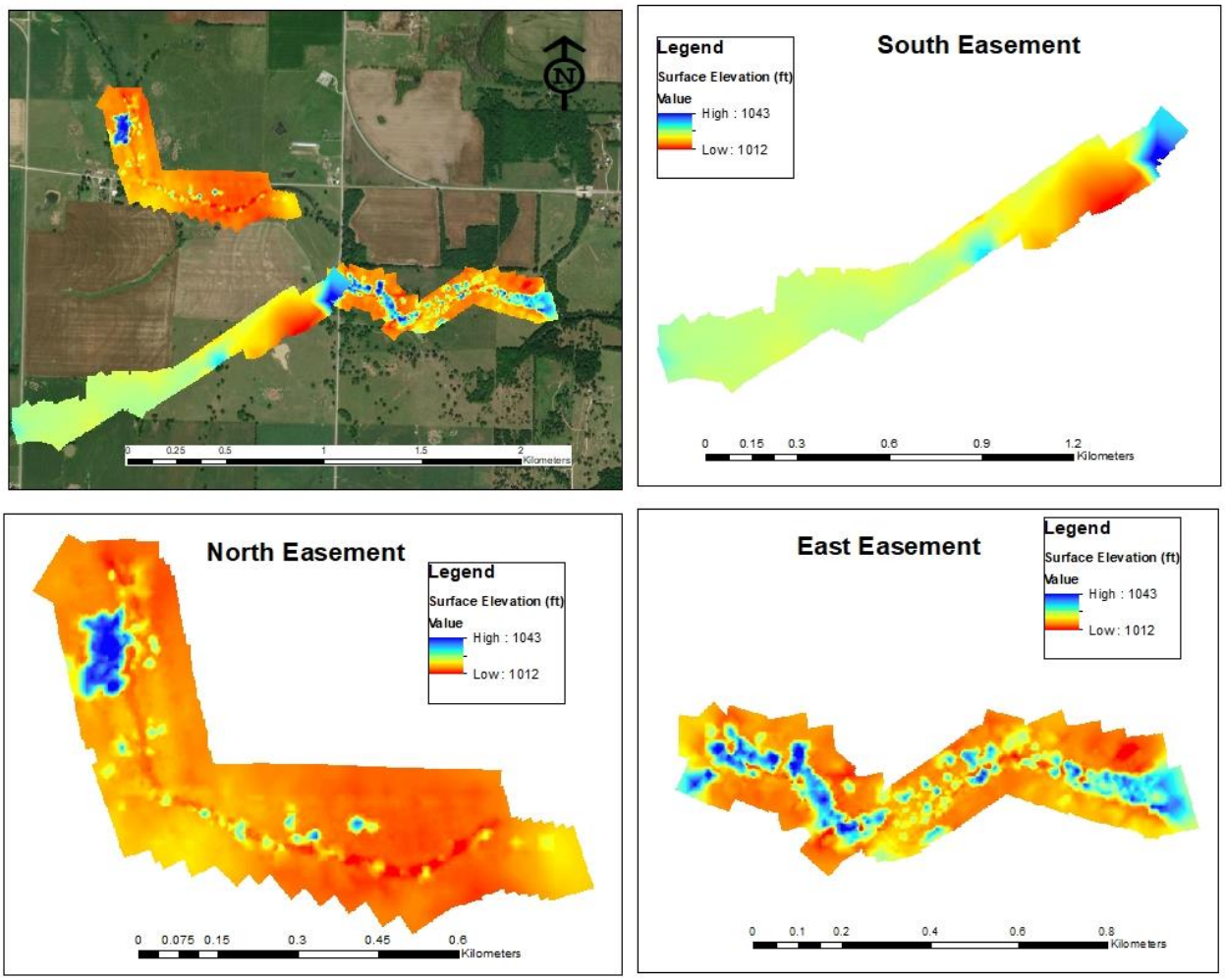

Figure 5.18. Surface elevation models at the initial riparian conservation easements using the sUAS imagery at 0.5-m spatial resolution.

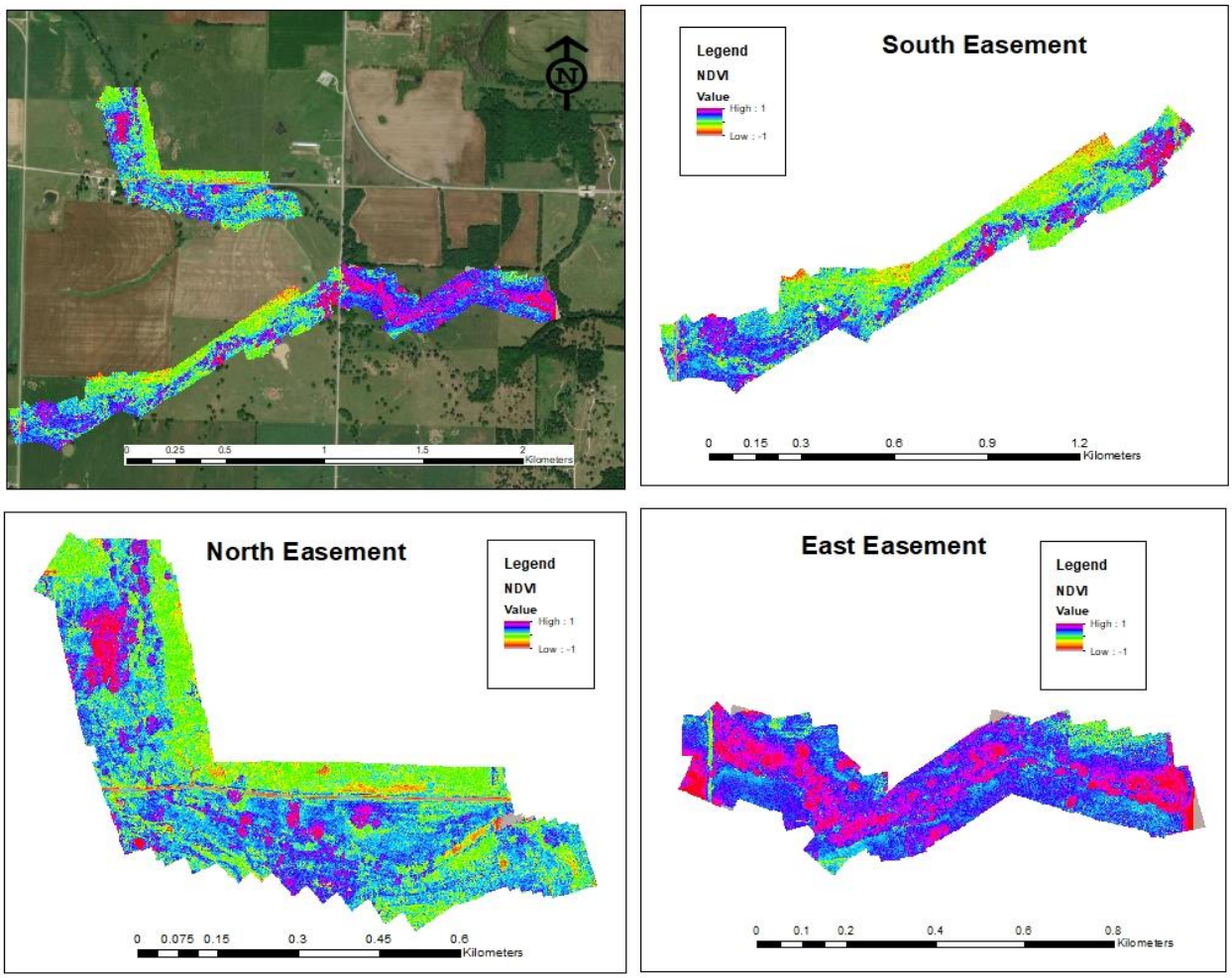

Figure 5.19. NDVI at the initial riparian conservation easements using the sUAS imagery at 0.5-m spatial resolution.

From Figure 5.19, it can be observed that at the time when these images were taken (mid-fall 2020), all the vegetation inside the area is healthy (NDVI values ≥ 0.8). However, by comparing the difference in ground elevation and the clusters of higher NDVI, it can be determined that more dense and taller vegetation is present on the east easement compared to the north and south easements. At this east fence, the dense and taller vegetation covers and surrounds the entire length of the channel. However, this phenomenon does not hold true for the south and north fenced areas. From Figure 5.18, it can be observed that the vast majority of the area inside the south fence does not fluctuate in elevation. This result indicates that there is no tall and dense vegetation, while in the north fence, there is some fluctuation

in the elevation (in some areas, the difference of height is > 10 m), indicating the presence of tall and dense vegetation.

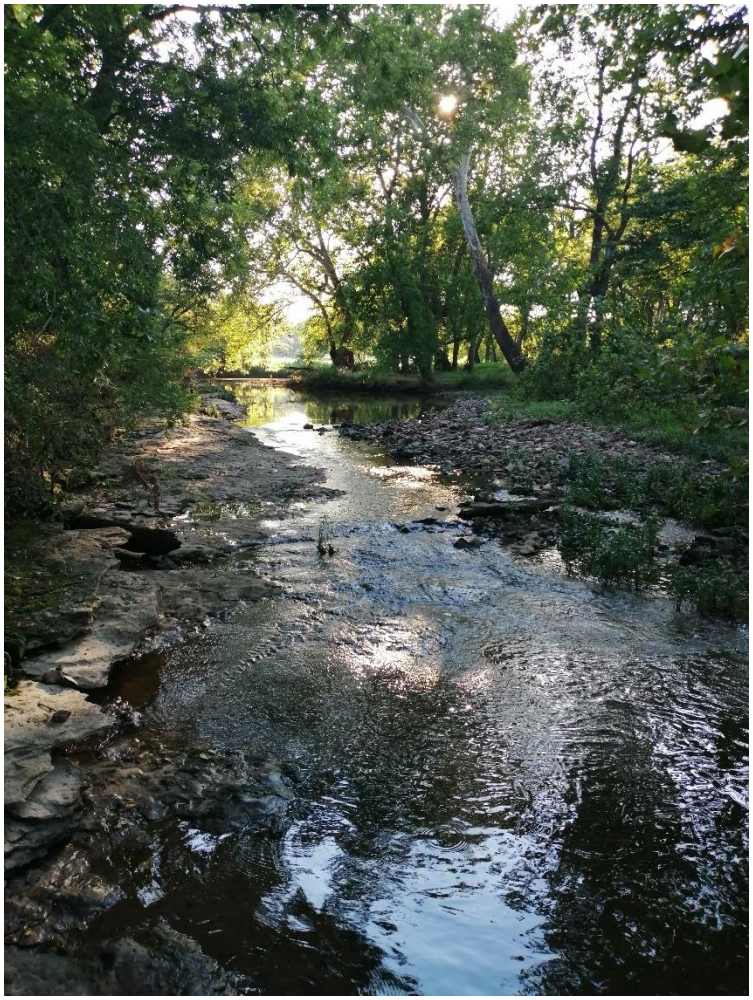

Figure 5.20. Upstream view inside the east easement. Picture taken during the 2019 summer.

By comparing the information present in Table 5.9 it seems that the current stage (in terms of LULC) of this riparian zone has not deviated from the 15-year average. However, it is important to mention that a drastic change on undisturbed LULC is not expected to happen in a two-year span.

5.4.Discussion

The approach taken was based on the use of historical water quality data (e.g., data collected by OCC from 1999 to 2018) and recent water quality (e.g., data collected by CREW from 2018 to 2020), paired with LULC and precipitation data for the past 20 years and multispectral data from a single sUAS flight. As a general result, it can be suggested that water quality in the past two decades for the Upper Horse Creek watershed has been influenced by the LULC practices that take part inside its watershed boundaries (Figure 5.15 and Figure 5.17).

Different researchers have shown that LULC classes impact surface and groundwater quality in a given watershed (Rosario-Ortizm 2013; Nielsen et al., 2012; Meneses et al., 2015; Li et al., 2106; Tasdighi et al., 2017; Zhang et al., 2018; Jordan et al., 2018). This result becomes particularly relevant when watersheds are influenced by developed/urbanized areas and agricultural land uses. As presented by Giri and Qiu (2016), land development/urbanization increases impervious surfaces (e.g., roads, parking lots, sidewalks, and rooftops), which directly increase runoff with the potential to come in contact with pollutants (e.g., oils, greases or metals) and eventually discharge into bodies of water. Agricultural practices alter the soil profile and promote the use of fertilizers and pesticides that eventually discharge into bodies of water via runoff.

It is imperative to begin this discussion with an understanding of this information because the study presented herein not only supports the fact that LULC affects watershed water quality but also helps to recognize the drivers that have been influencing the Upper Horse Creek watershed. In terms of water quality in HC and LHC, there is no evidence of a drastic change in water quality in the past two decades. Both datasets (OCC and CREW) show that, despite their relative distance between the sampling locations (Figure 5.4) that theoretically

has the potential to introduce undocumented influences, there were no statistical differences for the different analytes collected by OCC and CREW.

It is important to evaluate some of the factors that directly drive water quality in HC and LHC, e.g., seasonality and LULC. Tufford et al., (1998) described that seasonal variations are directly correlated with changes in water quality. For their case, greater concentrations of TP were reported in the spring and summer months, while peak concentrations of TN were reported during winter and spring. According to them, these greater concentrations, and the negative impact that they have on water quality, can be attributed to season agricultural practices that take place inside the studied watershed. Research in the Upper Big Walnut Creek watershed located in central Ohio by Fort et al., (2018) concluded that seasonal variations directly affect stream water quality. For their case, these greater concentrations of TP, TN and NO_3^- were noted in summer, winter and spring, respectively. Likewise, Sigleo and Frick (2003) concluded that the driving mechanism that increases nutrient concentrations and loads in rivers is rainfall (higher rainfall leads to greater runoff, concentrations and mass loads, lower rainfall results in lesser runoff, concentrations, and mass loads). Overall, the findings presented in this study concur with these studies. As an overall trend, greater nutrient concentrations and mass loading rates were determined during the spring and winter months for PO_4^{3-}, NO_2^-, NO_3^-, and SO_4^{2-}. At the same time, the seasonal precipitation analysis (Table 5.5) showed that average monthly precipitation was higher during the spring months, suggesting that that runoff from precipitation could be the mechanism that increases/decreases the concentrations and mass loads in HC and LHC.

In terms of the mass loads, and to have a general idea of where the Upper Horse Creek watershed stands (with reference to similar watersheds), a direct comparison between a similar LULC watershed was performed. For this comparison purposes the studies performed

by Schilling and Wolter (2004), Schilling and Zhang (2004) and Schilling et al., (2018) were used. Schilling and Wolter (2004) reported that for Walnut Creek watershed in Iowa (LULC dominated by crops and grasslands) annual SO_4^{2-} mass loads range from 0.19 – 37.6 kg/ha (five-year period). Schilling and Zhang (2004) reported that for Raccoon River watershed in Iowa (LULC dominated by crops and grasslands) annual NO_3^- mass loads range from 1.4 – 65.9 kg/ha (23-year period). Schilling et al., (2018) reported that for Walnut Creek watershed in Iowa (LULC dominated by crops and grasslands) annual PO_4^{3-} mass load range from 0.01 – 1.08 kg/ha (three-year period). Taking these as a refence point, it can be observed that the Horse Creek watershed falls within the range for a watershed dominated by crops and grasslands.

As mentioned before, LULC has a marked influence on water quality. For the case of the Upper Horse Creek watershed, LULC was relatively stable between 2001 and 2016 (Table 5.8). The only major change ($\geq 5\%$) inside the watershed was the loss of 5.56% of pasture/hay and the gain of 5.36% of cultivated crops. At this point, it is important to mention that one of the greatest limitations of this study in terms of LULC data was the temporal resolution of the NCLD data. Due to the complexity and labor-intensive process of developing this dataset (USGS, 2020), changes in LULC data can only be calculated up to 2016, given that 2016 NCLD is the latest and most up-to-date product. However, and to evaluate if this apparent LULC "stability" that the Upper Horse Creek watershed appears to demonstrate for 15 years (2001-2016) is valid, an additional LULC cover analysis was performed using the MODIS/Terra+Aqua Land Cover Type Product (MCD12Q1). The MCD12Q1 product provides global maps of land cover at a spatial resolution of 500 m and annual temporal resolution (starting from 2001 to present) (NASA, 2020). Due to the coarser spatial resolution of MCD12Q1 and different LULC classification algorithms within the Upper Horse Creek watershed, there are only three LULC classes (1) croplands, (2) grasslands, and (3) savannas.

Throughout the past 18 years (2001 – 2019), these data show that LULC remained relatively stable. There was a gain of 4.92% and 0.17% in grasslands and savannas, respectively; and a loss of 4.92% of croplands (MCD12Q1 uses a different classification and algorithm than the NLCD). It may be concluded that, despite the LULC classification given by each product, LULC inside the watershed has been stable.

Despite the results shown by both LULC datasets, it is very noticeable that from 2001 to 2016, LULC inside the Upper Horse Creek watershed has been dominated by (1) pasture/hay and (2) cultivated crops with a 15-year average distribution of 64% and 26%, respectively. Bidwell and Woods (2017) indicate that in the state of Oklahoma, a great percentage of the pastures are used to sustain cattle production. These pastures (introduced forage) require active management practices. Among others and as described by these authors, one of the practices to ensure optimum forage production is the use of industrial or natural (e.g., animal waste product) fertilizers capable of supplying nitrogen sources (e.g., NH_4^+, NO_3^-, ammonium sulfate ($(NH_4)_2SO_4$) and urea (CH_4N_2O)). Coulter et al., (2004) performed a study in the East Hickman Creek watershed of Fayette County, Kentucky (a watershed dominated by agricultural, urban and mixed LULC). The purpose of their study was to examine and determine the NPS pollution associated with agricultural and urban LULC. As part of their findings, they stated that agricultural watersheds had significantly greater average concentrations of NO_3^-, PO_4^{3-}, and TP compared to urban watersheds. They attributed these greater concentrations to "higher areal rates of fertilization during cropping". That said and considering the results presented in Section 3 of this study, it is most likely that in the Upper Horse Creek watershed, the most probable cause of negative impacts in water quality is NPS pollution from the management practices that take place in pasture/hay and cropland areas.

The underlining driving force that historically has influenced water quality in this watershed is LULC. To better illustrate and understand the historical influence that LULC has had on water quality in the Upper Horse Creek watershed, an RDA was used (section 5.3.3). RDA has been widely used to determine the influences of multiple LULC and water quality parameters simultaneously (Silva and Williams, 2001; Shen et al., 2015; Shi et al., 2017). The RDA analysis presented in this study used the seasonal water quality and the four dominant LULC classes (e.g., (1) pasture/hay, (2) cultivated crops, (3) urban development and (4) deciduous forest). This RDA concluded the two LULC (pasture/hay, (2) cultivated crops) that statistically explain the variance in the seasonal water quality are pasture/hay and cultivated crops (cumulative eigenvalues for all cases were higher than 85% for all cases). This relationship between water quality and LULC becomes more evident when examining the biplots (Figure 5.18 and Figure 5.19). From these biplots it can be observed that the relationship of water quality analytes with pasture/hay, cultivated crops and urban development (this last one only for the case of HC) is positive (angle between lines is < 90°), while the relationship that these analytes have with forest is negative. Song et al., (2020) not only found that pollution in a watershed is positively related to urbanized LULC area by means of an RDA, but also noted that "when the included angle (between the arrows of a land-use type and water quality indicator) is less than 90 degrees, the relationship between them is positive. In contrast, the relationship between them is negative when over 90 degrees, and there is no correlation when equal to 90 degrees". Liu et al., (2016) performed an RDA using various spatial scales in a watershed with different LULC. As part of their findings, they reported that concentrations of ammonia (NH_3) and TP had positive correlations with urban areas. In the same way, Zhang et al. (2019), after performing an RDA using different LULC, landscape metrics and in-situ water quality measurements, concluded that agricultural lands were positively correlated with concentration of TP, NH_4^+, total dissolved phosphorus

(TDP), and NO_3^-. Finally, Shi et al., (2016) not only found the same positive relationship when performing an RDA between water quality and LULC, but also concluded that a negative relationship between water quality and forest land use classes indicate the positive effect that this land use can have on improving water quality.

As mentioned above, in 2018 GRDA, OCC and an influential private landowner in the region implemented a series of riparian conservation easements on Horse Creek. The current stage of these pilot conservation easements shows that by constructing a fence around the riparian zone of small portions of HC, vegetation has the potential to grow undisturbed (Figure 5.17, 5.18, and 5.19). However, at this early time and due to limited available data that has been collected after the implementation of the easements, it cannot be concluded that they are or are not improving water quality in HC. Theoretically, and as concluded by several authors (Osborne and Kovacic (1993); Lowrance et al., (1997); Snyder et al., (1998); Spruill (2000); Anbumozhi et al., (2005); Li et al., (2009) and Wang et al., (2020)) riparian buffers not only have the ability to significantly reduce nutrient concentrations (e.g., TP, NH_4^+, NO_3^-, TDP, NH_3) by means of deposition, sorption, and denitrification before they enter a stream channel (serving as nutrient sinks), but also improve water quality by capturing runoff from NPS pollution. With the above in mind and given the proper amount of time, these conservation easements will work as natural environmental buffers and eventually help to decrease concentrations of nutrients going into HC.

5.5. Conclusions

From the results of this study, it can be concluded that: (1) measured water quality parameters in LHC have been relatively stable for the past two decades, (2) measured water quality parameters for HC have been relatively stable for the two periods of data collection (e.g., 1999 -2001 and 2011 – 2020), (3) LULC inside the Upper Horse Creek watershed has seen

minimal changes, (4) the watershed is dominated by pasture/hay (62%) and cultivated crops (28%), (5) it can be suggested that historical water quality for the watershed has been influenced by pasture/hay and cultivated crops (RDA), (6) one of the sources of elevated concentrations of nutrients could be attributed to NPS pollution that comes from actively managing pasture/hay and agricultural land and (7) at this point is not possible to determine the effect that the riparian conservation easements are having on water quality.

References

Abe, J.D; Driscoll, C.T. Effects of land use, climate variation, and N deposition on N cycling and C storage in northern hardwood forests. Nitrogen Cycling in Forested Catchments. 2012, 11(4), pp. 639-648.

Aerial Technology International. 2019. ATI AgBOT Data Sheet. [Online]. [Accessed November 1, 2020]. Available from: http://store.aerialtechnology.com/product/agbot-2/

Ahiablame, L.M.; Engel, B.A.; Chaubey, I. Effectiveness of Low Impact Development Practices: Literature Review and Suggestions for Future Research. Water Air Soil Pollution, 2012, 223, pp. 4253–4273.

Alvarez, X.; Valero, E.; Santos, R.M.B; Varandas, S.G.P.; Sanches, L.F.; Pacheco, F.A.L.; Anthropogenic nutrients and eutrophication in multiple land use watersheds: Best management practices and policies for the protection of water resources. Land Use Policy, 2017, 69, pp. 1-11.

Anbumozhi, V.; Radhakrishnan, J.; Yamaji, E. Impact of riparian buffer zones on water quality and associated management considerations. Ecological Engineering, 2005, 24(5), pp. 517-523.

Anbumozhi, V.; Radhakrishnan, J.; Yamaji, E. Impact of riparian buffer zones on water quality and associated management considerations. Ecological Engineering, 2005, 24(5), pp. 517-523.

Aust, W.M.; Blinn, C.R. Forestry best management practices for timber harvesting and site preparation in the eastern United States: An overview of water quality and productivity

research during the past 20 years (1982–2002). Water, Air, & Soil Pollution: Focus, 2004, 4, pp. 5–36.

Baker, M.E.; Wiley, M.J.; Selbach, P.W. GIS-Based hydrologic modeling of riparian areas: Implications for stream water quality. Journal of the American Water Resources Association, 2001, 37(6), pp. 1615-1628.

Basnyat, P.; Teeter, L.D.; Lockaby, B.G.; Flynn, K.M. The use of remote sensing and GIS in watershed level analyses of non-point source pollution problems. Forest Ecology and Management, 2000, 128(1–2), pp. 65-73.

Bidwell, T.G.; Woods, B. 2017. Management Strategies for Rangeland and Introduced Pastures. [Online]. [Accessed November 1, 2020]. Available from: https://extension.okstate.edu/fact-sheets/management-strategies-for-rangeland-and-introduced-pastures.html

Boysen, L.R; Brovkin, V.; Arora, V.K.; Cadule, P.; de Noblet-Ducoudre, N.; Kato, E.; Pongratz, J. Global and regional effects of land-use change on climate in 21st century simulations with interactive carbon cycle. Earth System Dynamics, 2014, 5(2), pp. 309-319.

Brion, G.; Brye, K. R.; Haggard, B.E.; West, C.; Brahana, J.V. Land-use effects on water quality of a first-order stream in the Ozark highlands, Mid-southern United States. River Research and Applications, 2011, 27, pp. 772–790.

Bu, H.; Meng, W.; Zhang, Y.; Wan, J. Relationships between land use patterns and water quality in the Taizi River basin, China. Ecological Indicators, 2014, 41, pp. 187-197.

Carle, M.V.; Halpin, P.N.; Stow, C.A. Patterns of watershed urbanization and impacts on water quality. Journal of the American Water Resources Association, 2005, 41(3), pp. 693–708.

Chen, B.; Wang, M.; Duan, M.; Ma, X.; Hong, J.; Xie, F.; Zhang, R.; Li, Z. In search of key: Protecting human health and the ecosystem from water pollution in China. Journal of Cleaner Production, 2019, 228, pp. 101-111.

Chen, S.; Wu, D. Adapting ecological risk valuation for natural resource damage assessment in water pollution. Environmental Research, 2018, 164, pp. 85-92.

Chen, X. W. Using remote sensing and GIS to analyze land cover change and its impacts on regional sustainable development. International Journal of Remote Sensing, 2002, 23, pp. 107–124.

Copernicus Global Land Service (CGL). 2020. Normalized Difference Vegetation Index. [Online]. [Accessed November 1, 2020]. Available from: https://land.copernicus.eu/global/products/ndvi

Corbett, C.W.; Wahl, M.; Porter, D.E.; Edwards, D.; Moise, C. Nonpoint source runoff modeling A comparison of a forested watershed and an urban watershed on the South Carolina coast. Journal of Experimental Marine Biology and Ecology. 1997, 213(1), pp. 133-149.

Corriveau, J; Chambers, P.A.; Culp, J.M. Seasonal Variation in Nutrient Export Along Streams in the Northern Great Plains. Water Air Soil Pollution, 2013, 224, pp. 1594.

Cristan, R.; Aust, M.W.; Bolding, M.C.; Barrett, S.M.; Munsell, J.F. National status of state developed and implemented forestry best management practices for protecting water quality in the United States. Forest Ecology and Management, 2018, 418, pp. 73-84.

Dai, X.; Zhou, Y.; Ma, W.; Zhou, L. Influence of spatial variation in land-use patterns and topography on water quality of the rivers inflowing to Fuxian Lake, a large deep lake in the plateau of southwestern China. Ecological Engineering, 2017, 99.

Dowd, B.M.; Press, D.; Los Huertos M. Agricultural nonpoint source water pollution policy: The case of California's Central Coast. Agriculture, Ecosystems & Environment, 2008, 128(3), pp. 151-161.

Foley, JA.; Defries, R.; Asner, G.P.; Barford, C.; Bonan, G.; Carpenter, S.R.; Chapin, F.S.; Coe, M.T.; Daily, G.C.; Gibbs, H.K.; Helkowski, J.H.; Holloway, T.; Howard, E.A.; Kucharik, C.J.; Monfreda, C.; Patz, J.A.; Prentice, I.C.; Ramankutty, N.; Snyder, P.K. Global Consequences of Land Use. Science, 2005, 309(5734), pp. 570-574.

Food and Agriculture Organization of the United Nations (FAO). Land-cover change describes differences in the area occupied by cover types through time. Available online: http://biology.usgs.gov/s+t/SNT/noframe/lu106.htm water (accessed on 10 September 2020).

Fraga, I.; Charters, F.J.; O'Sullivan, A.D.; Cochrane, T.A. A novel modelling framework to prioritize estimation of non-point source pollution parameters for quantifying pollutant origin and discharge in urban catchments. Journal of Environmental Management, 2016, 167, pp. 75-84.

Ford, W.I.; King, K.; Williams, M.R. Upland and in-stream controls on baseflow nutrient dynamics in tile-drained agroecosystem watersheds. Journal of Hydrology, 2018, 556, pp. 800-812.

Galbraith, L.M.; Burns, C.W. Linking Land-use, Water Body Type and Water Quality in Southern New Zealand. Landscape Ecology, 2007, 22, pp. 231–241.

Geomorphology, 2006, 79(3-4), pp. 264-285.

Giacomazzo, M.; Bertolo, A.; Brodeur, P.; Massicotte, P.; Goyette, J.; Magnan, P. Linking fisheries to land use: How anthropogenic inputs from the watershed shape fish habitat quality.

Giri, S.; Qiu, Z. Understanding the relationship of land uses and water quality in Twenty First Century: A review. Journal of Environmental Management, 2016, 173, pp. 41-48.

Glandon, R.P.; Payne, F.C.; McNabb, C.D.; Batterson, T.R. A comparison of rain-related phosphorus and nitrogen loading from urban, wetland, and agricultural sources. Water Research, 1981, 15(7), pp. 881-887.

Goonetilleke, A.; Thomas, E.; Ginn, S.; Gilbert, D. Understanding the role of land use in urban storm water quality management. Journal of Environmental Management, 2005, 74(1), pp. 31–42.

Gordon, L.J.; Steffen, W.; Jonsson, B.F.; Folke, C.; Falkenmark, M.; Johannessen, A. Human modification of global water vapor flows from the land surface. National Academy of Sciences, 2005, 102(21), pp. 7612-7617.

Grand River Dam Authority. 2017. GRDA expanding blue green algae advisory. [Online]. [Accessed November 1, 2020]. Available from http://www.grda.com/grda-expanding-blue-green-algae-advisory/

Grand River Dam Authority. 2017b. Water Quality Grand Lake. [Online]. [Accessed November 1, 2020]. Available from http://www.grda.com/grda-installs-new-water-quality-monitoring-equipment-on-grand-hudson/

Haidary, A.; Amiri, B.J.; Adamowski, J.; Fohrer, N.; Nakane, K. Assessing the Impacts of Four Land Use Types on the Water Quality of Wetlands in Japan. Water Resources Management, 2013, 27, pp. 2217–2229.

Hale, R.L.; Grimm, N.B.; Vorosmart, C.J.; Fekete, B. Nitrogen and phosphorus fluxes from watersheds of the northeast U.S. from 1930 to 2000: Role of anthropogenic nutrient inputs, infrastructure, and runoff. Global Biogeochemical Cycles, 2015, 29(3), pp. 341-356.

Huang, J.; Zhan, J.; Yan, H.; Wu, F.; Deng, X. Evaluation of the Impacts of Land Use on Water Quality: A Case Study in The Chaohu Lake Basin. The Scientific World Journal, 2013, 2013(7).

Hunt, W.F; Jarrett, A.R.; Smith, J.T; Sharkey, L.J. Evaluating Bioretention Hydrology and Nutrient Removal at Three Field Sites in North Carolina. Journal of Irrigation and Drainage Engineering, 2016, 132(6).

Ice, G. History of Innovative Best Management Practice development and its role in addressing water quality limited waterbodies. Journal of Environmental Engineering, 2004, 130(6).

Jordan, T.E.; Weller, D.E.; Pelc, C.E. Effects of Local Watershed Land Use on Water Quality in Mid-Atlantic Coastal Bays and Subestuaries of the Chesapeake Bay. Estuaries and Coasts, 2018, 41, pp. 38–53.

Krauskopf, K.B.; Loague, K. Environmental Geochemistry. Encyclopedia of Physical Science and Technology (Third Edition), 2003.

Lenat, D.R.; Crawford, J.K. Effects of land use on water quality and aquatic biota of three North Carolina Piedmont streams. Hydrobiologia, 1994, 294, pp. 185–199.

Leon, L.F.; Soulis, E.D.; Kouwen, N.; Farquhar, G.F. Nonpoint source pollution: a distributed water quality modeling approach. Water Research, 2001, 35(4), pp. 997-1007.

Li, L.; He, Z.; Li, Z; Zhang, S.; Li, S.; Wan, Y.; Stoffella, P.J. Spatial and temporal variation of nitrogen concentration and speciation in runoff and storm water in the Indian River watershed, South Florida. Environ Science Pollution, 2016, 23, pp. 19561–19569.

Li, S.; Gu, S.; Tan, X.; Zhang, Q. Water quality in the upper Han River basin, China: The impacts of land use/land cover in riparian buffer zone. Journal of Hazardous Materials, 2009, 165(1-3), pp. 317-324.

Liu, R.; Xu, F.; Zhang, P.; Yu, W.; Men, C. Identifying non-point source critical source areas based on multi-factors at a basin scale with SWAT. Journal of Hydrology, 2016, 533, pp. 379-388.

Liu, Y.; Engel, B.A.; Flanagan, D.C.; Gitau, M.W.; McMillan, S.K.; Chaubey, I. A review on effectiveness of best management practices in improving hydrology and water quality: Needs and opportunities. Science of The Total Environment, 2017, 601–602, pp. 580-593.

Lowrance, R., Altier, L., Newbold, J.; Schnabel, Ronald R. Groffman, P.M.; Denver, J.M.; Correll, D.L.; Gilliam, J.W.; Robinson, J.L.; Brinsfield, R.B.; Staver, K.W.; Lucas, W., Todd, A.H. Water Quality Functions of Riparian Forest Buffers in Chesapeake Bay Watersheds. Environmental Management, 1997, 21, pp. 687–712.

Matejicek, L.; Benesova, L.; Tonika, J. Ecological modelling of nitrate pollution in small river basins by spreadsheets and GIS. Ecological Modelling, 2003, 170(2-3), pp. 245-263.

Meneses, B.M.; Reis, R.; Vale, M.J.; Saraiva, R. Land use and land cover changes in Zezere watershed (Portugal) — Water quality implications. Science of The Total Environment, 2015, 527–528, pp. 439-447.

Minnesota Department of Agriculture (MDA). 2017. Agricultural BMP Handbook for Minnesota. [Online]. [Accessed November 1, 2020]. Available from: https://wrl.mnpals.net/islandora/object/WRLrepository:2955

Mission Planner; Computer Software. ArduPilot Development Team. Available online: https://ardupilot.org/ planner/ (accessed on 1 May 2020).

Multi-Resolution Land Characteristics (MRLC) Consortium. 2020. National Land Cover Database. [Online]. [Accessed November 1, 2020]. Available from: https://www.mrlc.gov/

Munafo, M.; Cecchi, G.; Baiocco, F.; Mancini, L. River pollution from non-point sources: a new simplified method of assessment. Journal of Environmental Management, 2005, 77(22), pp. 93-98.

National Ocean Service (NOA). What is the difference between land cover and land use? Available online: https://oceanservice.noaa.gov/facts/lclu.html (accessed on 10 September 2020).

Nielsen, A.; Trolle, D.; Sondergaard M.; Lauridsen, T.L.; Bjerring, R.; Olesen, J.E.; Jeppesen, E. Watershed land use effects on lake water quality in Denmark. Ecological Applications, 2012, 22(4), pp. 1187–1200.

Nobre, C.A.; Sampaio, G.; Borma, L.S.; Castilla-Rubio, J, C.; Silva, J.S; Cardoso, M. Land-use and climate change risks in the Amazon and the need of a novel sustainable development paradigm. Proceedings of the National Academy of Sciences, 2016, 113(39), pp. 10759-10768.

Oklahoma Conservation Commission (OCC). 1998. Riparian Area Management Handbook. [Online]. [Accessed December 10, 2020]. Available from http://pods.dasnr.okstate.edu/docushare/dsweb/Get/Document-2251/e-952.pdf

Oklahoma Department of Environmental Quality. 2020. Integrated Report – 303(D) & 305(B). [Online]. [Accessed April 24, 2020]. Available from https://www.deq.ok.gov/water-quality-division/watershed-planning/integrated-report/

Osborne, L.; Kovacic, D.A. Riparian vegetated buffer strips in water-quality restoration and stream management. Freshwater Biology, 1993, 29(2), pp. 243-258.

Pix4Dmapper; Computer Software; Pix4D SA: Prilly, Switzerland, 2011.

Poff, N.L.; Bledsoe, B.P.; Cuhaciyan, C.O. Hydrologic variation with land use across the contiguous United States: Geomorphic and ecological consequences for stream ecosystems.

Pokhrel, Y.N.; Felfelani, F.; Shin, S. Yamada, T., Satoh, Y. Modeling large-scale human alteration of land surface hydrology and climate. Geoscience Letters, 2017, 4(10).

R Core Team. R; Computer Software; R Core Team: Vienna, Austria, 2017.

Ren, W.; Zhong, Y.; Meligrana, J.; Anderson, B.; Watt, E.G., Chen, J.; Leung, H. Urbanization, land use, and water quality in Shanghai: 1947–1996. Environment International, 2003, 29(5), pp. 649-659.

Roesner; L.A.; Bledsoe, B.P.; Brashear, R.W. Are Best-Management-Practice Criteria Really Environmentally Friendly? Journal of Water Resources Planning and Management, 2001, 127(3), pp. 150-154.

Rosario-Ortiz, F. Watershed Perturbations and Water Quality. Journal American Water Works Association, 2013, 105(4), pp. 2.

Rugel, E.J.; Henderson, S.B.; Carpiano, R.M., Brauer, M. Beyond the Normalized Difference Vegetation Index (NDVI): Developing a Natural Space Index for population-level health research. Environmental Research, 2017, 159, pp. 474-483.

Ruiz-Luna, A; Berlanga-Robles, C. A. Land use, land cover changes and coastal lagoon surface reduction associated with urban growth in northwest Mexico. Landscape Ecology, 2003, 18, pp. 159–171.

Salazar, A.; Baldi, G.; Hirota, M.; Syktus, J.; McAlpine, C. Land use and land cover change impacts on the regional climate of non-Amazonian South America: A review. Global and Planetary Change, 2015, 128, pp. 103-119.

Science of The Total Environment, 2020, 717.

Sharpley, A.N.; Daniel, T.; Gibson, G.; Bundy, L.; Cabrera, M.; Sims, T.; Stevens, R.; Lemunyon, J.; Kleinman, P.J.; Parry, R. Best management practices to minimize agricultural phosphorus impacts on water quality. Agricultural Research Service Publication, 2006, pp. 52.

Shen, Z.; Chen, L.; Liao, Q.; Liu, R.; Hong, Q. Impact of spatial rainfall variability on hydrology and nonpoint source pollution modeling. Journal of Hydrology, 2012, 472–473, pp. 205-215.

Sigleo, A.; Frick, W. Seasonal Variations in River Flow and Nutrient Concentrations in a Northwestern USA Watershed. U.S. Department of Agriculture, Agricultural Research Service, 2013.

Silva, L.; Williams, D.D. Buffer zone versus whole catchment approaches to studying land use impact on river water quality. Water Resources, 2001, 35(14), pp. 3462-72.

Schilling, K.; Wolter, E.; Calvin, F. Contribution of base flow to nonpoint source pollution loads in an agricultural watershed. Ground Water, 2004, 39(1), pp. 49-58.

Schilling. K.; Zhang, Y. Baseflow contribution to nitrate-nitrogen export from a large, agricultural watershed, USA. Journal of Hydrology, 2004, 295, pp. 305-316.

Schilling, K.E.; Streeter, M.T.; Isenhart, T.M.; Beck, W.J.; Tomer, M.D.; Cole, K.J.; Kovar J.L. Distribution and mass of groundwater orthophosphorus in an agricultural watershed. Science of the Total Environment. 2018, 625, pp. 1330-1340.

Snyder, N.J.; Mostaghimi, S.; Berry D.F.; Reneau, R.B., Hong. S.; McClellan, P.W.; Smith, E.P. Impact of riparian forest buffers on agricultural nonpoint source pollution. Journal of the American Water Resources Association, 1998, 34(2), pp. 385-395.

Song, Y.; Song, X.; Shao, G. Response of Water Quality to Landscape Patterns in an Urbanized Watershed in Hangzhou, China. Sustainability 2020, 12, 5500.

Spruill, T.B. Statistical evaluation of effects of riparian buffers on nitrate and ground water quality. Journal of Environmental Quality, 2000, 29(5), pp. 1523-1538.

Stohlgren, T.J.; Chase, T.N.; Pielke, R.A.; Kittel, T.G.; Baron, J.S. Evidence that local land use practices influence regional climate, vegetation, and stream flow patterns in adjacent natural areas. Global Change Biology, 1998, 4(5), pp. 495-504.

Stone, B. Urban Heat and Air Pollution: An Emerging Role for Planners in the Climate Change Debate. Journal of the American Planning Association. 2005, 7(1), 13-25.

Subbarayan, S.; Jegankumar, A.; Selvaraj, J.; Jacinth, J.; Parthasarathy, K.S. Utility of Landsat Data for Assessing Mangrove Degradation in Muthupet Lagoon, South India. Coastal Zone Management, 2019, pp. 471-484.

Tasdighi, A.; Arabi, M.; Osmond, D.L. The Relationship between Land Use and Vulnerability to Nitrogen and Phosphorus Pollution in an Urban Watershed. Journal of Environmental Quality, 2017, 46(1), pp. 113-122.

ter Braak, C. Canonical community ordination. Part I: Basic theory and linear methods. Ecoscience. Ecoscience, 1994, 1(2), pp. 127-140.

Tufford, D.L.; McKellar, H.N.; Hussey, J.R. In-stream nonpoint source nutrient prediction with land-use proximity and seasonality. Journal of Environmental Quality, 1998, 27(1), pp. 100-110.

The National Aeronautics and Space Administration (NAS). 2020. MCD12Q1 MODIS/Terra+Aqua Land Cover Type Yearly L3 Global 500 m SIN Grid. [Online]. [Accessed November 1, 2020]. Available from: https://lpdaac.usgs.gov/products/mcd12q1v006/

The United States Environmental Protection Agency (EPA). National Source Program – a catalyst for water quality improvements. Available online: https://www.epa.gov/sites/production/files/2016-10/documents/nps_program_highlights_report-508.pdf (accessed on 22 September 2020).

The United States Environmental Protection Agency (EPA). Science Inventory – Non-Point Source Pollution. Available online: https://cfpub.epa.gov/si/si_public_record_Report.cfm?Lab=NHEERL&dirEntryID=60116 (accessed on 22 September 2020).

Tran, C.P; Bode, R.W.; Smith, A.J.; Kleppel, G.S. Land-use proximity as a basis for assessing stream water quality in New York State (USA). Ecological Indicators, 2010, 10(3), pp. 727-733.

United States Geological Service (USGS). 2020. National Land Cover Database. [Online]. [Accessed November 1, 2020]. Available from: https://www.usgs.gov/centers/eros/science/national-land-cover-database?qt-science_center_objects=0#qt-science_center_objects

Vitousek, P.M. Beyond Global Warming: Ecology and Global Change. Ecology, 1994, 75(7), pp. 1861-1876.

Wang, M.; Duan, L.; Wang, J.; Peng, J.; Zheng, B. Determining the width of lake riparian buffer zones for improving water quality base on adjustment of land use structure. Ecological Engineering, 2020, 158.

Wang, X. Integrating water-quality management and land-use planning in a watershed context. Journal of Environmental Management, 2001, 61(1), pp. 25-36.

Wang, Y.; Bian, J.; Zhao, Y.; Tang, J.; Jia, Z.; Assessment of future climate change impacts on nonpoint source pollution in snowmelt period for a cold area using SWAT. Scientific Reports, 2010, 8, pp. 2402.

Wilson, C.O. Land use/land cover water quality nexus: quantifying anthropogenic influences on surface water quality. Environ Monitoring and Assessment, 2015, 187.

Wu, L.; Long, T.; Liu, X.; Guo, J. Impacts of climate and land-use changes on the migration of non-point source nitrogen and phosphorus during rainfall-runoff in the Jialing River Watershed, China. Journal of Hydrology, 2012, 475, pp. 26-41.

Yang, X.; Liu, Z. Using satellite imagery and GIS for land-use and land-cover change mapping in an estuarine watershed. International Journal of Remote Sensing, 2005, 26(23), pp. 5275-5296.

Yoon, S.W.; Chung, S. W.; Oh, D.G.; Lee, J.W. Monitoring of non-point source pollutants load from a mixed forest land use. Journal of Environmental Sciences, 2010, 22(6), pp. 801-805.

Zhang, X.; Zhou, L.; Liu, Y. Modeling Land Use Changes and their Impacts on Non-Point Source Pollution in a Southeast China Coastal Watershed. International Journal of Environmental Research and Public Health, 2018, 15, pp. 1593.

CHAPTER 6 – Conclusions

The main purpose of this dissertation was to use of multispectral imagery captured with the help of an sUAS to create/develop finer and more accurate models to predict both optical and non-optical water quality parameters capable to monitor small bodies of water, sizeable lakes with multiple beneficial uses, and watersheds with diverse land use and land cover.

After completing this study, it may be concluded that:

- With the use of imagery captured by an sUAS, and a thorough understanding of the existing relationships between water quality components in the systems involved, optical and non-optical water quality parameters can be reliably estimated.
- When using a multiple linear regression approach, models capable of predicting optical and non-optical models (with strong prediction capability $R^2 > 0.80$) can be created.
- Multiple variable linear regressions in the visible portion of the electromagnetic spectrum (blue, green, and red) best described the relationship between TSS ($R^2 = 0.99$, *p*-value ≤ 0.01), Chl-a ($R^2 = 0.85$, *p*-value ≤ 0.01), TP ($R^2 = 0.98$, *p*-value ≤ 0.01), TN ($R^2 = 0.98$, *p*-value ≤ 0.01), and SDD ($R^2 = 0.88$, *p*-value ≤ 0.01).
- Although sUAS imagery increased the regression coefficients, the major limitations experienced when operating an sUAS are caused by flight restrictions, safety (improper piloting/ high wind speeds/ unclear airspace designations), battery life ($\approx$20 minutes, which in turn decreases the size of the scene), and on-board sensor accuracy (large bandwidths, and limited GPS precision).
- Compared to satellite imagery, cloud free imagery can be collected with the use of sUAS.

- The use of sUAS for water quality monitoring allows the user more flexibility in terms of temporal and spatial resolution.
- Understanding the different limitations of traditional remote sensing (e.g., cloud coverage problems, necessary atmospheric corrections, adjacency, temporal and radiometric resolution), sUAS-collected data provide the opportunity to improve the reliability of surface water quality models.
- Currently sUAS pre-processing tools are not capable of properly stitching images captured over large bodies of water.
- Generation of completely geolocated and radiometrically corrected true reflectance surfaces for large bodies of waters allows for the estimation of optical water quality parameters using linear approaches.